A Low-Cost Directional Log Periodic Log Spiral Antenna

by

Emily McMilin
B.Sc., Stanford University, 2001

A Thesis Submitted in Partial Fulfillment of the
Requirements for the Degree of

MASTER OF APPLIED SCIENCE

in the Department of Electrical and Computer Engineering

A Low-Cost Directional Log Periodic Log Spiral Antenna

by

Emily McMilin
B.Sc., Stanford University, 2001

Supervisory Committee

Dr. J. Bornemann, Supervisor
(Department of Electrical and Computer Engineering)

Dr. S. Claude, Co-supervisor
(Department of Electrical and Computer Engineering)

Dr. T. Darcie, Departmental Member
(Department of Electrical and Computer Engineering)

Supervisory Committee

Dr. J. Bornemann, Supervisor
(Department of Electrical and Computer Engineering)

Dr. S. Claude, Co-supervisor
(Department of Electrical and Computer Engineering)

Dr. T. Darcie, Departmental Member
(Department of Electrical and Computer Engineering)

ABSTRACT

The Square Kilometer Array radio astronomy telescope will achieve the majority of its extremely large aperture area with thousands of parabolic dishes, each illuminated by a wideband antenna feed, and this thesis introduces a new such antenna. The wide bandwidth of this new antenna is achieved with the development of a directional log periodic antenna. Scaling the log periodic elements into three-dimensional space is the present method used for directional log periodic antennas. We propose confining these often complex log periodic elements into a single plane, while the ground "plane" takes on a three dimensional form, permitting low-cost implementations without requiring the introduction of a complicated scaffolding to support the log periodic elements in 3-D. This low-cost solution would scale well in the implementation of the thousands of antenna feeds that the Square Kilometer Array demands. We also introduce a previously unreported LP design: the log periodic log spiral antenna.

Contents

List of Tables

List of Figures

ACKNOWLEDGEMENTS

I would like to thank:

J. Bornemann, for his support, both broad and deep. From the lecture hall, to the small classroom, to the one on one meeting, I have learned and grown so much with his generous time and spirit. The rapidity and clarity with which he has provided me solutions has enabled my ideas to develop far beyond their initial conditions.

S. Claude, for welcoming me to the Herzberg Institute for Astrophysics, mentoring my development there, providing physical and technical support during the measurements and keeping me on a timeline!

D. Henke, for providing all of the ADS software simulation data and for his thoughtful contributions to the development of this thesis.

P. Czajko and N. Wren, for their ingenuity in transforming the models and equations into a working prototype.

J. Stilburn, for his support and assistance in the construction of the prototype.

Herzberg Institute for Astrophysics Victoria Staff for providing a year of funding, access to facilities and state of the art equipment, and a community of encouragement and support.

Dominion Radio Astrophysics Observatory Staff for welcoming me to their valuable facilities, sensitive equipment, and the roof over my head during the week of measurements.

Chapter 1

Introduction

1.1 The Square Kilometer Array

The Square Kilometer Array (SKA), graphically depicted in Figure 1.1, derives its name from the cumulative size of its total aperture area, predominantly composed of an array of thousands of radio dishes. The radio dishes will be carefully arranged over a region, likely centered in South Africa or Australia, with arms branching out to lengths of hundreds of kilometers. One of several arrangements proposed is that the dishes resemble a logarithmic spiral as depicted in Figure 1.2. Situated at the focal point of each dish in the array will be antenna elements designed to meet the scientific requirements for this ambitious project.

Several types of antenna are proposed to meet these goals, including [1]:

- Aperture Arrays (AAs): Planar arrays of antenna elements directly carpeting the ground, rather than placed above a dish, phased through fiber optic cables enabling multiple steered beams.

- Phased Array Feeds (PAFs): A smaller planar array of antenna elements located within the focal plane of a parabolic dish, enabling a larger "Field of View" (FoV) than possible with a single element above the dish.

- Single Pixel Feeds (SPFs): A single antenna element situated at the focal point of a

parabolic dish. For SKA purposes, these feeds are required to receive a very "Wide Band" of frequencies, earning the name: WB+SPF.

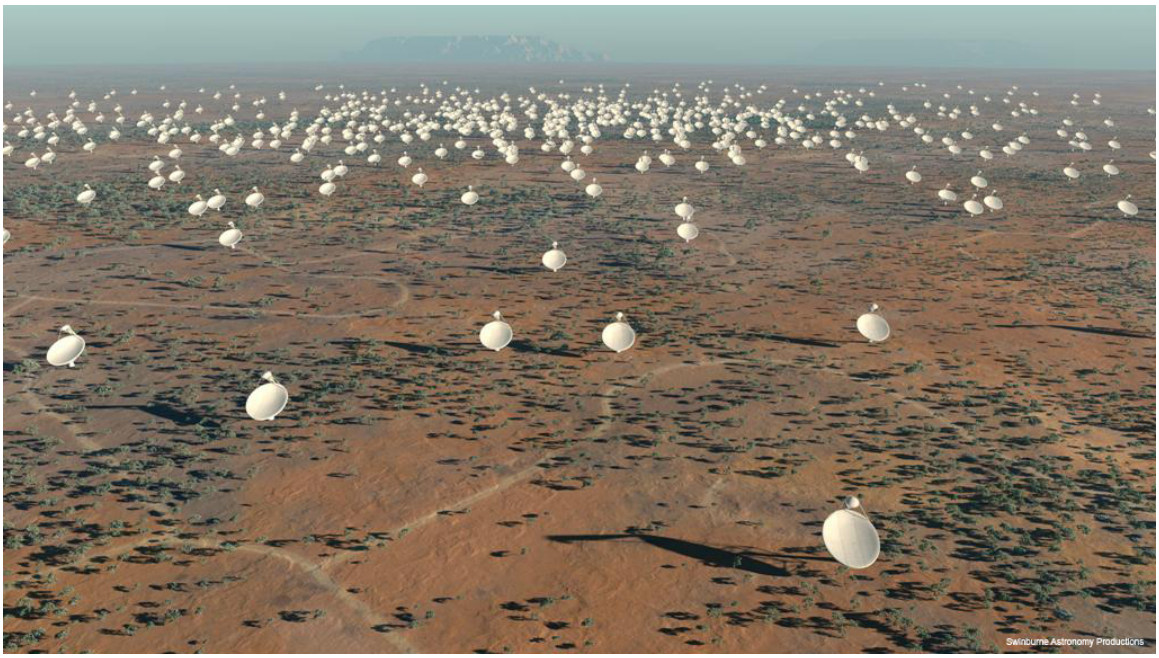

Figure 1.1: Artist's conception of SKA dishes [2].

Each of these technologies contributes benefits as well as barriers toward the projected 2020 implementation of the SKA. Although debate currently continues as to what engineering topologies can best achieve the SKA's science goals and budget constraints over the 500 MHz to 10 GHz frequency range, WB+SPFs have been chosen to cover the majority of this bandwidth [4].

> "It is likely that two different arrays of antennas will be needed to cover the frequency range up to 500 MHz. From 500 to 1000 MHz, there are three possibilities: dense AAs, parabolic antennas with PAFs, and parabolic antennas with SPFs. From 1000 MHz to 10 GHz, parabolic antennas with SPFs are chosen."

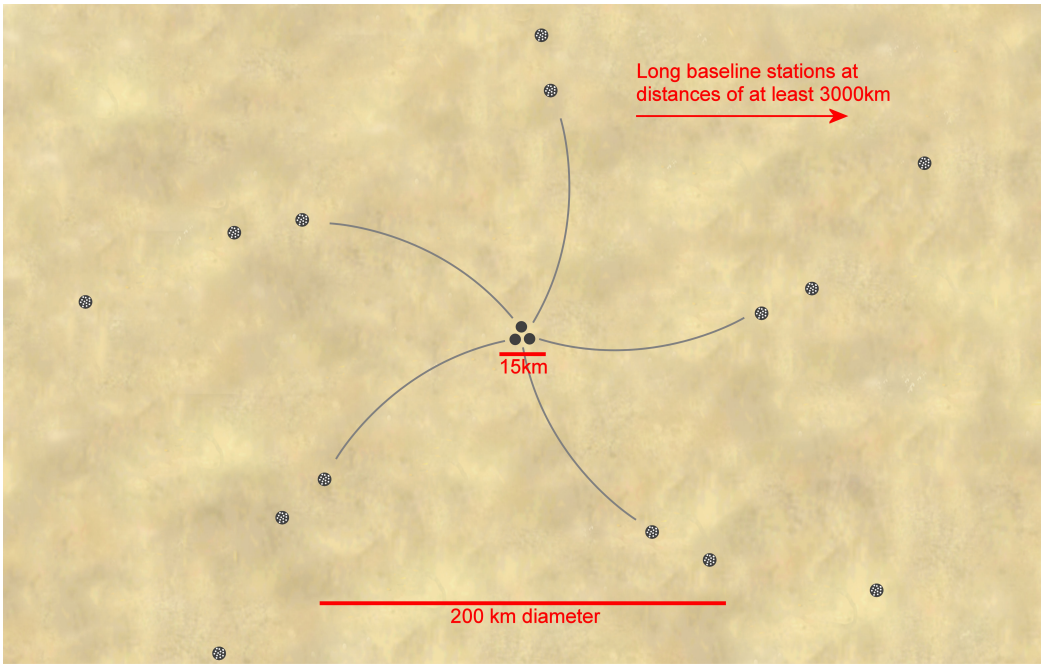

Figure 1.2: Artist's distant view of SKA dishes arranged in a logarithmic spiral [3].

1.2 Objective

This thesis introduces a new WB+SPF that will meet as many of the SKA specifications as possible while also providing a cost-effective solution for this next generation radio telescope. The wide bandwidth will be achieved by employing Frequency Independent (FI) design principles, reintroduced for present day radio astronomy purposes by W. J. Welsh and G. Engargiola [5]. FI antenna theory, succinctly described by Victor H. Rumsey in 1966 [6], relies primarily on the following design principles:

1. Maxwell's equations are frequency invariant in coordinate systems normalized to wavelengths. Therefore, two distinct structures can exhibit identical radiation properties at two different frequencies, only if the absolute dimensions of the structures have been scaled by the inverse ratio of the two frequencies. Such scalings can be embedded within a single structure that has self-similar properties. Self-similar (SS) antennas with a common feed point can be obtained via:

    - a continuous scaling of all features, such as that exhibited in a logarithmic spiral,

Figure 1.3: An example of a naturally occurring logarithmic spiral [7].

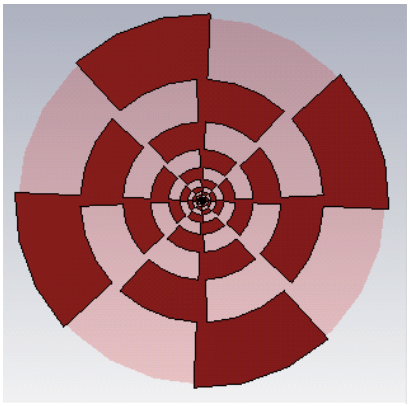

Figure 1.4: A SC pattern for an antenna with a common feedpoint in the center.

comparable to some naturally occurring weather patterns (Figure 1.3).

- a periodic scaling of a selected "cell" by a geometric ratio, for example the scaling of half-wavelength dipole elements that comprise the common VHF/UHF log periodic aerials placed atop roofs for the reception of television (c.f. Section 2.2.2.)

2. Aperture size must also scale with frequency. Furthermore, no standing wave patterns should be excited on the antenna. Therefore, there must be an "active region" (AR) where most of the energy at a given frequency radiates. If the location of this region also scales with frequency, to an upper dimension beyond the largest wavelength of

interest, the antenna can avoid the "end-effect", whereby none of the currents reach the antenna's edge to permit a reflection.

3. A constant impedance across the band can be achieved for a frequency range in which the antenna structure appears to be "Self-Complementary" (SC) to the currents excited at those frequencies. Figure 1.4 displays one such SC pattern. The clever application of Babinet's principle [8] for complementary structures to SC structures, known as Mushiake's relation [6], provides a theoretical feedpoint impedance common to all FI antennas; however, it is not a necessary condition for achieving a wideband antenna.

Unlike other efforts at broadbanding structures, such as adding ridges to waveguides and horns, or designing ultra wideband (UWB) antennas that radiate under a specified power spectral density for a large, though limited, bandwidth, there is no theoretical limit to the bandwidth an FI structure can achieve. Bandwidths exceeding 1,000:1 are achievable, but not practical given the technological limitations of backend elements. As such, bandwidths limited to 40:1 have been obtained [6].

1.3 Current Developments

A basic adherence to the FI principles above, most specifically items 1 and 2, has resulted in the development of several antennas currently proposed as WB+SPF solutions for the SKA, including the Allen Telescope Array (ATA) feed (Figure 1.5), the Quasi-Self-Complementary (QSC) feed (Figure 1.6), and the Eleven feed (Figure 1.7).

The antenna proposed in this thesis attempts to incorporate all the FI design principles stated above, by placing the radiating elements in a single plane, while shaping the ground "plane" into a three-dimensional ground "surface". Confining the complex radiating elements into one plane permits low-cost implementations of this structure, including printed circuit board (PCB) and water jet cutting technology, without requiring the introduction

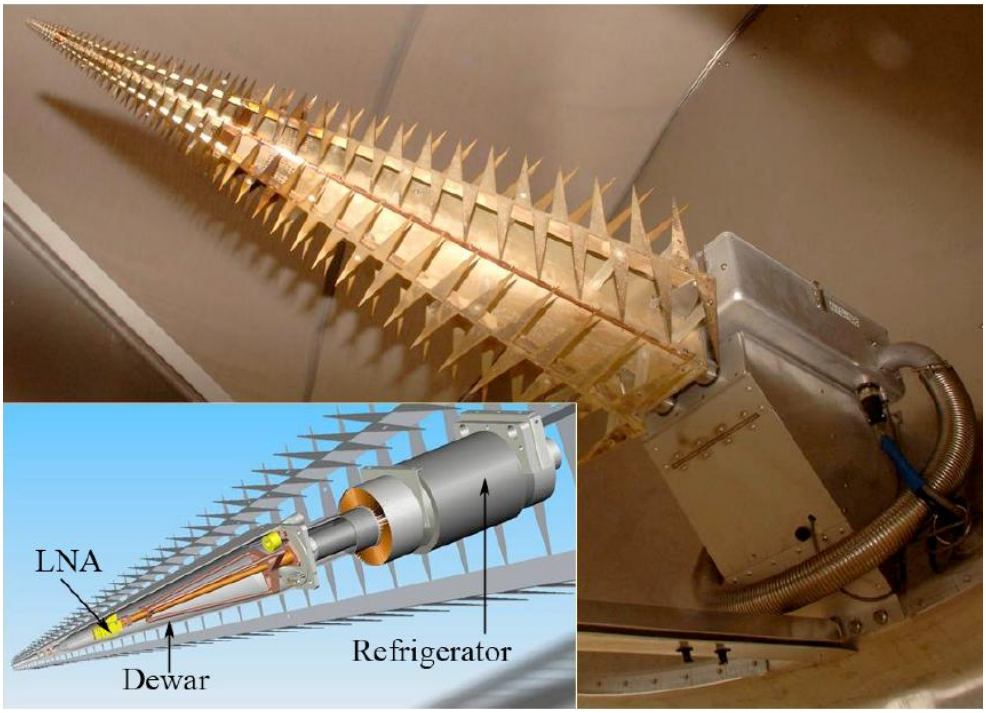

Figure 1.5: The ATA feed mounted in a dish with a closeup of the internal amplifier, dewar, and refrigerator for operation in the 500 MHz to 11 GHz frequency range [9].

of a complicated scaffolding to support the elements. A previously un-reported design of the radiating elements that combines the logarithmic spiral with the log periodic structure is described here. Measured results are shown to compare well with simulated results and also compare well with the early finding of other antennas currently proposed for the SKA.

1.4 Thesis Organization

This document is organized into 6 chapters, including this introduction, as outlined below:

Chapter 2 describes the implemented FI principles in detail and in application to the SKA.

Chapter 3 details the new contributions in the proposed design and their theoretical underpinnings, as well as the method of implementation.

Chapter 4 contains the computer simulated experiments undertaken to design and char-

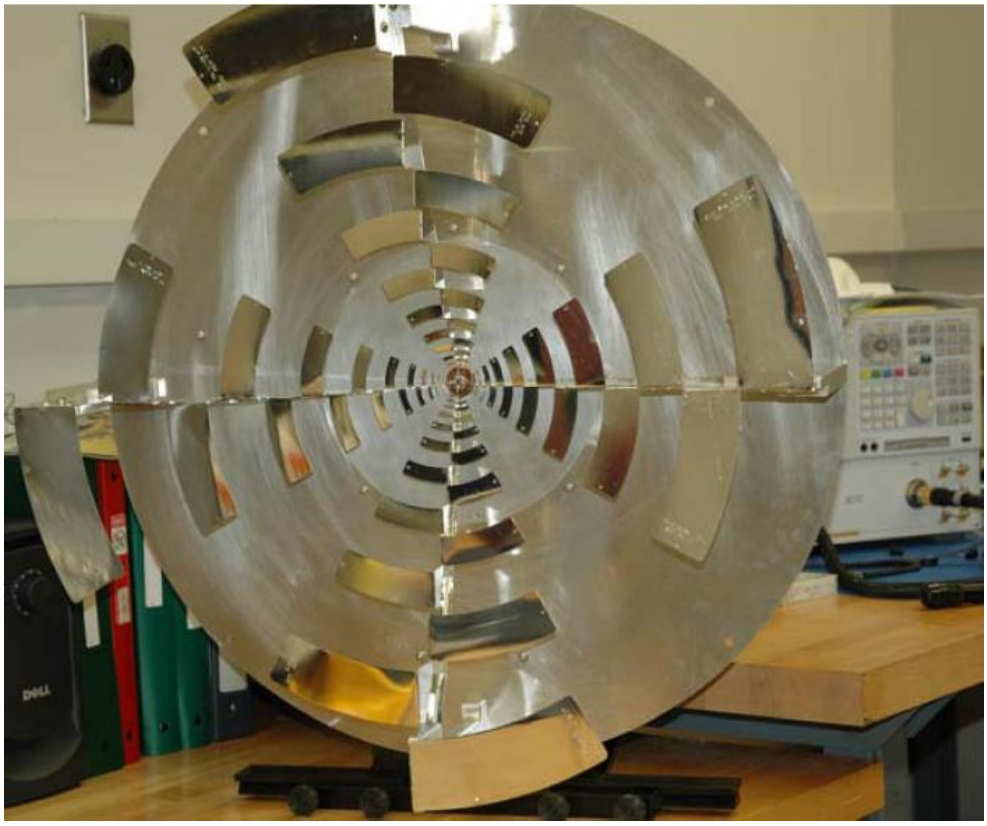

Figure 1.6: A prototype of the QSC feed fabricated to operate in the 500 MHz to 5 GHz frequency range [10].

acterize the antenna.

Chapter 5 describes the physical measurements undertaken to validate the theoretical and simulated results, and allow for brief comparisons to other contributions to this field.

Chapter 6 concludes with a restatement of the objective and results of the thesis as well as problems left unresolved for future work.

Figure 1.7: The Eleven feed built for 150 - 1500 MHz observations at the Green Bank radio telescope [11].

Chapter 2

Background

Figure 2.1: An optical image of a spiral galaxy [12].

2.1 Radio Astronomy

Although a single dish with a collecting area of one square kilometer is not feasible, a dozen very large dishes with dimensions similar to Arecibo's 73,000 square meter collecting area could achieve the SKA's required light-gathering power. For various reasons, this model of a small number of large diameter dishes has primarily been replaced by the "large number, small diameter" (LNSD) dish concept, currently being implemented to achieve $\frac{1}{10}$th of a

square kilometer collecting area in the Allan Telescope Array (ATA) [13]. Clearly, the LNSD model for the SKA requires thousands of antennas and receivers matched to the thousands of proposed dishes.

Figure 2.2: Wideband quadridge feed horn manufactured by ETS-Lindgren.

Horn antennas have traditionally been paired with radio astronomy dishes to provide efficient illumination of the dish [14]. Horn antennas are effectively waveguides that have been gradually broadened at one end, such that the opening dimensions may be several wavelengths in size. However, at the other end, the largest dimension of the waveguide attached to the horn is roughly a half wavelength at the lowest frequency and a whole wavelength at the highest frequency, for single mode operation. Ridges can be added to the center of waveguiding structures to permit bandwidths that exceed one octave. Wideband radio telescopes have been implemented with a modified quadridge feed horn (Figure 2.2) that can excite single mode bandwidths of 4:1 and beyond [15]. However, it is difficult to achieve a frequency invariant radiation pattern across the band, as the size of the horn's aperture does not effectively scale with frequency. Therefore, the highest frequencies will be radiated from a relatively large aperture to create a relatively narrow beamwidth. A compromise must then be made between over-illumination of the dish and thus spillover at the lowest frequencies, or under-illumination and thus inefficient utilization of the dish at the highest frequencies.

2.2 Self-Similarity

The FI design theory outlined in Chapter 1 can permit a consistent aperture size, independent of frequency, by appropriately scaling the dimension's of the "active region" with wavelength. If the majority of applied power at a given frequency is radiated within this active region the effective size of the aperture will also scale with frequency. In fact, many of an antenna's properties such as impedance, radiation patterns, and polarization can be designed to be independent of frequency across very large bandwidths.

Maxwell's equations can be shown to be scale invariant when measured in spatial units per wavelength [6]. That is, an original structure and its similar version, scaled by τ, in spatial dimensions, will be solved for the same solution at frequencies f_0 and $\frac{f_0}{\tau}$, respectively. This property is used in practice to measure the radiation characteristics of a smaller, scaled-down prototype that replaces the larger unwieldy antenna that will eventually be used in practice. Alternatively a scaled-up prototype may be tested in lieu of a smaller, higher frequency version of the antenna that requires difficult or minute machining processes.

2.2.1 Logarithmic Spirals

Instead of entirely replacing the scaled version for the original, FI antennas embed both the scaled versions and the "original" into one structure. This results in an antenna that is SS. Early SS antennas where constructed with a logarithmic spiral (LS) of a form similar to the distant spiral galaxies observed in our universe (Figure 2.1). In the case of the two-arm spiral, the second arm is obtained by rotating the first arm by 180 degrees. The two arms may then be fed against one another in a differential mode to complete the FI antenna. An LS is also known as an equiangular spiral due the following property: if a radial line r is drawn outward from the central pole of the spiral, the angle between r and the tangent of the spiral at each intersection will always maintain the same angle β as shown in Figure 2.3. Now we define each of the intersecting points between the radial line and the curve of the spiral with the variables: ρ_n, $\rho_{(n-1)}$, $\rho_{(n-2)}$..., with ρ_0 located an infinite distance away.

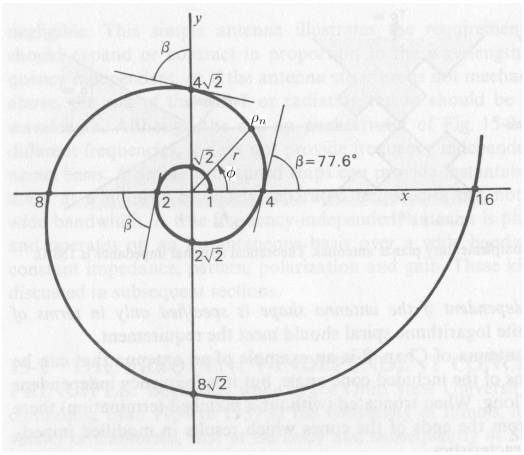

Figure 2.3: An LS with intersecting radial line r [8].

We will later calculate the geometric relationship governing these values.

The equation for ϕ as a function of the radial distance ρ in polar coordinates is as follows:

$$\phi = \phi_0 + (\tan \beta) \ln \rho \tag{2.1}$$

Figure 2.4: An cut away image of a nautilus shell [16].

When the LS is rotated by an angle ϕ, the resulting structure is a scaled (and rotated) version of the original structure. Jacques Bernoulli described this behavior in his treatise on the LS, and requested it be engraved on his tombstone: "Although changed, I rise again the same" [17]. This SS aspect of LS's can explain why they are so often witnessed in nature. For example, as the mollusk inside the nautilus shell grows in size, most of its features scale

in portion to one another [17]. The protective shell that is secreted as the mollusk develops provides a historical record of a scaled-down version of the mollusk's younger days (Figure 2.4)

The relationship between the LS antenna and geometric progression can be seen by revisiting Equation 2.1 and raising both sides of the equation to the exponent:

$$\rho = k\, e^{\frac{\phi}{\tan\beta}} \tag{2.2}$$

where $k = 1/\frac{\phi_0}{\tan\beta}$. Defining the growth rate of the spiral as

$$c = \frac{1}{\tan\beta} \tag{2.3}$$

we obtain the simple equation in polar coordinates:

$$\rho = k\, e^{c\phi} \tag{2.4}$$

By convention $\rho_n > \rho_{(n-1)}$ and therefore c is a negative value indicating that the spiral is exponentially decaying as n increases. Truncating ρ_0 to some large but finite value with an angle of $\phi = 0$, we evaluate Equation 2.4 at every $\phi = 2\pi$ turn, we construct Table 2.1.

ϕ	ρ
$\phi = 0$	$\rho_0 = \rho_0 e^{c0} = \rho_0$
$\phi = 2\pi$	$\rho_1 = \rho_0 e^{c2\pi} = \rho_0 \tau$
$\phi = 4\pi$	$\rho_2 = \rho_0 e^{c4\pi} = \rho_0 \tau^2 = \rho_1 \tau$
$\phi = n2\pi$	$\rho_n = \rho_0 e^{cn2\pi} = \rho_0 \tau^n = \rho_{n-1} \tau$

Table 2.1: Values of ρ at points on a radial line intersecting with an LS.

Table 2.1 indicates that values for ρ at the points of intersection between a radial line and an LS create a geometric progression of

$$\rho_n \quad = \quad \rho_{n-1}\,\tau \quad = \quad \rho\,\tau^n \tag{2.5}$$

where

$$\tau = e^{c2\pi} \tag{2.6}$$

2.2.2 Log Periodic Antennas

Self-similarity appears to be necessary, but not sufficient, for frequency independent radiation patterns. Just as the orientation of the mollusk within its shell changes as it grows, the polarization of the LS antenna's radiation patterns unsurprisingly rotates as one moves across the frequency band [6]. However, the science that drives the SKA would generally prefer two linear polarizations that are stable with frequency variations [1]. The demand for wide bandwidth precludes the insertion of a relatively narrow band orthomode transducer (OMT) to obtain two linear polarizations. Fortunately, log periodic (LP) antennas can achieve linear polarization by confining the elements within an angle far smaller than the angle of 2π required by the spiral.

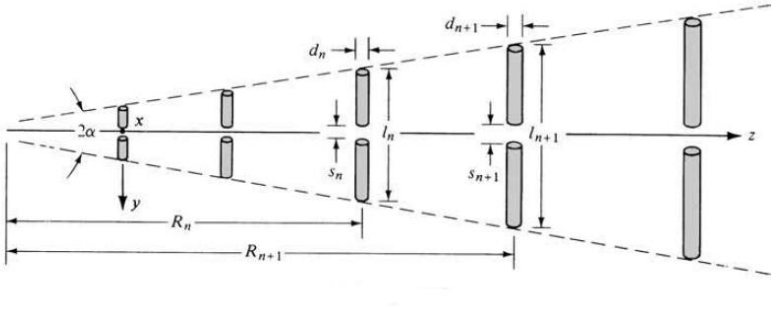

Figure 2.5: A log period dipole array [18].

Log Periodic Dipole Array

In the log periodic dipole array (LPDA) antenna, shown in Figure 2.5, the resonant dipole elements are placed distances R_n from the apex of the angle. It is between this angle of 2α that the length of the elements is constrained. Similar to the relationship amongst the LS's values for ρ_n along a straight line, the location of the LPDA elements obeys a geometric

progression where $\tau = \frac{R_n}{R_{n+1}}$. In fact, similar to the growth of the mollusk, all dimensions of the LPDA elements scale by the same factor:

$$\tau = \frac{R_n}{R_{n+1}} = \frac{l_n}{l_{n+1}} = \frac{d_n}{d_{n+1}} = \frac{s_n}{s_{n+1}} \tag{2.7}$$

Log Periodic Cells

Referring again to Figure 2.5, a single "cell" can be defined as the region bound by dimensions R_n to R_{n+1}. If there exists a frequency f_n excited precisely at R_n, it will be related to frequency f_{n+1} excited at location R_{n+1} by:

$$\frac{f_n}{f_{n+1}} = \frac{1}{\tau} = \frac{R_{n+1}}{R_n} \tag{2.8}$$

(It should be noted that although the initial starting point for first element, $n = 0$, varies amongst authors, τ will always be defined to have a value less than one.)

The two similar structures located at R_n and R_{n+1} will have matching radiation properties at frequencies f_n and f_{n+1}, respectively. Between f_{n+1} to f_n, however, the radiation properties are bound to exhibit some variation. If the variation over this period is kept to a minimum, the variation over the entire band can also be kept to a minimum, as this period is repeated in the next cell from f_{n+1} to f_{n+2}, and then the next from f_{n+2} to f_{n+3}, and so on.

One method to reduce the periodic variations is to minimize the relative bandwidth covered between f_n to f_{n+1}. This can be done by increasing τ toward the limiting value of $\tau = 1$, at which there is no periodic variation but the bandwidth is reduced to the single frequency $f_n = f_{n+1}$. Additionally, as τ is increased, the entire length of the structure in the z direction is increased. LPDA antennas do not have frequency independent phase center locations, so this increase in total LPDA length will result in greater frequency dependent behavior of the phase center [14].

Log Periodic Radio Astronomy Elements

Radio light collected by the parabolic dish focuses at one point, regardless of the frequency of that light. The phase center of the antenna should be placed at this focal point. Although some of the defocusing effects resulting from phase center frequency variation away from the focal point have been found to be acceptable [13], it is preferable to localize the phase center across the frequency band. The ATA feed (Figure 1.5) has been implemented in the Allen Telescope Array dishes with a mechanical device that translates the position of the antenna along its axis of radiation.

Many astronomical measurements are observed within a narrow portion of the feed's entire bandwidth. Therefore, the antenna can be positioned so that the phase center location for the frequency band of interest is at the focal point of the dish. However, this type of mechanical device may be difficult to implement and maintain in the thousands of SKA radio dishes.

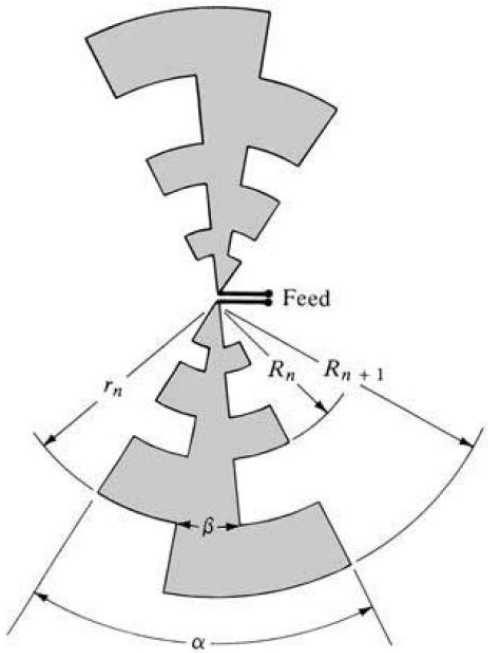

Figure 2.6: Curved trapezoidal tooth LP antenna [18].

Frequency invariance of the phase center can be achieved by placing the antenna in

a single plane orthogonal to the direction of radiation. A common antenna of this type, sometimes called the curved trapezoidal tooth (CTT) LP antenna, is shown in Figure 2.6. The symmetry of this planar antenna dictates the radiation of two symmetrical lobes, normal to the plane of the antenna.

Effective radio astronomy antennas must efficiently illuminate the radio dish by radiating the great majority of its energy in the direction of the dish. This requirement rules out completely planar designs of FI antennas. The high sensitivity requirement for radio astronomy also prohibits the 3 dB power loss due the placement of an absorption cavity on one side of the planar antenna, as is often done to generate lobes in solely one direction [19].

2.2.3 Self-Similar Elements Over a Ground Plane

A current source placed a certain height h above ground plane (GP) induces an "image" current source with an opposite transverse component and a parallel normal component, an equal distance below the GP. When the height is arranged such that the fields radiating from the "two" current sources are adding constructively in the direction of interest, the GP is behaving like a reflector. A height of $h = \frac{\lambda}{4}$ will result in constructive inference for a simple current element parallel to the GP [8].

For FI antennas, as λ changes, the value of h must also change. An early implementation incorporating a GP into an FI antenna was published by DuHamel in 1959 [20]. This antenna designed for communications in the 3 MHz to 30 MHz range (Figure 2.7) shows variation in the value of h from a minimum at the highest frequency components near the feedpoint on the ground level, to a maximum h at the lowest frequency elements. Adopting the progression of n indicated in Figure 2.7 it would be found that $\tau = \frac{h_{n+1}}{h_n}$.

The QSC feed (Figure 1.6) and the Eleven feed (Figure 1.7) also employ the method of height variation of the radiating elements above the GP in order to achieve gain in the dish's direction. Unfortunately, the need to vary the height of the resonant elements may introduce manufacturing complexity, particularly on the scale of production for the SKA.

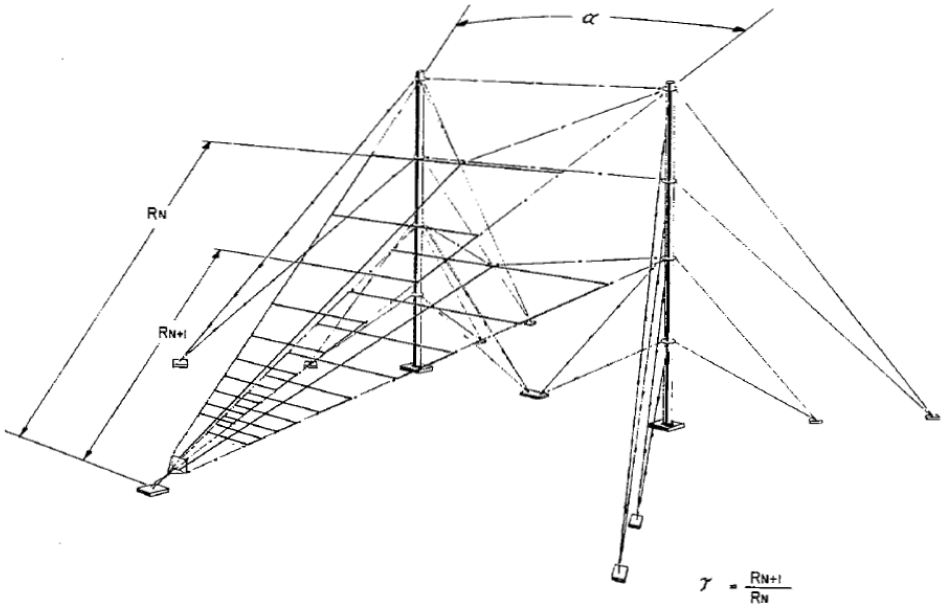

Figure 2.7: 3 MHz to 30 MHz FI antenna over a ground plane [20].

2.3 Self-Complementary

Babinet's principle for complementary structures at optical frequencies can be summarized as follows: the diffraction pattern of shadow and light resulting from illumination of an opaque screen by a point light source, plus the diffraction pattern resulting from a subsequent illumination of the screen's complement, will together combine to form the pattern of undisturbed light that would have resulted from a single point source illumination if there was no screen there at all [8]. That is, the two resultant diffraction patterns are themselves complementary. At lower frequencies, the application of this principle to the electromagnetic vector fields, known as Booker's relation, states that one can witness the same phenomena by replacing an opaque screen with a "perfect electric conductor" (PEC) which is opaque to radio and microwave light [8]. A result of Booker's relation is that the impedances of the two complementary structures are indeed complementary as well. Applying this result for impedances to two complementary structures that are composed of

PEC and vacuous air, it is found that

$$Z_{PEC}\, Z_{air} = \frac{\eta^2}{4} \tag{2.9}$$

Where η is the impedance of free space.

Mushiake observed that the equation can be further simplified when the structure is SC [6]. Equating $Z_{PEC} = Z_{air}$ in Equation 2.9 and taking the square root of both sides, we obtain

$$Z_{PEC} = Z_{air} = \frac{\eta}{2} \tag{2.10}$$

Rumsey applied Mushiake's findings to the study of FI structures. Although the resulting FI impedance behavior may not be apparent at first when simplifying Equation 2.9 into Equation 2.10 for SC structures, a quick example elucidates this.

Equation 2.9 can be used to calculate the impedance of a slot in waveguide, for example, when the slot is the length of a resonant dipole with an impedance of Z_{dipole}:

$$Z_{slot} = \frac{\eta^2}{4\, Z_{dipole}} \tag{2.11}$$

In the case that the dipole is a purely resonant half wavelength element, $Z_{dipole} = 67 + j0\Omega$ at the feedpoint. The slot impedance across its narrow midpoint will be found as $Z_{slot} = 530 + j0\Omega$. If the frequency of operation is slightly scaled, while the dimensions of the dipole remain unchanged, Z_{dipole} will no longer be resonant and correspondingly, Z_{slot} will also change with frequency by Equation 2.11.

Alternatively, regardless what frequency resonants in a SC structure, application of Equation 2.10 will always result in an FI impedance: $\frac{\eta}{2} \approx 188.5\,\Omega$. The practical limitations in building and feeding structures requires deviation from perfect SC and therefore from the ideal constant impedance [6].

2.4 Active Region

The AR is the portion of the antenna at which the majority of the power at a given frequency radiates, usually by the placement of resonant elements in the region. In FI structures the location and size of the AR must scale with frequency. This can be accomplished if the antenna behaves like a low-pass filter for a given narrow frequency range of interest. For an example we examine a case when a broad pulse of power with the majority of its power spectral density at 5 GHz is transmitted by an LPDA antenna designed to operate in the 1 GHz to 10 GHz frequency range.

For reasons that will soon become apparent, the antenna is fed in the region where the highest frequency elements resonate. This region is composed of electrically small dipole elements relative to the 60 mm wavelength of the 5 GHz signal. These elements may appear as capacitive stubs positioned in a periodic fashion along a transmission line and is referred to as the "transmission line region" (TLR) as the energy appears to not radiate in this region. As the signal travels away from the feed point along the beam of the antenna at a velocity near the speed of light, it will eventually encounter dipole elements of length $l_n \approx \frac{\lambda_{5GHz}}{2}$. At this time the dipole elements will no longer appear small, but will instead resonate at the 5 GHz frequency and radiate in this region: AR_{5GHz} [6].

The low-pass filter behavior can now be seen if we contrast the above scenario to that encountered by a 1 GHz signal. Initially at the feedpoint, the dipole elements will similarly appear electrically small to the 300 mm wavelength energy that propagates along the TLR. This transmission line mode will continue past the area where the 5 GHz energy radiated until it reaches the active region and resonates in the dipole elements of length $l_n \approx \frac{\lambda_{1GHz}}{2}$. One can then describe the behavior at the AR_{5GHz} as a low-pass filter that only allowed frequencies below 5GHz to pass while attenuating frequencies above 5 GHz. However, the resistive element at 5 GHz is one of radiation resistance, rather than a resistor that generates random heat.

2.4.1 End Effect

The frequencies at which the antenna appears to be both SS and SC are limited by the dimensions of the inner most and outer most elements. The low frequency limit is approximately related to the wavelength at which the largest elements are of a length $l_{ideal\_big} = \frac{\lambda_{low}}{2}$. The high frequency limit is the wavelength at which the feeding structures (such as co-axial cables) and the smallest elements have sufficiently small dimensions such that they can be modeled as lumped elements rather than distributed elements. The lumped element approximation can take place when the large dimension of a component is approximately $l_{small} \approx \frac{\lambda_{high}}{16}$ [19]. Operation below this upper frequency limit avoids unintentional radiation from the feeding structures in the highest frequencies and sets up these high frequencies in a TLR prior to radiation in an AR.

Similar to the case of the high frequency limit, the lower bound is not in fact determined by the size of the resonant frequency of the largest element, as approximated earlier. In practice, the largest element's length is $l_{big} = \epsilon_{ee} \frac{\lambda_{low}}{2}$ where the end effect coefficient $\epsilon_{ee} \approx 1.5$, which is roughly the largest element at which no reflected energy appears.

If a traveling wave contains spectral content that resonates in the largest element at the antenna's edge, as would be the case when $\epsilon_{ee} = 1$, its is reasonable to imagine that this AR will radiate in a manner that is not similar to the inner ARs. Specifically, the edge of the antenna may appear like an open circuit that will reflect the energy back toward the feed point. As this low frequency signal propagates back along the antenna, all the dipole elements will appear increasingly electrically small and there will be no low pass filter effect to attenuate this reflected content. The superposition of the forward and reflected wave will create a standing wave pattern that will not scale with the logarithm of the frequency, and will thus introduce frequency dependent properties.

Extending the length of the largest element by a factor of $\epsilon_{ee} \approx 1.5$ larger than a half wave dipole will usually permit the lowest frequency signals to sufficiently radiate prior to the antenna's outer edge. Elimination of the "end effect" (also known as the "truncation effect") by operating in the proper frequency range can allow for an antenna to appear both

SS and SC because the currents dissipate prior to reaching the antenna's edge [6]. The "end effect" limits bandwidth in broadband antennas, such as the discone antenna, that do not have an AR that sufficiently radiates currents prior to the antenna's edge [21].

Chapter 3

The Proposed Antenna

The type of antenna feed selected for SKA operation in the 1 GHz to 10 GHz frequency range, introduced as a Wide Band Single Pixel Feed (WB+SPF) in Section 1.1, has drawn increasing attention. In this chapter we will describe a new WB+SPF antenna proposed as a solution for the SKA's 1 to 10 GHz range. The wide bandwidth of the new WB+SPF antenna introduced in this thesis is achieved by employing the frequency independent design principles discussed in Section 2.2 through Section 2.4, which can be identified in other WB+SPF antennas currently proposed for the SKA, including the ATA feed [9],QSC feed [10], and the Eleven feed [22], all introduced in Section 1.3. These LP antennas efficiently illuminate the radio dish with a single main lobe. This required unidirectionality of the antenna rules out the usage of entirely planar FI antennas, as discussed in Section 2.2.2. Scaling the LP elements into three-dimensional space [23], potentially over a ground plane [20], is the present method used to obtain directional FI antennas.

We instead propose confining these often complex LP elements into a single plane, while the ground "plane" takes on a three-dimensional form. Planar LP patterns permit low-cost implementations, including printed circuit board methods and water jet cutting technology, without requiring the introduction of a complicated scaffolding to support the LP elements in 3-D. Various technologies such as metal spinning can be cost-effectively shape the ground "plane" into a 3-D surface. This low-cost WB+SPF solution would scale

well in the implementation of the thousands of antenna feeds that the SKA demands. In this chapter we also introduce a previously unreported LP design: the log periodic log spiral (LPLS) antenna.

3.1 Preliminary Design Work

Prior to the development of the LPLS design, we initially placed a non-planar ground "surface" beneath a well-developed FI planar arrangement: the CTT LP antenna. A two-arm CTT LP antenna was shown in Figure 2.6. The design work for the antenna described here was conducted using the Microwave Studio package by Computer Simulations Technology (CST), electromagnetic field solving software which will be discussed in Section 4.1. Initial results of the computer simulations of the ground surface incorporated under the CTT LP antenna (some of which will be discussed in Section 4.2) indicated that a non-planar ground surface was promising, and at that time, design of the LPLS and the non-planar ground surface began in tandem.

3.2 Design Details

The WB+SPF antennas proposed for the SKA are all similar in their geometry of multiple "arms", composed of the SS elements that characterize an LP structure. All of these arrangements of the "arms" have some form of rotational symmetry, not unlike the petals of a flower. Tom Landecker of the National Research Council's (NRC) of Canada, Dominion Radio Astrophysical Observatory (DRAO) first suggested the use of the term "petal" to describe the "arms" that compose the LP arrays [24] and we will adopt this convention here. The LP antenna that we propose here will be composed of four petals that will be referred as $Petal_1$ through $Petal_4$.

3.2.1 Log Periodic Log Spiral

Figure 3.1a shows a computer-aided design (CAD) of a four-arm LPLS antenna above the ground surface modeled in CST's Microwave Studio, and Figure 3.1b is a prototype of the LPLS with a ground surface mounted for measurement. The zig-zag elements of $Petal_1$ and $Petal_4$ progress predominately in the vertical direction, parallel to the y-axis, and the zig-zag elements of $Petal_2$ and $Petal_3$ progress predominately in the horizontal direction, parallel to the x-axis. $Petal_1$ through $Petal_4$ are attached to ports 1 through 4, respectively. The antenna operates in a differential mode between $Petal_1$ and $Petal_4$ and between $Petal_2$ and $Petal_3$, such that the signals received at port 1 and port 4 will be 180 degrees out of phase from one another, and there will be a 180 degree phase difference between the signals received at port 2 and port 3 as well.

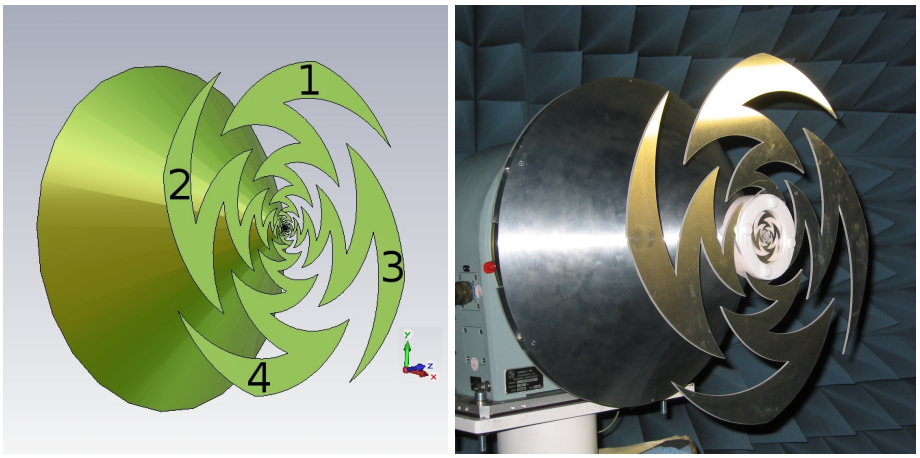

(a) CAD model (b) Prototype

Figure 3.1: Petal numbers labeled on (a) CAD model and b) the prototype.

Each "zig" or "zag" of a single petal can be considered a roughly half-wave resonant element extending orthogonally from the direction that the petal progresses. An examination of the surface currents in Section 3.3 will confirm this approximate half-wave resonance. The dipole-like zig-zags radiate in a manner similar to a collinear array of dipoles, such that the E-field component of the excitations received at ports 1 and 4 is predominantly horizontally polarized or parallel to the x-z plane, while the E-field component received at

ports 2 and 3 is predominantly vertically polarized or parallel to the y-z plane, achieving two linear orthogonal polarizations.

As with all LP structures, the angular extent of the "cells", in this case the zig-zags, are confined within the angle α. In polar coordinates, the equation for one side of the nth "zig" or "zag" of a single petal is the basic equation for a logarithmic spiral, with some constant rate of decay c, and bound by α

$$\rho = \rho_{(n-1)}\, e^{\pm c\,\phi}\Big|_{\mp\frac{\alpha}{2}}^{\pm\frac{\alpha}{2}} \tag{3.1}$$

Equation 3.1 is applied for n iterations, from 1 to $n = max$, representing the total number of zig-zags. The even values of n define a "zig" using the upper $+$ or $-$ signs in Equation 3.1, and odd values of n define a "zag", using the lower $+$ or $-$ signs in Equation 3.1. The extreme points at the edges of the nth "zig" or "zag" are defined by points $\rho_{(n-1)}$ and ρ_n. The other side of the petal can be obtained by rotating Equation 3.1 by $\phi = \frac{\pi}{i}$ radians for a total of i petals, as can be seen in Figure 3.2. Finally, the arcs that define the outer and inner edges of a petal are determined by $\rho = \rho_0\,\frac{\pi}{i}$, and $\rho = \rho_{max}\,\frac{\pi}{i}$, respectively, to complete the planar surface. The remaining petals can be found by rotating $Petal_1$ by $\frac{2\pi}{i}$. Note that it is permissible for α to be in the range of $0 < \alpha < \frac{2\pi}{i}$, unlike the CTT design in which case $\alpha \geq \frac{\pi}{i}$ would result in the petals short circuiting against one another. This additional flexibility of LPLS design extends the limits of one of the design variables, potentially permitting a reduced radial distance for a given arc length of a resonant element.

3.2.2 Scaling Factor for the LPLS

As is the case in Equation 2.5 for the LS antenna, the following is true for the LPLS antenna

$$\rho_n \quad = \quad \rho_{n-1}\,\tau \quad = \quad \rho\,\tau^n \tag{3.2}$$

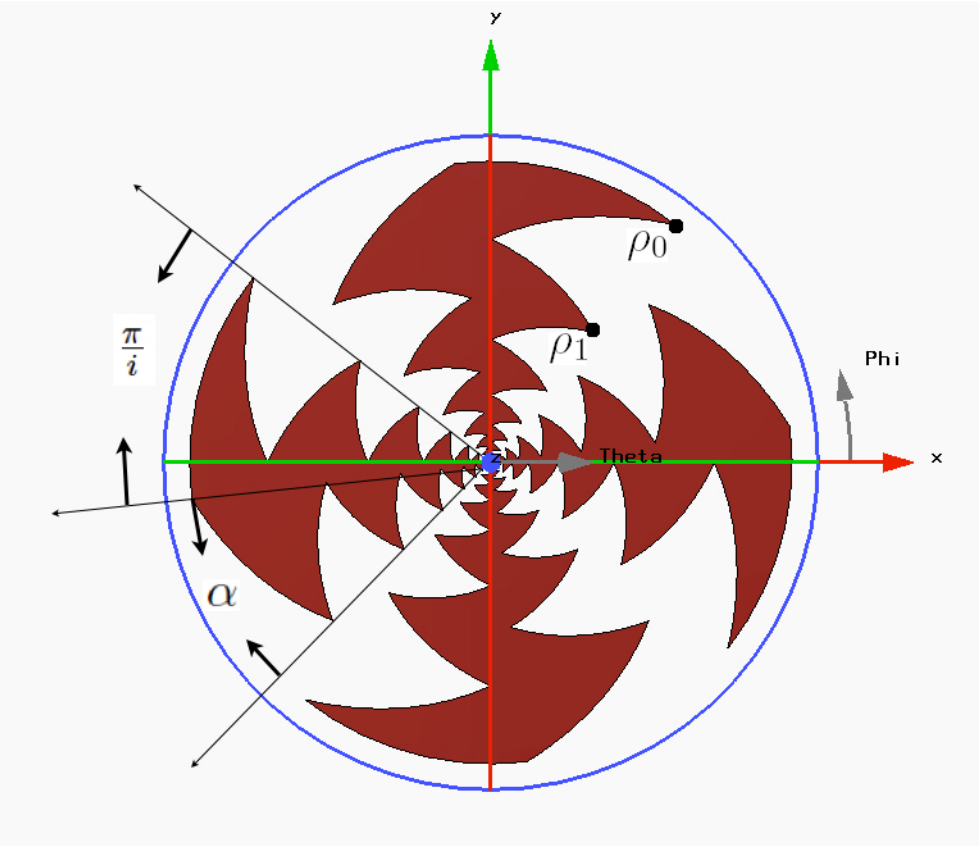

Figure 3.2: Geometry of a generic LPLS antenna.

However, τ now differs from the logarithmic spiral's τ of Equation 2.6 by the replacement of the $\phi = \alpha$ instead of $\phi = 2\pi$, such that

$$\tau = e^{c\,\alpha} \tag{3.3}$$

Revisiting Equation 2.3, we see that c, the rate of exponential spiral decay, is dependent only on the angle β, which is the constant angle that motivates the name "equiangular spiral". However, Equation 3.3 shows that τ is dependent upon both c and α. We sought to investigate the properties of the antenna by adjusting only one of these variable values, while the remaining variables are held constant, so it was most useful to utilize the scaling factor with the fewest dependencies. For this reason, we used c to define the growth (decay) of the LPLS, as do many articles on LS antennas, allowing for independent variation of rate of decay c and the arm angle α. However, this is in contrast to many articles on LP antennas which use τ to describe LP antennas.

3.2.3 Non-planar Ground "Plane"

The specific case of a series of current sources of length l_n, placed at heights h_n above a GP, was introduced in Section 2.2.3. In general, constructive interference of the radiated fields from the source and its image at a distance h_n below the GP will be found when the source is at a height of

$$h_n \quad = \quad k_1\, l_n \tag{3.4}$$

where k_1 is a constant in the general case and, for example, equals $\frac{1}{2}$ or a quarter-wavelength in the case that the element of length l_n is a half-wave dipole [8]. The function that describes the shape of the ground "surface" was determined by finding the arc length of Equation 3.1 from $\frac{\alpha}{2}$ to $-\frac{\alpha}{2}$ for the nth element

$$l_n \;=\; \int_{-\frac{\alpha}{2}}^{\frac{\alpha}{2}} \sqrt{\rho^2 + \left(\frac{d\rho}{d\phi}\right)^2}\, d\phi \;=\; \sqrt{1+c^2}\,\frac{\rho_{(n-1)}}{c}\, 2\sinh\left(\frac{c\,\alpha}{2}\right) \;=\; k_2\,\rho_{(n-1)} \tag{3.5}$$

for some constant k_2. Combining Equation 3.4 and Equation 3.5 with Equation 3.2 we find a linear relationship between the height h_n and the radial distance ρ_n for the nth element, specifically

$$h_n = k_1 k_2 \frac{\rho_n}{\tau} \tag{3.6}$$

determining that a conical surface is the appropriate shape for the ground surface beneath the petals.

3.3 Surface Current Investigations

An analysis of surface currents played a large role in the iterative design process of the LPLS over a ground surface. It can be shown that a spatial Fourier Transform conducted upon the surface currents on the antenna results in the far-field radiation pattern [18]. In this section we will look at CST simulation results as a way of explaining the operation of the LPLS.

3.3.1 Differential Currents

The differential currents on this antenna can be explained by the 180 degree rotational symmetry between the two petals that compose one linear polarization. The arrows in Figure 3.3 represent an incident electromagnetic (EM) wave with an E-component in the y-direction illuminating the antenna.

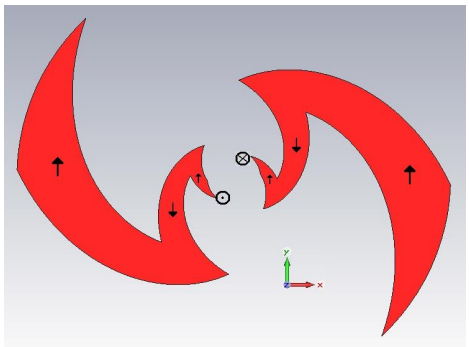

Figure 3.3: Representation of an incident EM wave with an E-component in the y-direction.

Although the surface currents are excited in parallel directions on the two petals of interest, the induced currents reach the center of the antenna with their orientation 180 degrees out of phase, one going into the page and the other out of the page, as indicated by the dot and the cross, respectively, at the center of the antenna in Figure 3.3.

3.3.2 Active Region

A depiction of the AR, two different frequencies (Figure 3.4a at 1 GHz and Figure 3.4c at 2 GHz) due to the excitation of one linear polarization ($Petal_2$ and $Petal_3$), as well as the approximate dimensions of the AR is shown in Figure 3.4. These instantaneous snapshots at the approximate current maxima reveal that there is little current beyond the respective resonant sections at 1 GHz and 2 GHz. As we increase the frequency from 1 GHz to 2 GHz, we see that the AR reduces in size accordingly. This reduction of the aperture area with the reduction in wavelength allows for a consistent beamwidth across the band which can be shown by performing spatial Fourier Transform (FT) on the surface currents [18]. Should the entire antenna be active with surface currents across the operation bandwidth, the antenna would appear increasingly electrically large at the higher frequencies such that the FI beamwidth properties would be sacrificed.

Additionally Figure 3.4 shows the presence of an AR, internal to the physical boundaries of the antenna, confirming that the LPLS does indeed behave as a traveling wave structure in the $\pm x$ direction characterized by the dissipation of the currents prior to reaching the edge of the antenna in the $\pm x$ directions. Meanwhile the structure appears to resonate in the $\pm y$ direction, in this case when the petals that progress along the x-direction are excited.

3.3.3 Resonant Currents

Another depiction of CST simulation result surface currents at 1 GHz is shown in Figure 3.5. In this more sparsely plotted depiction of the surface currents, we again see that currents

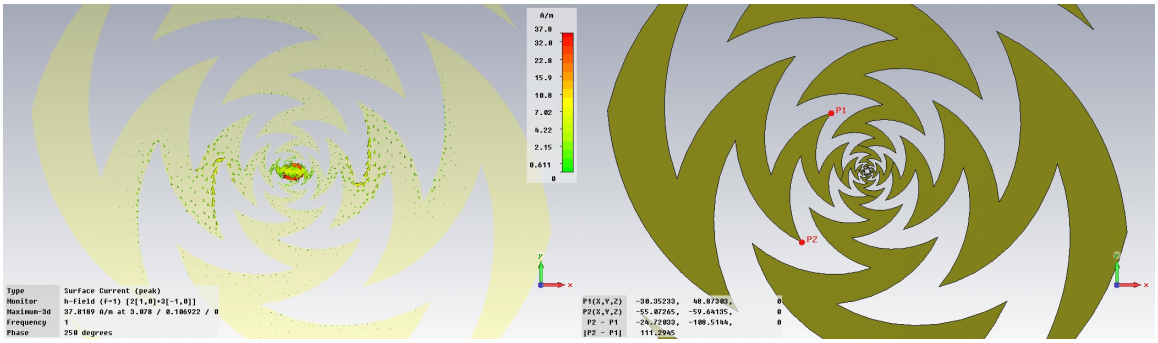

(a) Surface currents at 1 GHz (b) Dimensions at 1 GHz

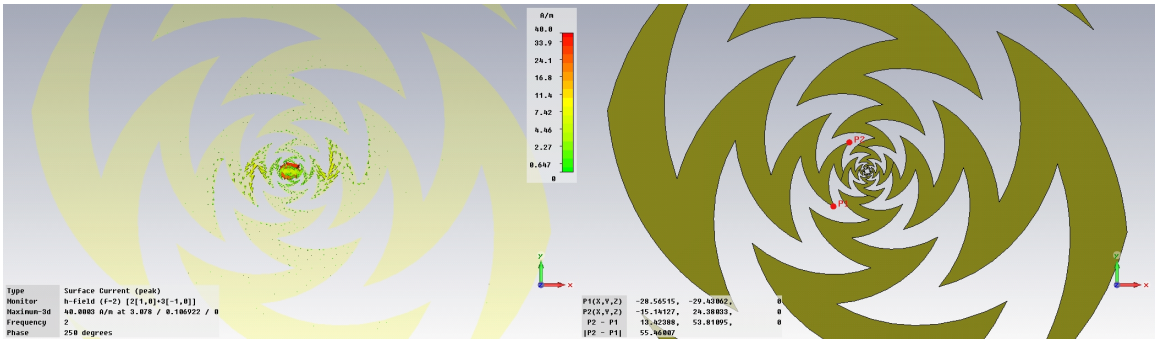

(c) Surface currents at 2 GHz (d) Dimensions at 2 GHz

Figure 3.4: Vectorial representation of surface currents and rough dimensions of the AR.

quickly dissipate after the zig-zag at which they appear to resonate. On this particular resonant "zig" (the fourth one from the outer edge of the antenna) an approximate sine wave distribution of the surface currents appears, with the relatively higher current intensity in the middle of the "zig", while the current approaches zero at the end of the "zig". This approximate sine wave distribution of surface currents is characteristic of a resonant dipole structure and confirms our approximate analysis of such in Section 3.2.

3.4 Design Parameters

The following variable values were fixed early in the design process:

- the conical ground surface was fixed at 45 degrees and left to be investigated in later research

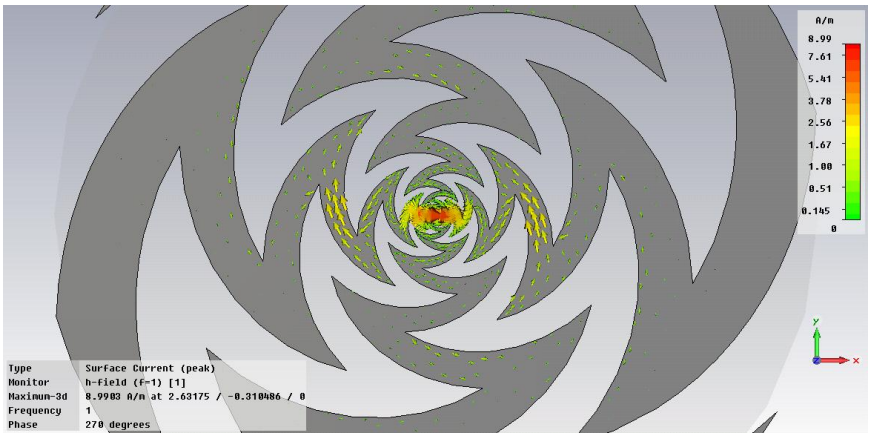

Figure 3.5: Approximate sin wave distribution of the surface currents modeled in CST and scaled in dB at 1 GHz.

- the number of petals i was set to 4 in order to achieve two linear polarizations, each composed of two petals.

The design variables for the LPLS antenna were limited to these below, and through an iterative process, a solution was determined at these values

- the inner-most radial distance of the petal $\rho_{max} = 3$ mm
- the outer-most radial distance of the petal $\rho_0 = 225$ mm
- the rate of exponential growth of the spiral $c = -.34$
- the arm angle of the zig zags, $\alpha = 66$ degrees.

Employing Equation 3.1 and Equation 3.6, a script defining the LPLS structure and conical ground surface was written in Visual Basic for Applications (VBA). Utilization of the scripts allowed for a rapid construction of the computer-aided design (CAD) model. The model then underwent a CST simulation to determine its radiation properties and S-parameters. Following a simulation, the collected data was analyzed and interpreted for a given set of design variables in regard to the overall design goals. A single adjustment would then be made to the design variable that appeared to be a limiting factor to the attainment of the design goals, and other testing iteration would begin. The design goals

were driven by the SKA science requirements, and will be discussed in tandem with the results in Chapter 4.

Chapter 4

Antenna Simulation

4.1 Modeling Software

The Microwave Studio package by CST was utilized to model the radiation properties of the WB+SPF. CST solves Maxwell's equations for the complex 3-D electromagnetic fields that surround the antenna under test (AUT), as well as the resulting far-field radiation patterns. CST's time domain analysis method stimulates the antenna with a pulse of 0 dBm power contained in a very short duration of time [25]. The FT relationship reveals that the increasingly narrow the pulse of energy is in the time domain, the increasingly broad its constitute spectral components are in the frequency domain. CST's time domain analysis excites the antenna with an appropriately brief voltage pulse such that all the spectral components in the bandwidth of interest are excited. Thus, a single excitation can provide the very large bandwidth of interest for the WB+SPF. After the energy of the original excitation pulse has reduced to a specified dB value, the simulation is terminated and the FT is performed to provide the simulated data in the frequency domain.

We additionally employed Advanced Design System (ADS) 2006 software to simulate circuits and RF systems utilizing ADS's S-parameter simulator. Unlike CST, this version of ADS does not solve Maxwell's field equations. We instead used ADS to analyze S-parameter data previously measured with a vector network analyzer (VNA). This was accomplished

by inserting the matrix of measured data as a network block into an ADS model of a RF linear circuit.

All the data and results presented in the chapter are results from computer simulations. Real measurement data will not be presented until Chapter 5.

4.2 Co-polar and Cross-polar Investigations

As described in Section 3.1, we first introduced the non-planar ground surface to a well-developed FI planar arrangement: the CTT LP antenna. The initial CTT simulations resulted in far-field radiation patterns with elliptically shaped lobes, where the E-plane beamwidth is dissimilar to the H-plane beamwidth. Although design changes to the CTT LP antenna could result in equal beamwidths for the E-plane and H-plane, we will take advantage of the discrepancy here as a convenient visual representation of the distinction between the two orthogonal linear polarizations of the antenna. We now utilize these patterns to gain a better understanding of the relationship between the coordinate system of our simulation and the vertical and horizontal polarizations. Note that the elliptically shaped lobes of the radiation plots shown in this section are not those of the LPLS antenna.

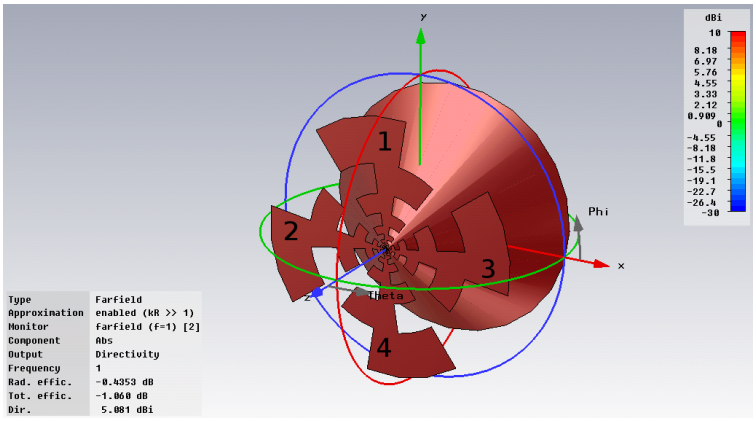

Figure 4.1: CTT LP antenna over a ground surface.

Figure 4.1 shows a four-arm CTT LP antenna modeled in CST with Theta (θ) and Phi (ϕ) labeled as is convention in spherical coordinates. The beams of $Petal_1$ and $Petal_4$ extend

vertically, parallel to the y-axis and the beams of $Petal_2$ and $Petal_3$ extend horizontally, parallel to the x-axis, just as they do in the case of the LPLS antenna. As is also the case with the LPLS antenna, $Petal_1$ through $Petal_4$ of the CTT LP antenna are attached to ports 1 through 4, respectively. In the CST simulation, each of the four ports were independently excited, one at a time, with identical broadband signals.

4.2.1 Differential Far-field

For both the CTT and the LPLS, the antenna operates in a differential mode as discussed previously. Due to the linearity of the Fourier Transform, it is expected that this differential mode of operation in the surface currents can be achieved in the far-field radiation pattern by subtracting the far-field pattern radiated by $Petal_1$ from that radiated by $Petal_4$ to result in predominantly horizontally polarized E-field components. Similarly, subtracting the far-field pattern radiated by $Petal_2$ from that radiated by $Petal_3$, one should find the predominantly vertical E-field components. CST offers post-processing functionality that can subtract complex vector fields to determine what we will refer to as the "differential far-field" patterns, and can be utilized to confirm the above expectations.

4.2.2 Polarization of $Petal_2$ and $Petal_3$

The 3-D differential far-field patterns for the vertical and horizontal E-field components and their soon-to-be-investigated assignment of co-polarized (co-pol) and cross-polarized (x-pol) fields radiated by $Petal_2$ and $Petal_3$ of the CTT antenna are shown in Figures 4.2a and 4.2b, respectively. As expected, the vast majority of the energy radiated by the vertical elements of $Petal_2$ and $Petal_3$ is vertically polarized, resulting in a 10 dB difference between peak vertical E-field component compared to the peak horizontal E-field component.

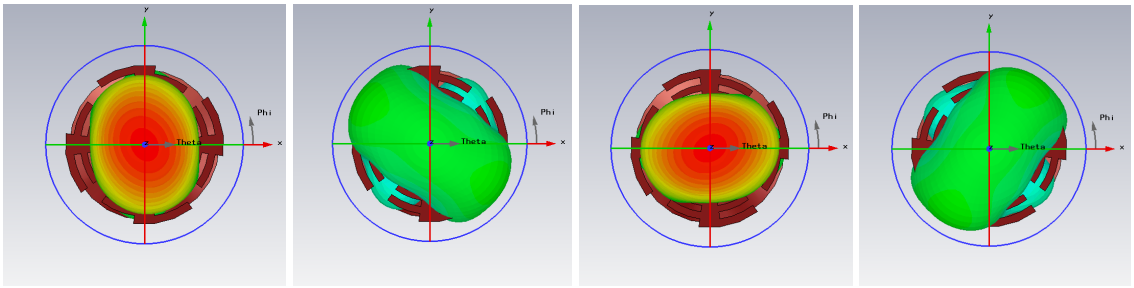

(a) Vertical (co-pol) (b) Horizontal (x-pol) (c) Horizontal (co-pol) (d) Vertical (x-pol)

Figure 4.2: CTT co-pol and x-pol differential radiation patterns, (a) and (b) from simulation of $Petal_2$ and $Petal_3$, and (c) and (d) from simulation of $Petal_1$ and $Petal_4$. Note these are not the LPLS radiation patterns.

4.2.3 Co-pol and X-pol E-Field Components

The vertical and horizontal far-field components are calculated in CST using Ludwig's third (Ludwig 3) definition [26]:

$$E_{vert} = E_\theta \sin\phi + E_\phi \cos\phi \tag{4.1}$$

$$E_{hor} = E_\theta \cos\phi - E_\phi \sin\phi \tag{4.2}$$

where E_θ and E_ϕ have the usual definitions of the total E-field, $E(\theta_0, \phi_0)$, at a given location (θ_0, ϕ_0), decomposed into the orthogonal vectors $E(\theta_0, \phi_0)\hat{\theta}$ and $E(\theta_0, \phi_0)\hat{\phi}$, respectively. The assignment of co-pol and x-pol E-field components can be related to the vertical and horizontal components by Ludwig 3. As described in the CST manual,

> "Depending on the direction of the electric field of the excitation mode, vertical and horizontal have to be linked with cross polarization and co-polarization. The vertical component always directs in y-direction. Therefore, in the case of E_y as the main waveguide mode component, the co-polarization is identical to E_{vert} and cross polarization is identical to E_{hor}." [25].

This example of E_y as the main waveguide mode is analogous to our above description of the radiation from $Petals_2$ and $Petal_3$ as parallel to y-z plane. For the antenna's alignment

in Figure 4.1, the principle polarization plane is defined as $\phi = \frac{\pi}{2}$ and $\theta = 0$ in spherical coordinates or as the y-z plane normal to the x axis in cartesian coordinates. As previously discussed, the monopole elements of $Petals_2$ and $Petal_3$ are parallel to this plane, so the co-pol field is defined as E_{vert}, while the x-pol field is E_{hor}. If $E_{hor} = 0$, one would expect an absence of x-pol field components, and this definition is consistent with the "necessary and sufficient condition for zero cross polarized surface currents"[26]:

$$E_\theta \sin\phi = E_\phi \cos\phi \tag{4.3}$$

4.2.4 Polarization of $Petal_1$ and $Petal_4$

We can now adopt the convention of referring to E_{vert} as the co-pol and E_{hor} as the x-pol radiation from $Petals_2$ and $Petal_3$; however, this convention is only relative to the orientation of $Petal_2$ and $Petal_3$, so it cannot be applied to the fields radiated from $Petals_1$ and $Petal_4$. The orientation of the monopoles elements on $Petal_1$ and $Petal_4$ are rotated 90 degrees from those of $Petals_2$ and $Petal_3$. This 90 degree rotation can be obtained in the spherical coordinate system for our model by replacing $\phi = \frac{\pi}{2}$ with $\phi = 0$. Now the principle plane of interest is defined as $\phi = 0$ and $\theta = 0$ in spherical coordinates or as the x-z-plane normal to the y axis in cartesian coordinates. The monopole elements of $Petal_1$ and $Petal_4$ are parallel to this plane, so co-pol field for $Petal_1$ and $Petal_4$ is now defined by E_{hor}, while the x-pol field is E_{vert}.

Note that when Equation 4.1 and Equation 4.2 are evaluated at $\phi = \frac{\pi}{2}$ with $\phi = 0$ we find

$$E_{hor}\big|_{\phi=0} = -E_{vert}\big|_{\phi=\frac{\pi}{2}} \tag{4.4}$$

$$E_{vert}\big|_{\phi=0} = E_{hor}\big|_{\phi=\frac{\pi}{2}} \tag{4.5}$$

which can be seen in Figure 4.2, where the 3-D differential far-field patterns for the horizontal and vertical components radiated $Petal_1$ and $Petal_4$ shown in Figure 4.2c and Figure

4.2d respectively, can be directly compared to the vertical and horizontal E-field components radiated from $Petal_2$ and $Petal_3$.

The differential mode behavior, as well as the petal and port geometry of the CTT antenna, is analogous to that of the LPLS antenna. Thus the conclusions that are derived in these sections also apply to LPLS antenna. We revisited the CTT antenna because the undesirable ellipticity in its radiation pattern proved useful in visually distinguishing between the horizontally and vertically polarized fields. The desirable absence of eccentricity of the LPLS antenna requires a polarized probe in the far-field to measure the polarization of the fields.

4.3 LPLS Simulated Far-field Patterns

Simulated far-field radiation patterns for the LPLS antenna are discussed in this section. All the figures in this section are captured from CST simulation results for the CAD model from which the physical prototype was built. We will revisit this section when comparing the physically measured radiation patterns to these simulated results.

Referring to the geometry in Figure 4.3 it can be seen that the main radiation lobe of the antenna is always directed along the the z-axis. Figures 4.3a, 4.3c and 4.3e show the x-axis going to the right and the y-axis going into the page, while Figures 4.3b, 4.3d and 4.3f show the x-axis coming out of the page and the x-axis going to the right.

Figure 4.3 shows the differential excitation of $Petal_2$ and $Petal_3$. It was found in Section 4.2.3 that the co-polar component of radiation from $Petal_2$ and $Petal_3$ is vertical and along the $\phi = 90$ degrees plane (y-z plane), and is therefore shown in Figures 4.3b, 4.3d and 4.3f. It follows that the H-plane (defined as orthogonal to the E-plane) is along the $\phi = 0$ degrees plane (x-z plane) for the excitation of $Petal_2$ and $Petal_3$ and is shown in Figures 4.3a, 4.3c and 4.3e.

For an excitation of $Petal_1$ and $Petal_4$ the E-plane is along the $\phi = 0$ degree plane (x-z plane) and the H-plane is along the $\phi = 90$ degree plane (y-z plane), due to their rotation

of $\phi = 90$ degrees relative to $Petal_2$ and $Petal_3$.

4.3.1 Three Dimensional Patterns

To most effectively illuminate a parabolic dish with an on-axis feed antenna (as initial SKA dishes are slated to be) it is desired that the E-plane beamwidth equal the H-plane beamwidth. Initial plans for the SKA dishes are slated as parabolic dish with an on-axis feed antenna, therefore these equal beamwidths are important SKA antenna feed design parameters. With the exception of Figures 4.3a and Figures 4.3b at 0.8 GHz, the simulated low frequency (Figure 4.3) and high frequency (Figure 4.4) 3-D patterns at both $\phi = 0$ and $\phi = 90$ degrees roughly qualify the frequency independent behavior of the far-field radiation patterns up to 8 GHz. Quantitative data from physical measurements will be analyzed in Chapter 5.

4.3.2 Co-pol and X-pol Patterns at $\phi = 45$ Degrees

One particular 2-D plane of interest in terms of the co-pol and x-pol fields is that along the $\phi = 45$ degrees plane. At this angle, many antennas with some rotational symmetry, such as a diagonal horn, exhibit high x-pol fields [18]. This high presence of x-pol field energy is radiated at a cost to the co-pol fields.

Some SKA science drivers are astronomical objects that radiate polarized fields of interest to astronomers. For this reason, it is important that the SKA telescope is sensitive to the polarization of the radio light is receives.

We can see from Figure 5.19 that on boresight, the ratio of the co-pol to the x-pol components, or the cross polarization level (XPL) is about 8 dB at 1 GHz, 15 dB at 4 GHz and 16 dB at 8GHz. Although the XPL becomes less sensitive in the side lobes, this radiation is beyond the angular extent of the dish and should not compromise the cross-polarization discrimination of the radio telescope.

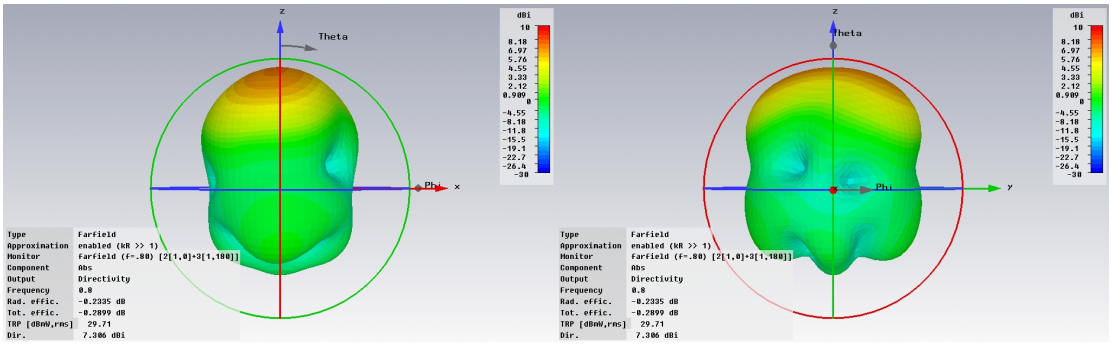

(a) 0.8 GHz at $\phi = 0$

(b) 0.8 GHz at $\phi = 90$

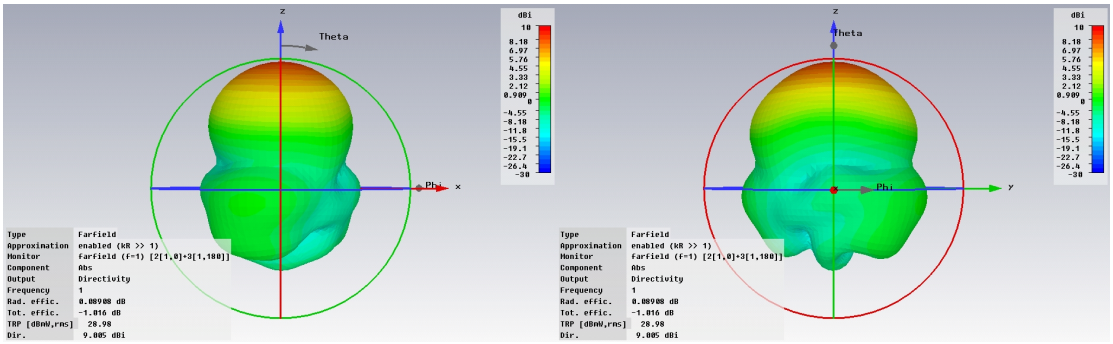

(c) 1 GHz at $\phi = 0$

(d) 1 GHz at $\phi = 90$

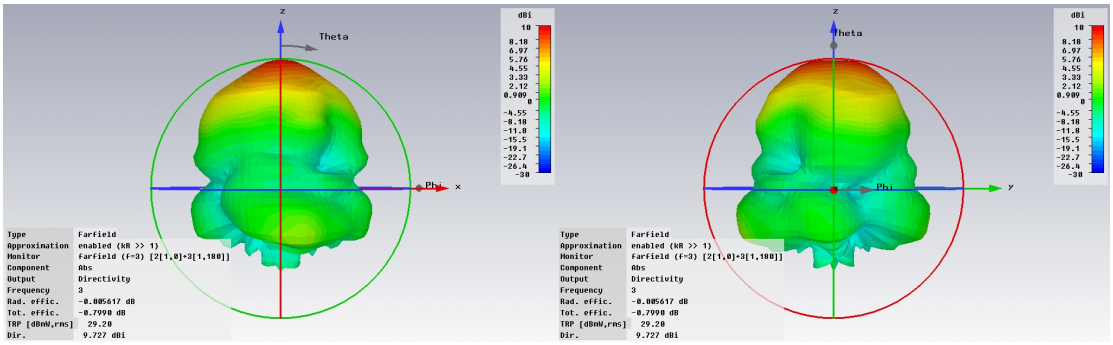

(e) 3 GHz at $\phi = 0$

(f) 3 GHz at $\phi = 90$

Figure 4.3: Simulated low frequency far-field 3-D patterns for the LPLS.

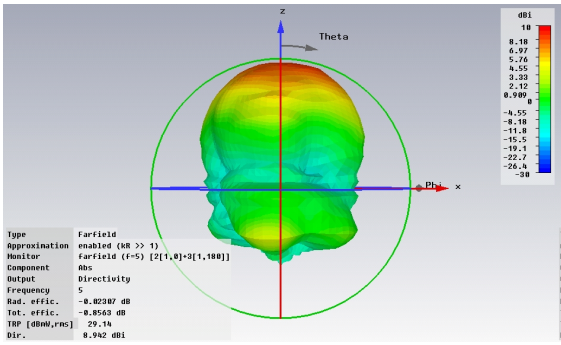

(a) 5 GHz at $\phi = 0$

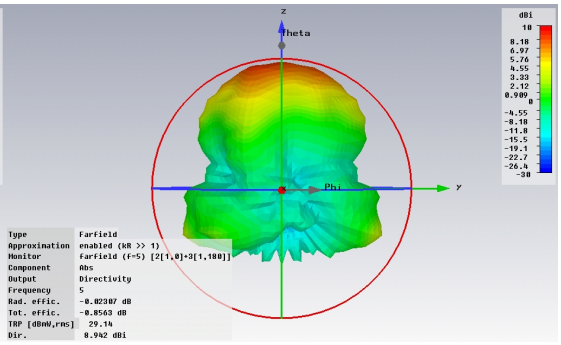

(b) 5 GHz at $\phi = 90$

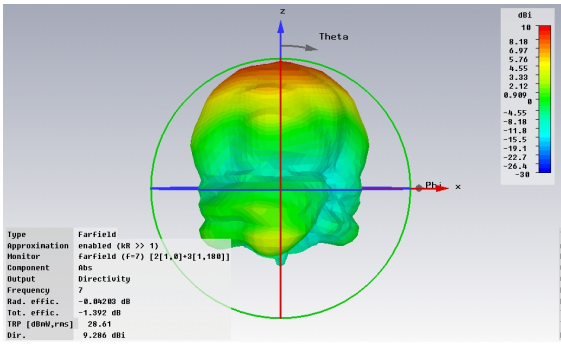

(c) 7 GHz at $\phi = 0$

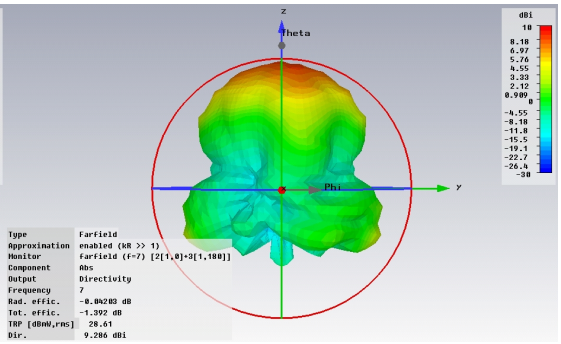

(d) 7 GHz at $\phi = 90$

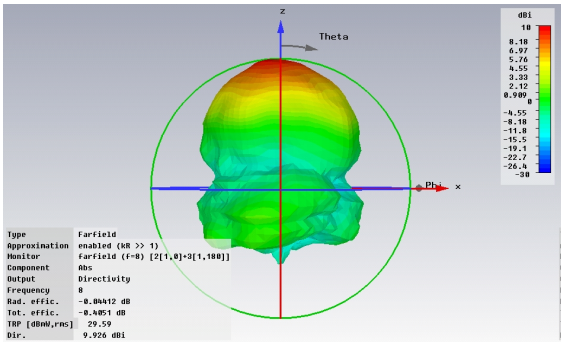

(e) 8 GHz at $\phi = 0$

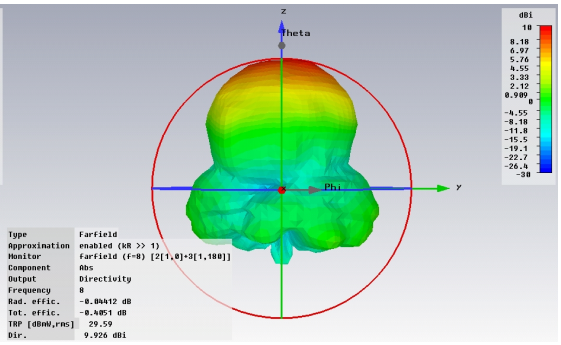

(f) 8 GHz at $\phi = 90$

Figure 4.4: Simulated high frequency far-field 3-D patterns for the LPLS.

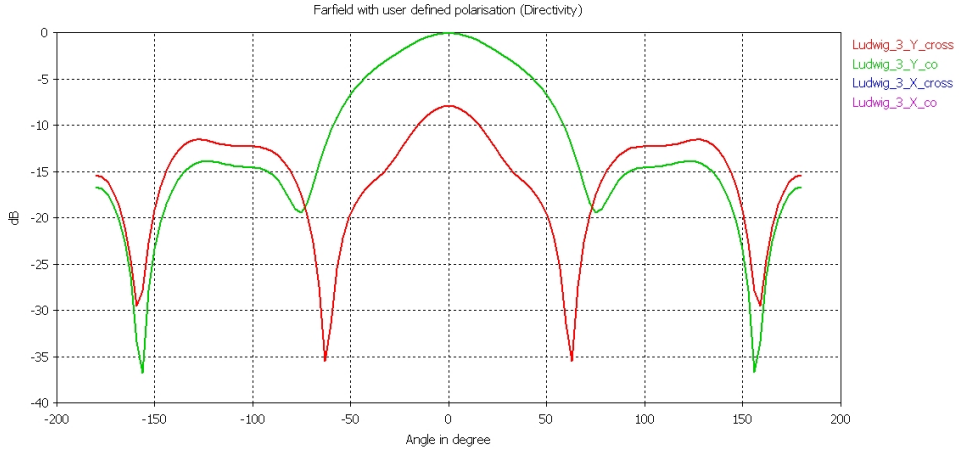

(a) 1 GHz

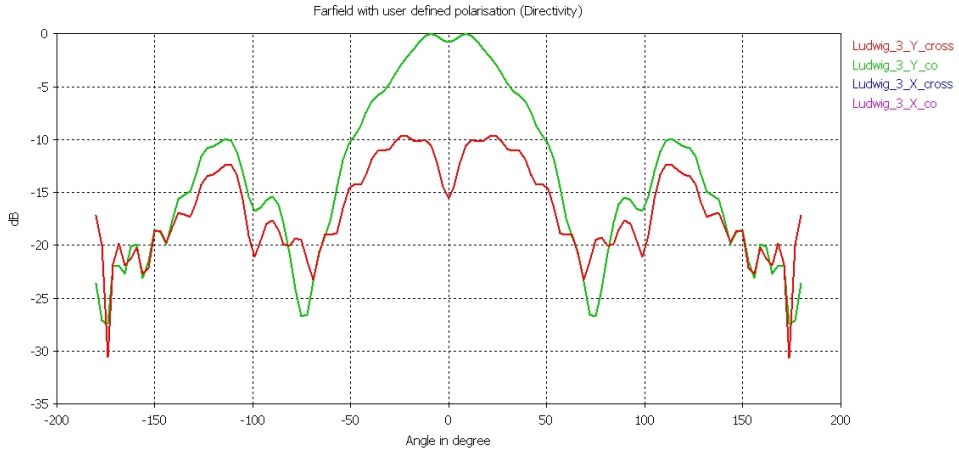

(b) 4 GHz

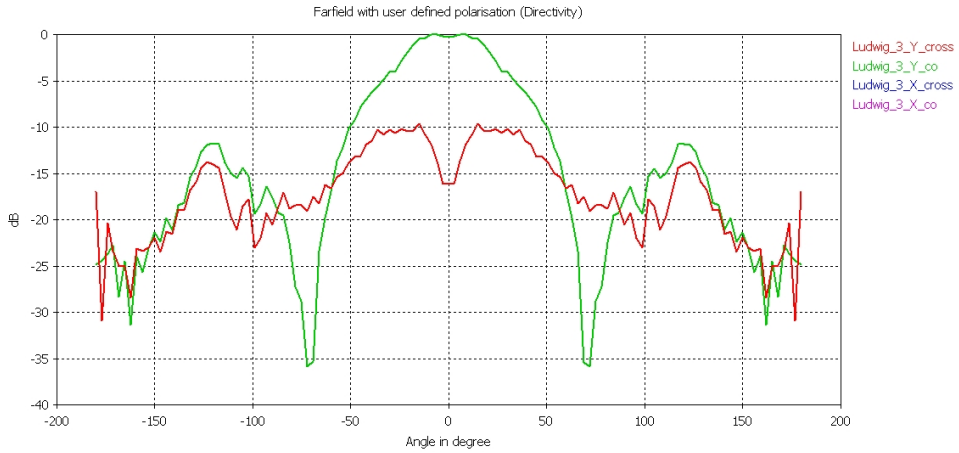

(c) 8 GHz

Figure 4.5: Simulated co-pol (green line) and x-pol (red line) 2-D patterns at $\phi = 45$ degrees.

4.4 Scattering Parameter Measurements

4.4.1 Feedpoint Impedance

Transmission lines such as coaxial cables are designed to have distributed reactive (and resistive) properties, such that the cables present a constant impedance across the frequency of operation. Specifically, the positive inductive reactance due to a length of conductor is matched with a negative capacitive reactance due to the proximity of two conductors, which combined result in a purely real impedance that can be matched across a wideband to devices attached to the transmission line. The presence of an unmatched reactive component in a transmission line introduces a frequency dependent impedance, and therefore limits the range of devices that can be perfectly power matched to the cable for optimal power delivery.

More complex antenna geometries present an increased difficulty in characterizing the impedance of an antenna. The idealized impedance of the SC structure described in Section 2.3 is not maintained due to the introduction of the conical ground "plane" surface. As an alternative to an extremely complicated geometrical analysis of the structure, simple measurements of the currents and voltages present at the feedpoint of the antenna can be used to characterize the single-ended impedance of the antenna.

The reflection coefficient (Γ) provides useful insight into the value of the antenna's unknown feedpoint impedance in relation to the known impedance of the transmission line feeding the antenna. The reflection coefficient is the measurement of the impedance discontinuity at the interface of two components, in this case defined as the ratio of the backward directed "reverse" voltage V^- reflected from the antenna divided by the forward voltage V^+ supplied to the antenna . In terms of S-parameters as well as voltage

$$\Gamma = s_{11} = \frac{V^-}{V^+} \tag{4.6}$$

4.4.2 Characterizing the Impedance in Simulation

The antenna presents some complex impedance (Z_a) to the transmission lines feeding the antenna. We can consider the feedpoint as the interface where the inner-most portion of the petals interfaces with the structure that delivers power from the generator to the antenna. In the physical VNA measurement obtained in Chapter 5, the VNA delivers the power to the four petals via the four single-ended, coaxial cables.

A similar measurement can be simulated on CST by computer modeling the four coaxial cables. Each cable can then be excited with a "waveguide port", which is defined in CST as an "infinitely long waveguide connected to the structure"[25]. The waveguide port is excited with a square root of one watt of peak power that propagates along the coaxial cable toward the antenna feedpoint and additionally travels forever away from the structure down the infinitely long waveguide.

An eigenmode solver determines the number of modes that can be supported at the 2-D front "face" of the waveguide. The coaxial cables can be modeled to have an intrinsic line impedance that most closely matches the presumed real part of the antenna's feedpoint impedance $\Re\{Z_a\}$ by appropriately adjusting the ratio of the diameter of the inner conductor to that of the outer conductor. A further adjustment of the transmission line's impedance can only be accomplished by a subsequent simulation, as the fields set up in the waveguide port are based on the geometry of the port, and cannot be "renormalized" to a different value.

Simulating the excitation of the antenna directly with coaxial cables may be the most genuine representation of physical measurement procedure, but this method may present problems as well. Specifically, port measurements that are recorded at the waveguide port of the coaxial may obscure the actual data that is present directly at the feedpoint of the antenna. Before being able to qualify the accuracy of a simulation measurement collected at the far end of the coax, it must be understood what results are expected at the feedpoint of the antenna. The Smith chart is one tool for visualizing such measurement results and would qualify the need to mathematically "de-embed" the transmission line from the data.

4.4.3 Smith Chart in Simulation

A plot of a circle centered on the Smith chart generally represents a reflection coefficient with constant magnitude and varying phase, such as $|\Gamma_a|e^{j\theta}$ at a single frequency. Such a curve is usually encountered when measuring a standing wave pattern at varying positions of z on a piece of transmission line where $j\theta$ can be simplified as $j\beta z$. Alternatively, this same curve could be explained as the result of measuring a current distribution similar to a standing wave pattern, but instead measured at a single location of z and for varying values of β. Such a measurement is taken when plotting the reflection coefficient across the frequency band in a broadband feed. As a better match between the transmission line and the antenna is approached, it would be expected that this circle's radius would reduce. Only an antenna that is perfectly resonant across the entire bandwidth could produce a curve that reduces to a point centered on the normalized Smith chart.

All known frequency independent structures exhibit a reactive impedance at various frequencies across the band, and thus an ideal static point on the Smith chart will not be encountered for broadband measurements. Further deviations from a constant radius curve on the Smith chart can be expected for log periodic structures as the magnitude of the reflection coefficient will likely vary for the range of frequencies near resonance in a single cell as discussed in Section 2.2.2. Furthermore, these deviations will not be consistent with the period of a complete rotation around the Smith chart, which varies linearly with frequency as opposed to varying with the logarithm of the frequency.

4.5 ADS Transmission-line Model

Figure 4.6 shows ADS simulations in which a hypothetical impedance mis-match between the antenna and the transmission line is superimposed on various lengths of transmission line prior to measurement. We could consider these initial plots of Figure 4.6a as three different feedpoint reflection coefficients that the antenna may present to the transmission line. The superposition of the initial plots upon the transmission lines of increasing length

eventually results in the Smith Chart plot of Figure 4.6c that provides little intuition about the antennas actual feedpoint s-parameters.

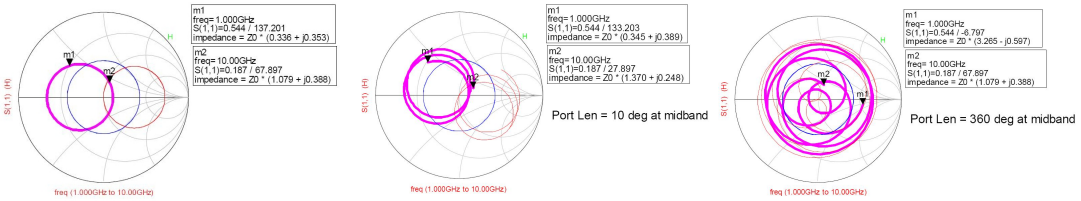

(a) Feedpoint plots (b) Short transmission lines (c) Long transmission lines

Figure 4.6: ADS simulation of (a) initial data measured through (b) and (c) coax of increasing length, "Port Len".

The results of Figure 4.6a can be extracted from the plot in Figure 4.6c with a process called "de-embedding" that will be discussed in Section 5.6.3.

4.6 LPLS Simulated S-Parameter Measurements

This section presents the simulated far-field radiation patterns for the LPLS antenna, and all the figures in this section are from CST simulation results for the CAD model from which the physical prototype was built. We will employ the convention that lowercase S-parameters (such as s_{11}) are the linear measurement while uppercase S-parameters (such as S_{11}) are given in dB.

4.6.1 LPLS Simulated Single-ended Results

Direct measurements taken at a single port are referred to as "single-ended" measurements. Although we are ultimately interested in the differential S-parameters, the single-ended measurements provide an intuition into the operation of the antenna. Furthermore, the differential measurement data will be mathematically derived from single-ended measurements in both simulation and VNA data, because measuring equipment such as VNAs are themselves single-ended devices.

Figure 4.7a shows the reflection coefficient $\Gamma = s_{33}$ plotted on the Smith Chart with the 8 mm of feeder coax cable de-embedded from the data. Efforts were made to keep the coax cable as short as the simulation software permits, however a minimum length of transmission line is required to properly set-up the TEM propagating wave. Figure 4.7b is a plot of the single-ended S_{22} measurements. Note in this ideally reciprocal device, $s_{22} = s_{33}$ for the excitation of $Petal_2$ and $Petal_3$. Additionally, $s_{11} = s_{44} = s_{22} = s_{33}$ for the excitation of $Petal_1$ and $Petal_4$ as compared to the same excitation of $Petal_2$ and $Petal_3$. We will reserve discussion about the magnitude of these values until later, and at this time note that this graph was plotted on a logarithm scale so that the periodicity of the S_{22} as a function of logarithm of the frequency is apparent.

4.6.2 LPLS Simulated Differential Results

Although single-ended ports are required for measuring purposes, in practice the differential currents described in Section 3.3.1 would ideally drive a differential amplifier. For highly sensitive applications, such as radio astronomy, this differential amp should be a low-noise amplifier (LNA). There are currently efforts underway to design differential LNA's specifically for the WB+SPF SKA feeds [27]. Collaborations with Caltech's Dr. Weinreb to develop differential LNA's specific to a given antenna's differential impedance are presently underway for the QSC feed [10] and the Eleven feed [22], as well as the presently implemented LNA's in the ATA Hat Creek Observatory [13]. If the feed presented here is further developed, it is proposed that such a collaboration may be considered to match the differential impedance of the LPLS to a differential LNA. For these reason, efforts are not made to standardize the impedance of the feed to a single-ended 50 ohm load.

The "mixed mode" S-parameters of a differential 2-port device can be derived from 4-port single-ended measurements [28]. The term "mixed mode" refers to the mode conversion that may take place between common and differential mode currents. The subscripts in a mixed mode S-parameter matrix generally indicate the mode conversion on the left and

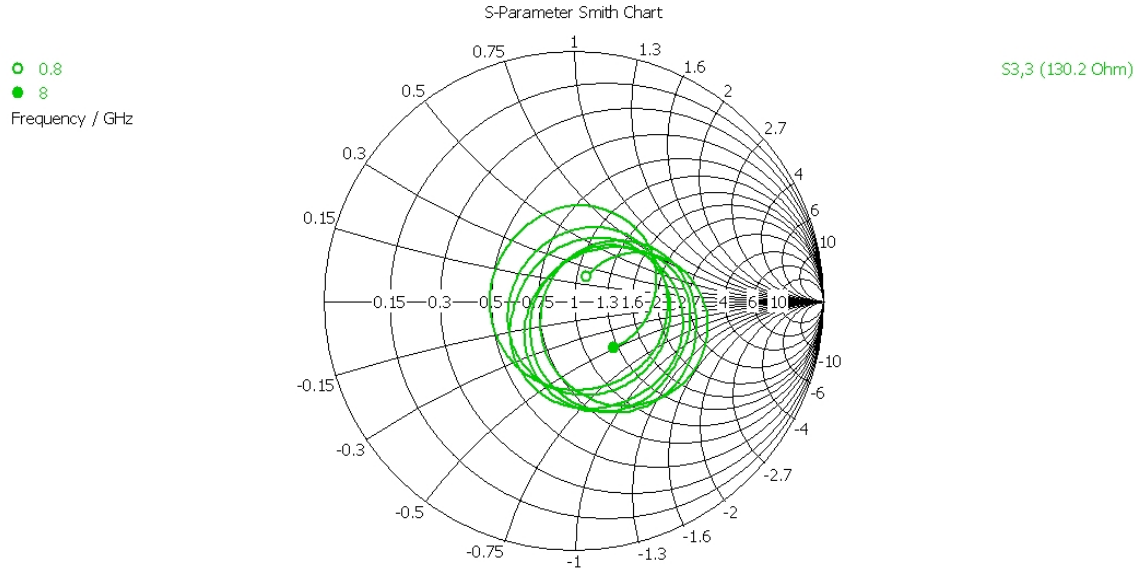

(a) Reflection coefficient, $\Gamma = s_{33}$ plotted on the Smith Chart.

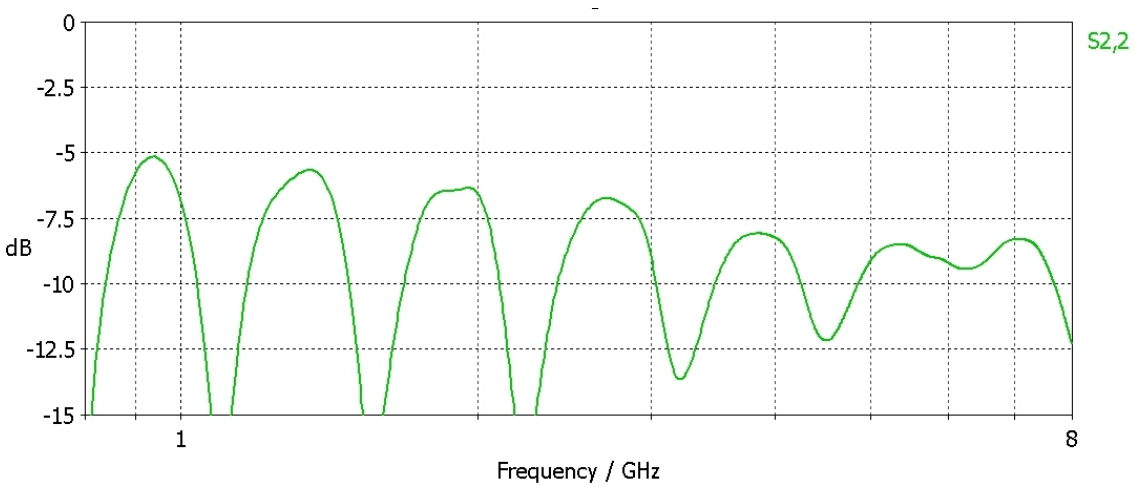

(b) Single-ended S_{22} measurements

Figure 4.7: Single-ended reflection coefficient data from the excitation of $Petal_2$ and $Petal_3$ plotted in dB.

port conversion on the right.

$$S_{ghij} = S_{(output-mode)(input-mode)(output-port)(input-port)} \tag{4.7}$$

such that s_{dd11} would be currents reflected out from port 1 in differential mode normalized by those driven into port 1 in differential mode [29].

In a device in which there has been zero mode conversion that is differentially fed between single-ended ports 1 and 4, the differential s_{11} is calculated as

$$s_{dd11} = \frac{1}{2}\big(s_{11} + s_{44} - s_{41} - s_{14}\big) \tag{4.8}$$

or in a reciprocal device

$$s_{dd11} = s_{11} - s_{41} \tag{4.9}$$

for the linear S-parameter values. When s_{dd11} is given in dB as a positive value, it is often referred to as the differential return loss. Equation 4.8 and Equation 4.9 have been employed by both the QSC feed [30] and the Eleven feed [31] respectively, to characterize the differential return loss of their antennas. Figure 4.8 shows the results for the LPLS antenna from an excitation of $Petal_2$ and $Petal_3$, therefore the magnitude of the differential return loss S_{dd22} is calculated from $s_{dd22} = s_{22} - s_{32}$.

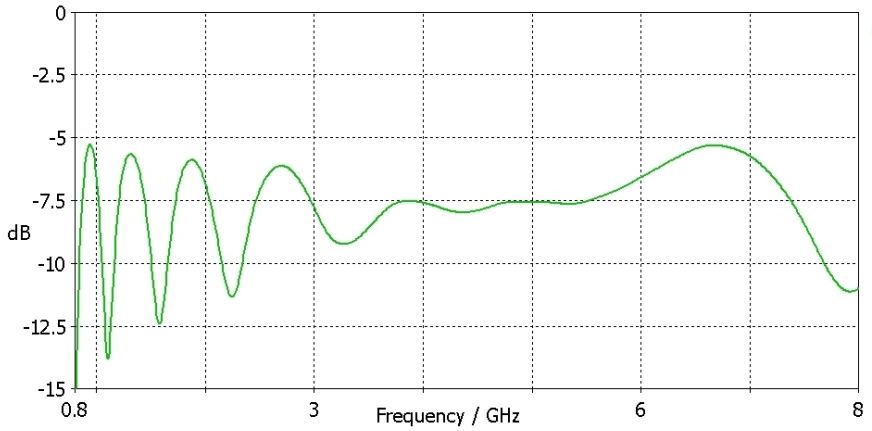

Figure 4.8: Simulated S_{dd22} in dB vs frequency in GHz.

Although the results of Figure 4.8 show a disappointingly high level of reflected power at the feed, we also note that initial publications of the Eleven feed reported a simulated differential return loss that was also no better than 5 dB [22]. Recent efforts have been successful at reducing the S_{dd11} for the Eleven feed [32] and we anticipate the efforts would find similar success for the LPLS feed.

Chapter 5

Antenna Measurements

In this chapter we will define the geometry of the prototype that was researched and constructed at the NRC's Herzberg Institute for Astrophysics (HIA) in Victoria, British Columbia. The standards that we employed when obtaining and interpreting the antenna measurements conducted at the NRC-HIA's DRAO in Penticton, British Columbia will also be introduced in the Chapter. Finally, we will also display and evaluate these results by providing comparisons to simulated results and other WB+SPF results.

5.1 Built Prototype

A draft of the constructed LPLS prototype modeled by P. Czajko, a mechanical engineering co-operative student at HIA in Victoria, is shown in Figure 5.1, with the components labeled as follows [33]:

- 1) High conductivity aluminum (Al 1100) conical surface with a bottom diameter of 450 mm and height of 225 mm minus a truncated tip of 18 mm.
- 2) High conductivity aluminum (Al 1100) solid cone tip with a bottom diameter of 36 mm and a height of 18 mm minus 3 mm for foam spacer.
- 3) Lowloss Eccostock foam support.

- 4) Co-axial cable with outer diameter of 2.2 mm and 73 mm in length (not to scale in drawing).
- 7) Male SMA connector.
- 8) Standard grade aluminum wedge interface to connect cone to baseplate.
- 9) Standard grade aluminum baseplate for mounting onto measurement positioner.
- 11) Teflon clamp and Teflon screws for securing and properly positioning petals.
- 12) High conductivity aluminum (Al 1100) petals, manufactured by water jet cutting process.

These dimensions above in conjunction with the variable values provided at the end of Chapter 3 and repeated below for convenience, completely define the built prototype.

- the conical ground surface was fixed at 45 degrees.
- the number of petals i was set to 4 in order to achieve two linear polarizations, each composed of two petals.
- the inner-most radial distance of the petal $\rho_{max} = 3$ mm.
- the outer-most radial distance of the petal $\rho_0 = 225$ mm.
- the rate of exponential growth of the spiral $c = -0.34$.
- the arm angle of the zig zags, $\alpha = 66$ degrees.

Figure 5.2 shows a close-up of the Al 1100 solid cone tip, truncated 3 mm below its apex, detailing the four holes drilled in its interior through which the 2.2 mm diameter co-axial cable is extended. The outer conductor of the co-axial cable is then cut flush with truncated tip of the solid cone and the inner conductors are extended through the low-loss foam an additional 6 mm to make a convenient contact with the top of the petals. Figure 5.2 also details the Teflon hardware that affixes the petals to the foam support, which separates the petals from the cone a distance of 3 mm.

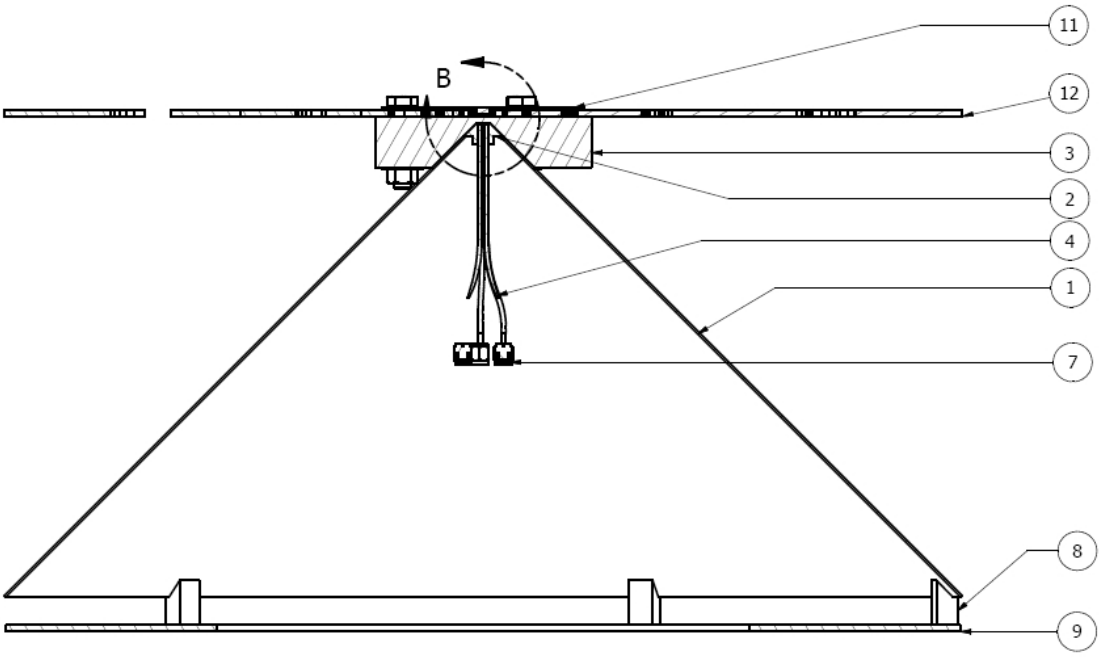

Figure 5.1: Draft of the built LPLS with ground surface prototype by P. Czajko.

5.2 Antenna Geometry in Measurement

For consistency with the simulated set-up, the four petals of the antenna are mounted such that when differentially fed, $Petal_1$ and $Petal_4$ radiate predominately horizontally polarized E-fields, and so are referred to as the horizontal petals, while $Petal_2$ and $Petal_3$ radiate vertically and are referred to as the vertical petals. Each of the four petals are individually attached to an exposed co-axial inner conductor 6 mm in length. Figure 5.3 shows photographs of the cone tip before and after the attachment of the petals to the cables. The shields of the four co-axial cables are grounded to the conical reflector 3 mm beneath the underside of the petals. These four single-ended co-axial cables then extend 73 mm into the interior of the cone and are terminated with SMA connectors.

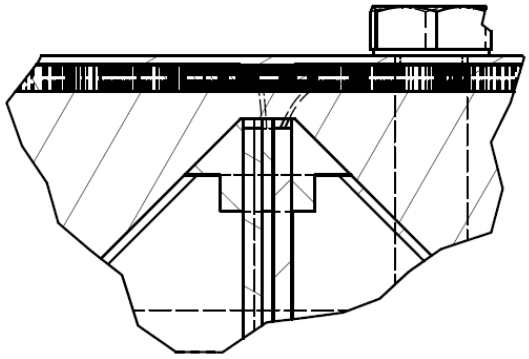

Figure 5.2: Draft of the prototype's feeding region by P. Czajko.

5.3 Field Regions

As the distance from an antenna changes, the nature of the electromagnetic fields surrounding the antenna change as well. In order to interpret a measured field pattern, one must confirm that the measurement probe is located in the expected region around the AUT. The fields very near an antenna are a combination of reactive and radiating fields. As the measurement probe recedes from the antenna, the reactive fields dissipate and the radiating fields undergo a spatial FT [34] as will be detailed further in the following sections.

5.3.1 Far-Field

The far-field region is described as a distance at which the relative pattern is not effected by a variations in the radial distance from the AUT, which is placed at the origin of a spherical coordinate system. This distance r_{ff} is generally accepted as $r_{ff} > \frac{2D^2}{\lambda}$ where D is the largest dimension of the antenna's aperture [35]. At this distance of r_{ff}, the radiated far-field wavefront emitted from an isotropic radiator would present a maximum phase variation of $\frac{\pi}{8}$ [36]. In the far-field region, the amplitude of the E-field component will decay as $\frac{1}{r}$, however as stated above, the pattern will not otherwise vary as a function of r.

(a) Exposed co-axial inner conductors

(b) Conductive epoxy drying with temporary dowel separator.

Figure 5.3: Cone tip (a) before and (b) after the attachment of the petals to the cables.

5.3.2 Near-Field

Interior to the far-field boundary is a region described as the near-field $r_{nf} < \frac{2D^2}{\lambda}$. Within the near-field, there are two regions of further distinction described as the radiating near-field and the reactive near-field.

Reactive Near-Field

At radial distances smaller than $r = \sqrt{\frac{2}{3\sqrt{3}}(\frac{D^3}{\lambda})}$ or $0 < r_{nf_i} < 0.62\sqrt{\frac{D^3}{\lambda}}$, the E and H complex vector fields are predominately out of phase with one another. Therefore, the complex Poynting vector ($S = E \times H$) is largely imaginary. In the reactive near-field, the amplitude of the reactive E-field component decays at a rate faster than $\frac{1}{r}$ and its relative field strength will additionally vary as a function of r [21].

Radiating Near-Field

As r is increased, the reactive components decay sufficiently such that real or radiating components of the Poynting vector begin to denominate. This region is usually defined by the boundaries of $0.62\sqrt{\frac{D^3}{\lambda}} < r_{nf_r} < \frac{2D^2}{\lambda}$. Unlike the far-field radiating region, in the radiating near-field the pattern is a function of r [18]. Therefore, in this region the E-field decays as $\frac{1}{r}$, similar to the far-field, while the angular distribution of the field does vary with distance from the antenna, similar to the reactive near-field.

5.4 Radiation Pattern Measurements

The radiation pattern is a graphical depiction of the relative variation of the fields as a function of angle about the AUT at a fixed distance r_0. Due to the remote nature of most communications or radio astronomy applications, the far-field radiation pattern is often the most useful graphical representation of the field.

Far-field pattern measurements can be accomplished by measuring E_θ and E_ϕ along constant θ or ϕ circles of a spherical coordinate system. If phase coherent measurements

are achieved, the polarization of the E-field can be determined by taking the phase angle δ between the complex E_θ and E_ϕ components [8]. The E-field radiating from the AUT can be measured by a probe antenna moving along a spherical coordinate system in the AUT's far-field, or by rotating the AUT along its ϕ and θ while the probe remains still, or finally, by some combination of movement by both the AUT and the probe. Due to reciprocity, the radiation pattern of the AUT can be determined by illuminating the AUT with a plane wave emanating from a far-field source [21].

The far-field radiation pattern can be directly sampled in the far-field region, or it can be sampled in the near-field region and transformed into a far-field pattern by the FT [18]. We elected to directly measure the radiation pattern in the far-field.

5.4.1 Positioner System

The AUT and/or the probe antenna is placed on positioning equipment that guide the antennas along the constant ϕ and θ circles. One of the common positioner arrangements, referred to as "Roll over Azimuth", is shown in Figure 5.4. DRAO's anechoic chamber is configured with a roll over azimuth range that permits a full 360 degree rotation of θ and ϕ, and has the elevation of the AUT fixed at 90 degrees.

With the elevation angle fixed along the z-axis, the z-axis is referred to as the "pole" of the system, with all constant ϕ circles moving through the pole while all constant θ circles move around the pole [37], as shown in Figure 5.5.

Note that in textbooks the spherical coordinate system is often depicted with the z-axis pointed vertically, and thus the θ angle is often referred to as the elevation angle, and the angle ϕ is referred to as the azimuth angle. However, in many measurement systems it is more useful to point the z-axis horizontally, directly facing a similarly situated probe [34]. In this scenario, the term "elevation" retains its definition as the altitude, or angle upward, of the AUT relative to the vertical plane at 0 and 180 degrees. Thus, in this case the elevation angle is no longer synonymous with θ. Additionally, in this positioner arrangement, the term "azimuth" is not used to describe any variation in angle of the positioner, however,

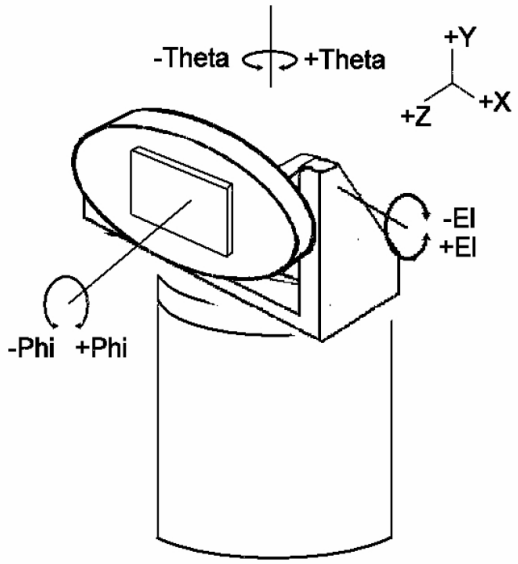

Figure 5.4: A roll over azimuth positioner with the elevation of the AUT shown at 90 degrees [37].

the title "roll over azimuth" likely refers to the fact that the AUT rolls or spins along an axis in the horizontal plane.

The probe in DRAO's measurement range was fixed; however, it could also roll along its axis through all 360 degrees with an angle referred to as χ. Figure 5.6 is a schematic for a range geometry consistent with that of DRAO's range, with the probe positioned at some (θ, ϕ) angle, and then rolled on its axis to some angle χ [34]. In this representation, the probe appears to be moving along a "measurement sphere" at some radius r with the antenna remaining static. In fact at DRAO, the antenna's movements will be contained within a region termed the "test antenna minimum sphere" while the probe remains static, with the exception of rolling along it's own axis (the z-axis) to any angle χ.

5.4.2 Ludwig's Third Definition

Ludwig's third definition of polarization is particularly effective in measuring linearly polarized antennas. In this definition, the main polarization of the measurement antenna probe and the AUT are initially aligned, and the angle of the probe and AUT remains aligned as the antennas are adjusted in synchronization throughout the measurement cycle. In

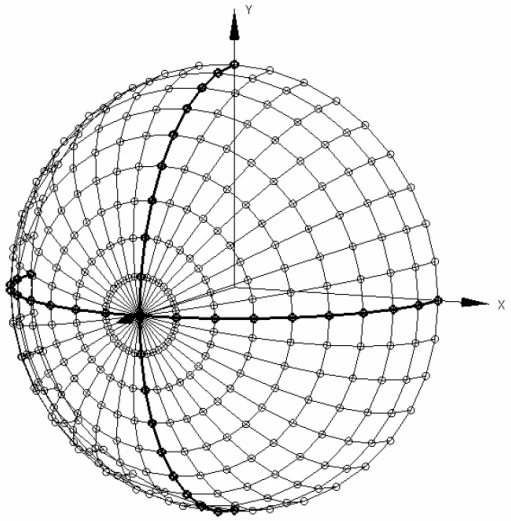

Figure 5.5: Rotation angles for a roll over azimuth positioner with the z-axis angling out of the page.[37]

addition to direct measurement, this type of alignment can also be obtained after a phase coherent-measurement through transformations [26]. We elected to directly measure the AUT using Ludwig 3 in the far-field, as detailed below.

5.4.3 Ludwig 3 in Measurement

1. Prior to the first measurement cut at $\phi_0 = 0$, a linearly polarized probe at the boresight location of $\theta = 0$ will be aligned parallel to the polarization of the AUT to an angle now defined as $\chi_0 = 0$ for the remaining measurements. This alignment results in the probe receiving a maximum induced voltage for its distance r_{ff} from the AUT.

2. A 2-D cut of the AUT's radiation pattern will then be accomplished by moving the probe or the AUT, such that the probe swings through the range of values from $-\theta_{max}$ to θ_{max} with an increment of $\Delta\theta$.

3. The AUT rolls on its axis to $\phi_1 = \phi_0 + \Delta\phi$, to permit measurement cuts for varying values of ϕ.

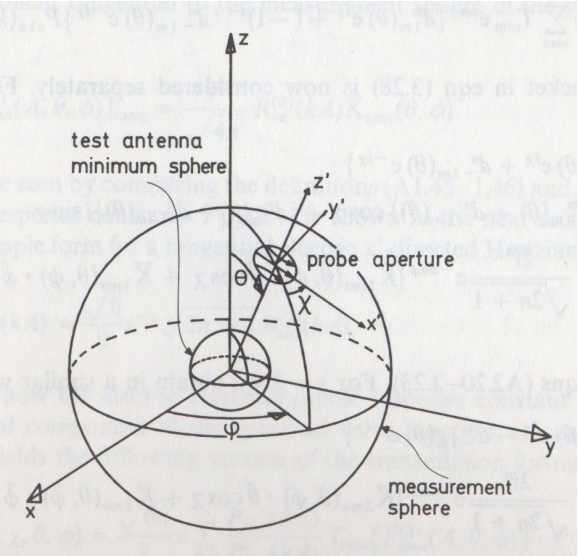

Figure 5.6: A schematic for a range geometry consistent with that of DRAO's range, with the probe positioned at some (θ, ϕ) angle, and then rolled on its axis to some angle χ [34].

4. The probe is also rolled to a value of $\chi_1 = \phi_1$ to maintain an ideal alignment with polarization of the AUT.

Steps 2 through 4 continue for the range of values from $-\phi_{max}$ to ϕ_{max}. This measurement of the co-pol of the AUT will be followed by a measurement of the orthogonal x-pol. The x-pol measurement is accomplished by iterating through the above measurement cycle; however, in Step 1, the initial value for χ is $\chi_0 = 0 + 90$ such that throughout the measurement cycle $\chi_n = \phi_n + 90$ degrees.

5.4.4 Ludwig 3 in Post-processing

Figure 5.7 shows the polarization of a horizontal probe superimposed on the measurement sphere of the AUT with the z-axis angling out of the page in Figure 5.7a and the z-axis angling into the page in Figure 5.7b. These curves are also referred to as the Ludwig 3 horizontal cicles. Figure 5.7c shows the Ludwig 3 vertical circles. Note that although the circles depicted in Figures 5.7 are not along the spherical coordinate system, they can in fact be obtained from measurements along spherical coordinates.

The apparent discrepancy between the circles depicted in Figure 5.5 and Figure 5.7 is

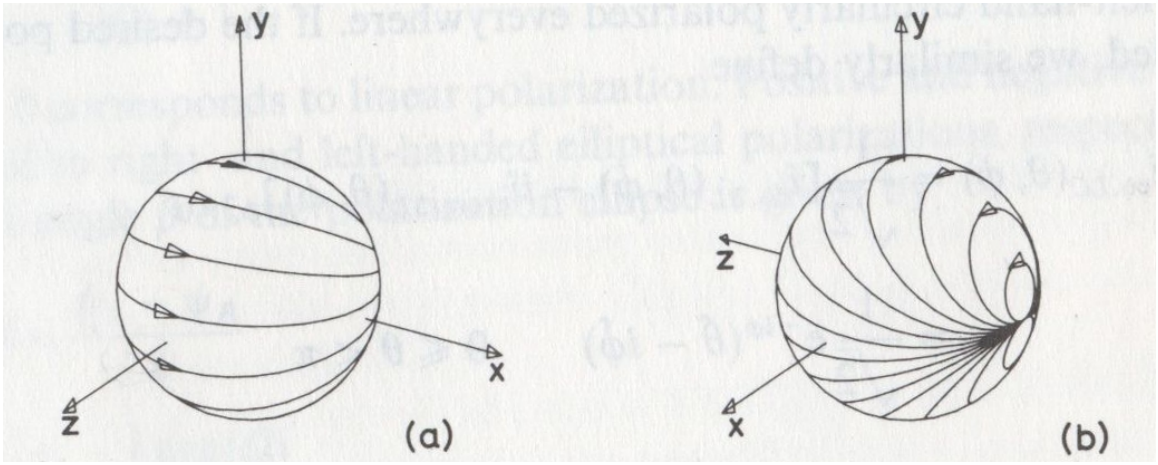

Figure 5.7: Horizontally polarized fields defined by Ludwig's third definition with (a) the z-axis angling out of the page and (b) the z-axis angling into the page [34].

resolved with the recognition that Ludwig's third definition circles do not describe individual 2-D measurement cuts. Instead, a Ludwig 3 circle is strung together from multiple, nearby individual $E(\theta_0, \phi_0)$ measurements originating from distinct 2-D constant θ_0 and constant ϕ_0 slices. The specific individual measurements that comprise a Ludwig 3 circle are those that permit the probe's orientation to remain approximately horizontal, or, as is the case in Figure 5.8, the probe remains approximately vertical.

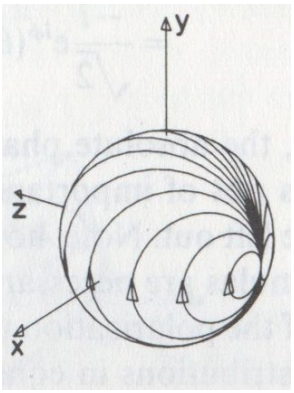

Figure 5.8: Vertically polarized fields defined by Ludwig's third definition [34].

5.4.5 Vertical and Horizontal Measurements

As discussed in Section 4.2, $Petal_1$ and $Petal_4$ together produce a co-pol main beam that is horizontal, while $Petal_2$ and $Petal_3$ together produce co-pol main beam that is vertical. Another schematic of DRAO's roll over azimuth range is shown in Figure 5.9 with the cartesian coordinates of the AUT the vertical (v) and horizontal (h) polarization of the probe at some arbitrary location [38].

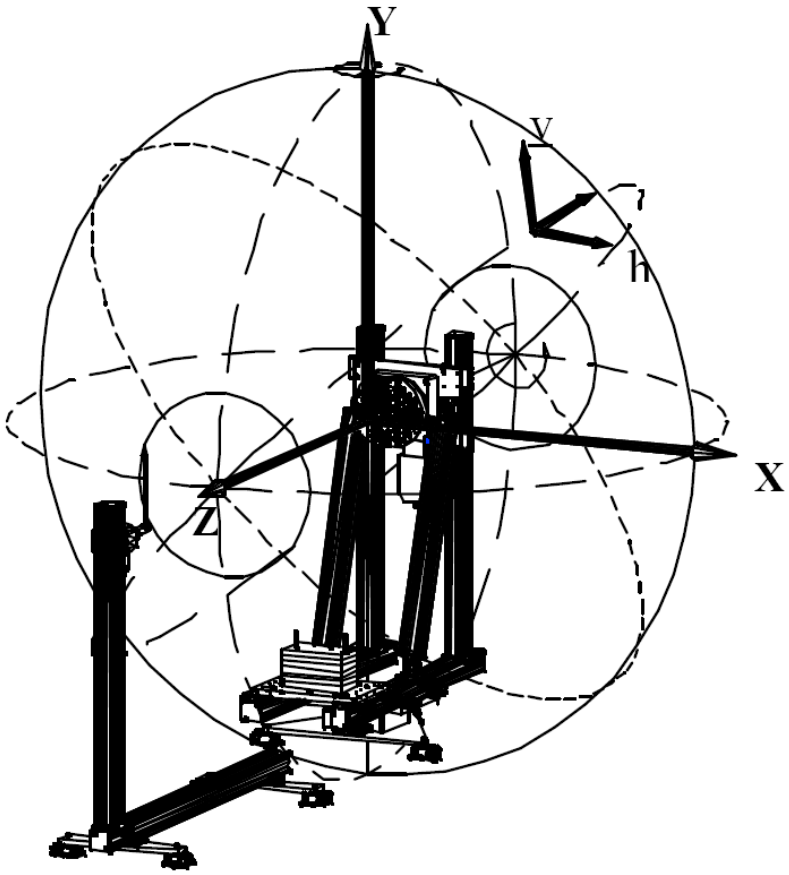

Figure 5.9: Vertical and horizontal orientation of the probe at some arbitrary location indicated in the cartesian coordinates of the AUT [38].

The vertically polarized probe measures the co-pol radiated fields from $Petal_2$ and $Petal_3$, and it measures the x-pol fields from $Petal_1$ and $Petal_4$. Conversely, the vertically polarized probe measures the x-pol radiated fields from $Petal_2$ and $Petal_3$, and it measures the co-pol fields from $Petal_1$ and $Petal_4$.

5.5 LPLS Differential Far-field Measurements

To obtain a differential excitation between the two petals comprising a single polarization, the two petals must be excited with identical signals, barring the distinction that they are 180 degrees out of phase with one another.

5.5.1 180 degree hybrid

This requirement of evenly splitting a signal between the petals, while providing a 180 degree phase difference, can be met with the insertion of a 180 degree hybrid between the VNA and the two petals of interest. Although this task requires only one input port and two output ports, a 180 degree hybrid is in fact a four port device with the extra port terminated in the characteristic impedance of the port [39]. For our purposes, we desire a device where the signal incident at port 1 couples 3 dB of its power to port 2 and couples the remaining 3 dB to port 3 with no power coupled to the isolated (extra) port 4.

In practice a 180 degree hybrid is a frequency dependent device, such that in most cases it can provide an even split of the power at only two frequencies. The frequency response of this component can be determined by injecting a VNA-supplied signal into port 1 and measuring the response from port 2 while port 3 is appropriately terminated. After recording the measured signal from port 2, this procedure can be repeated to measure port 3. The frequencies at which the ratio of the power split between ports 2 and 3 is equal to one, can be found by dividing the two independently measured signals. At the frequencies for which there is a 0 dB difference between ports 2 and 3, the phase difference would ideally be 180 degrees. Figure 5.10 shows the amplitude difference (top) and phase difference (bottom) between the signals coupled to port 2 and port 3, indicating that the 180 hybrid evenly couples power to ports 2 and 3 at frequencies 4.8 GHz (marker 3) and 7.7 GHz (marker 4) with phase differences of about 175 degrees at both frequencies. We expect to find the most accurate representation of the differential far-field patterns near these frequencies.

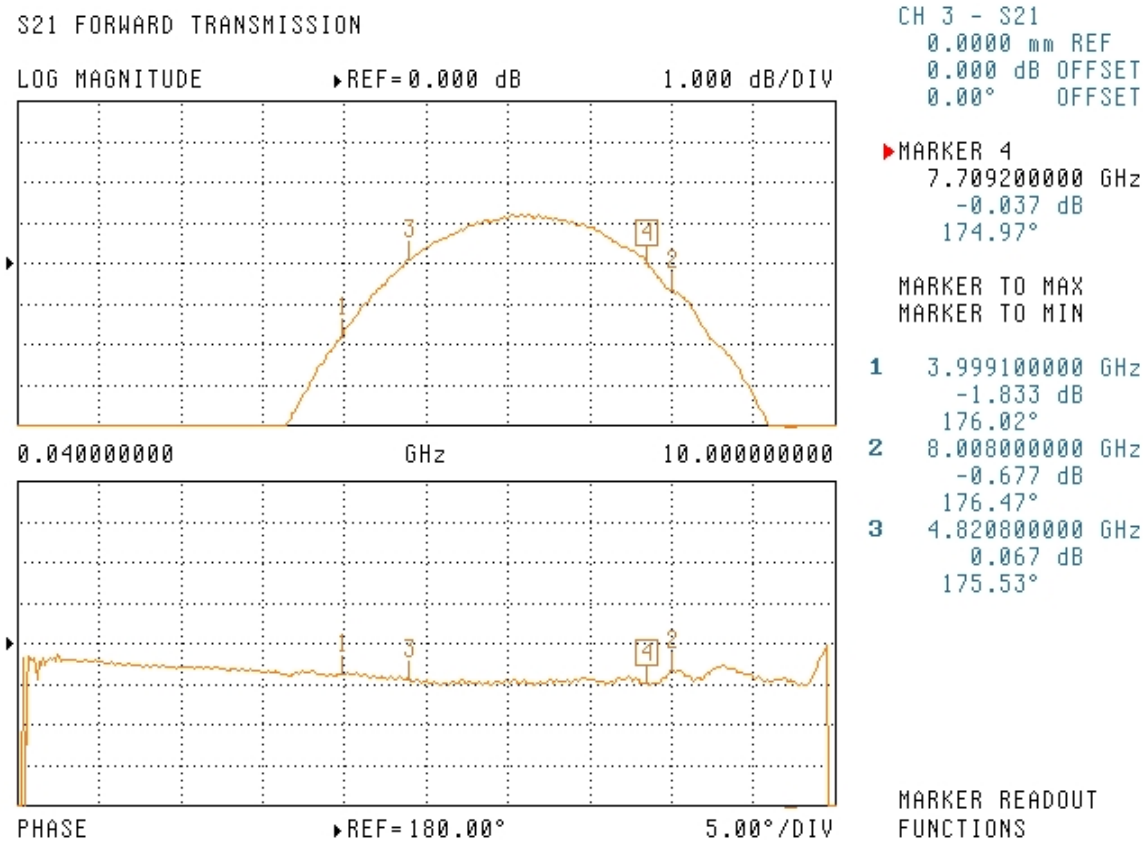

Figure 5.10: Amplitude (top) and phase (bottom) difference between the signals coupled to port 2 and port 3.

For the lower frequencies, we utilized a 180 hybrid that evenly split its power between port 2 and port 3 at the frequencies 1.22 GHz and 1.76 GHz. The phase differences between the signals at ports 2 and 3 at 1.22 GHz is about 170 degrees (marker 2) and at 1.76 GHz is about 160 degrees (marker 1), as shown in Figure 5.11.

5.5.2 Differential Hybrid Patterns

Four waveguide probe antennas where used to measure the AUT in the following bands:

- 0.95 GHz to 1.45 GHz
- 3.3 GHz to 4.9 GHz
- 4.9 GHz to 7.05 GHz

Figure 5.11: Phase difference between the signals coupled to port 2 and port 3.

- 7.05 GHz to 10 GHz

A rough image of the antenna's performance across the band can be seen in the far-field patterns of Figures 5.12 and 5.13. Across the four probes, and at times within each single probe, there is a great deal of variation in the gain that each probe measured, from about -35 dB maximum at the low frequencies to about -80 dB maximum at the highest frequencies. However, the directivity, or relative radiation patterns, are fairly consistent across the band, and will be further investigated later. The variations in maximum gain can be explained by the lack of a calibration antenna to determine the frequency dependency of the gain across the probe antennas. In an uncalibrated system, it can be expected that increases in frequency require probes with smaller aperture areas, and thus the received power density integrated over the aperture results in a lower total power.

Despite our inability to quantify the absolute gain of the antenna, we can use the data measured to analyze the directivity of the co-pol and x-pol E-field of the antenna at each frequency measured, as we will investigate in the following sections.

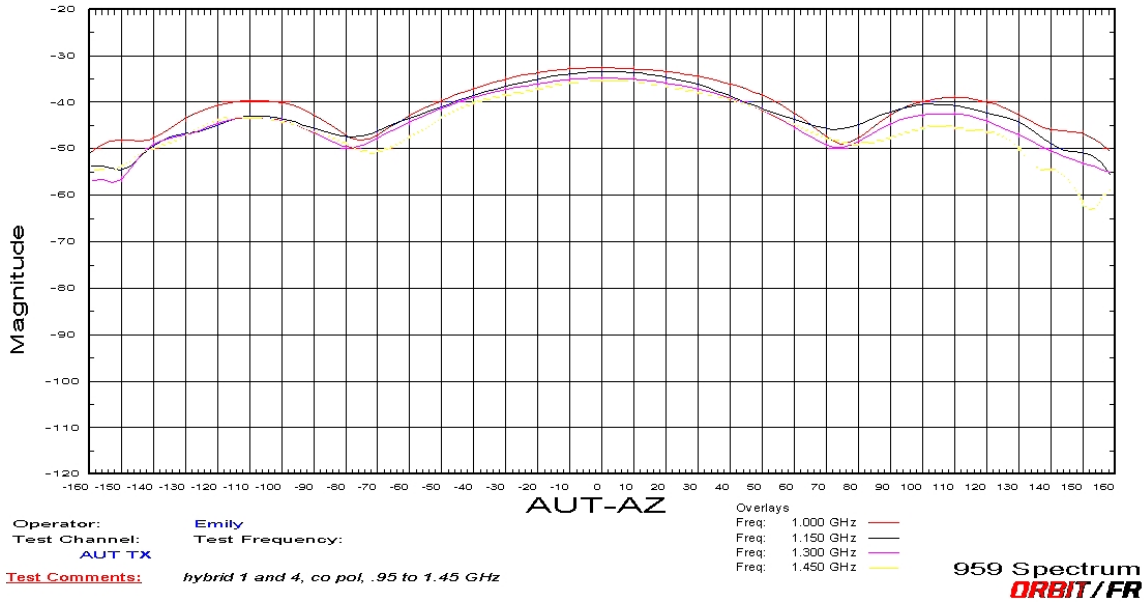

(a) Frequency range 1 GHz to 1.45 GHz

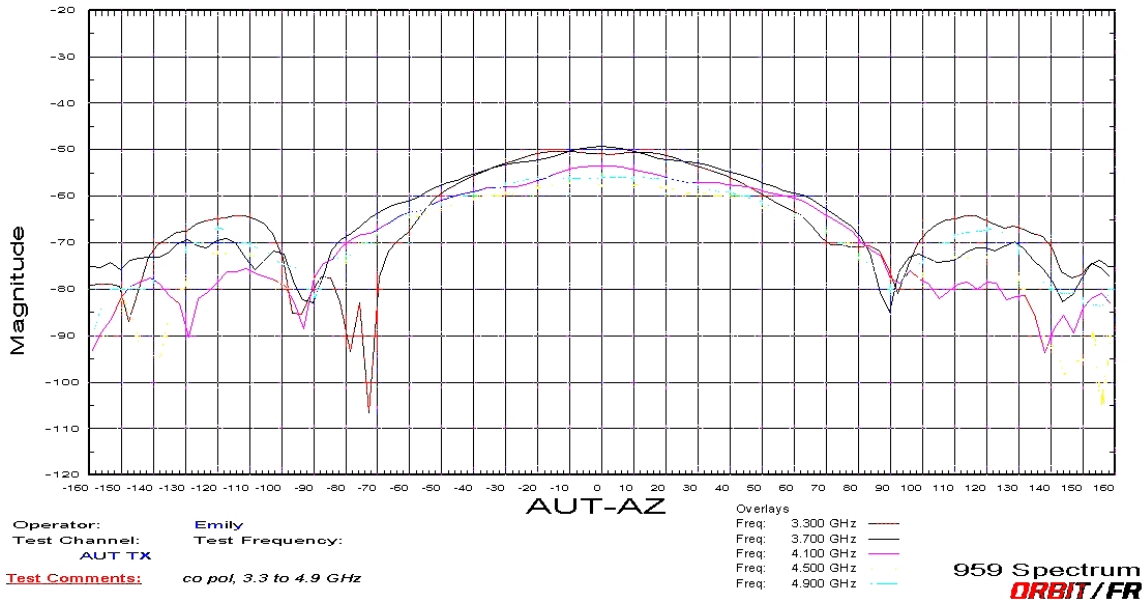

(b) Frequency range 3.3 GHz to 4.9 GHz

Figure 5.12: Co-pol as a function of $\theta < |160|$ degrees, on a -20 to -120 dB scale, for $\phi = 0$ at the lower frequencies.

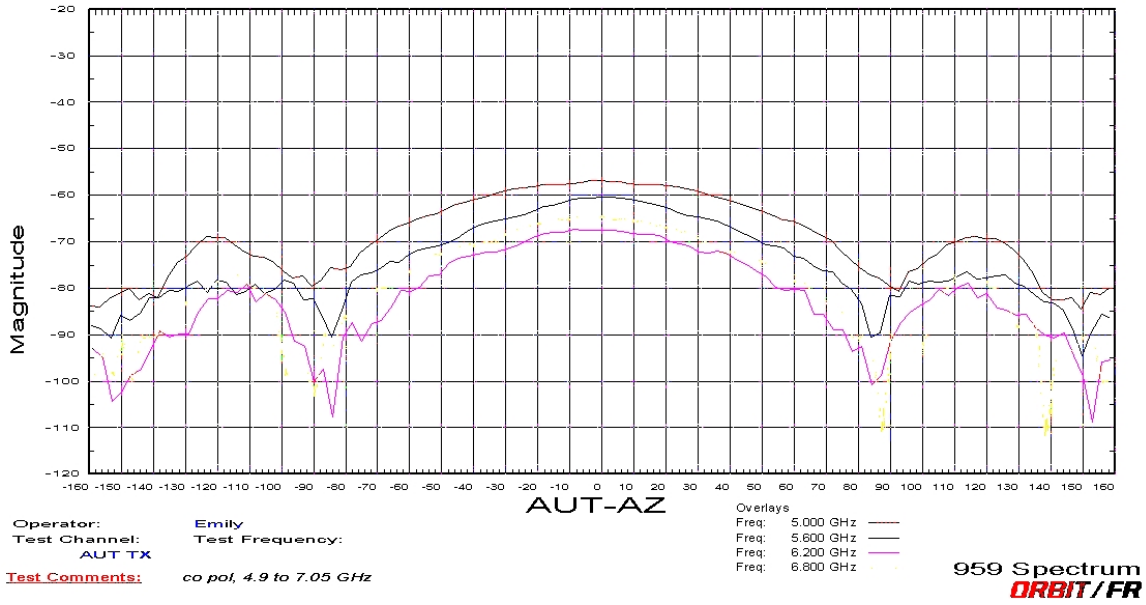

(a) Frequency range 5 GHz to 6.8 GHz

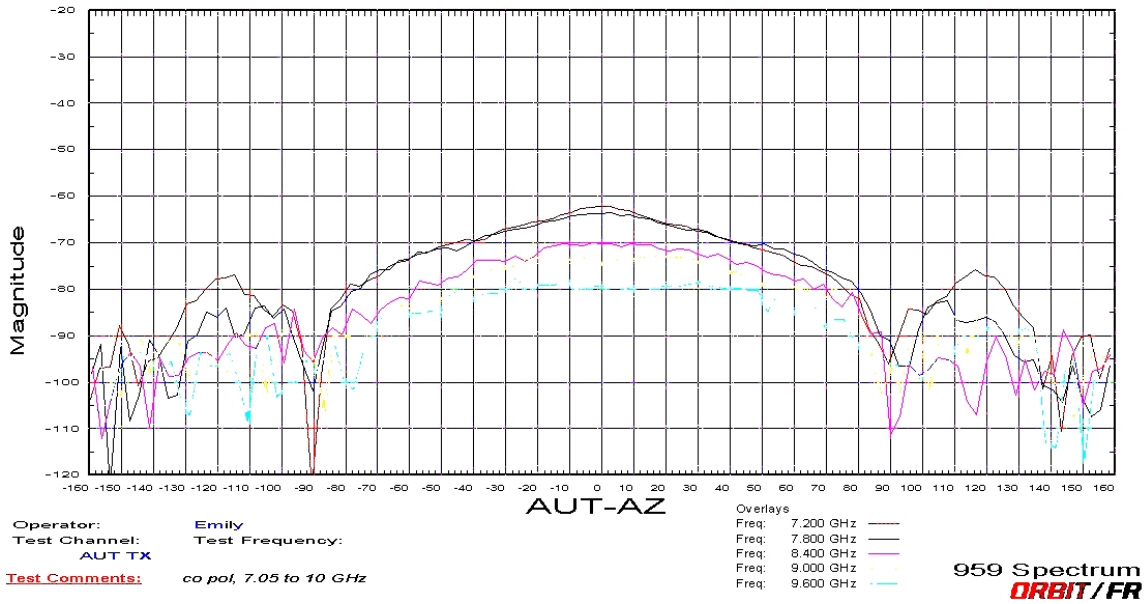

(b) Frequency range 7.2 GHz to 9.6 GHz

Figure 5.13: Co-pol as a function of $\theta < |160|$ degrees, on a -20 to -120 dB scale, for $\phi = 0$ at the higher frequencies.

5.5.3 Two-Dimensional Patterns at Multiple ϕ Values

As discussed in Section 4.3, an ideal three-dimensional beam pattern would have equal E-plane and H-plane beamwidths. In radio astronomy, the 10 dB taper is often used to define the beamwidth of the main beam, as compared to the half-power beamwidth often used in telecommunications. This convention derives from the basis of situating the feed antenna at a distance (referred to as the focal length) from the dish such that it illuminates the edge of the dish with a power density that is 10 dB below the power density at the boresight of the antenna. This half-width 10 dB taper angle was designed to be comparable to the half-width 10 dB taper of about 65 degrees for the QSC feed [10] and about 60 degrees for the Eleven feed [22], so that similar focal length to dish diameter (f/D) ratios for dish geometries could be used for all three feeds.

In addition to equal E-plane and H-plane beamwidths, a consistent radiated power level at -10 dB beamwidth angle for the intermediate values of $0 < \phi < 90$ degrees is desired to efficiently illuminate the dish. Although 3-D patterns can provide valuable qualitative information, multiple 2-D cuts at a set of ϕ values can provide quantitative information as well. This data is presented in Figure 5.14 through Figure 5.17. As there is a very wide range of frequencies to choose amongst for this "snapshot", we arbitrarily elected to present these 2-D slices at the highest frequency in the operating range for each of the measuring probes, or in the case of the highest frequency probe, at the AUT's maximum frequency of operation.

Figure 5.14 shows the co-pol E-field as a function of θ for $\theta < |160|$ degrees for the differential excitation of $Petal_1$ and $Petal_4$ in 2-D planes of ϕ = 0, 15, 30, 45, 60, 75 and 90 degrees. The polar plot shows that the beam remains consistent across this range of ϕ values for $\theta < |40|$. The 10 dB taper predominately occurs at the value of $\theta = |60|$ degrees; however, the 10 dB taper approaches $\theta = |50|$ degrees in the E-plane. Additionally, the side lobes at $\theta \approx |110|$ are about 10 dB below the main beam. Note however that the side lobe level (SLL) at θ =-110 is larger than the SLL at θ = 110. This asymmetry in the radiation pattern can be explained by the asymmetry in the network that fed the antenna,

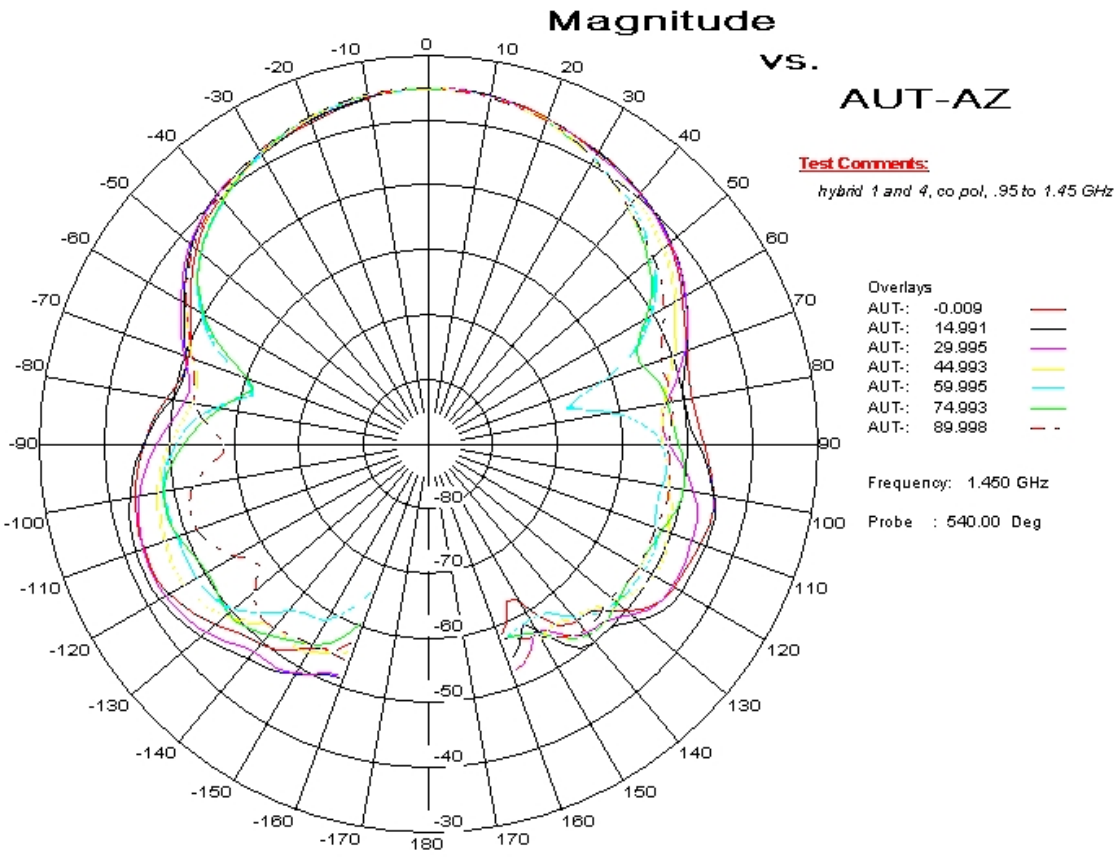

Figure 5.14: Co-pol radiated from $Petal_1$ and $Petal_4$ at 1.45 GHz as a function of θ, at $\phi = 0$, 15, 30, 45, 60, 75 and 90 degrees.

specifically the uneven power division and the deviation from a 180 degree difference in the phase (Figure 5.11) at the two output ports of the low frequency 180 hybrid at 1.45 GHz and was not seen in the simulated 2-D patterns at $\phi = 45$ degrees of Figure 5.19.

Figure 5.15 and Figure 5.16 also show the co-pol E-field radiated from $Petal_2$ and $Petal_3$ at frequencies 4.9 GHz and 7.05 GHz, respectively, again as a function of $\theta < |160|$ degrees at $\phi = 0$, 15, 30, 45, 60, 75 and 90 degrees. Again note that the pattern is about 10 dB below the main beam at $\theta = |60|$ in the E-plane, although there is some variation in the -10 dB taper at other ϕ-plane slices. Again, the SLL is generally under -10 dB at both of these frequencies.

Finally, Figure 5.17 shows co-polarized E-field from $Petal_2$ and $Petal_3$ at 8 GHz, again

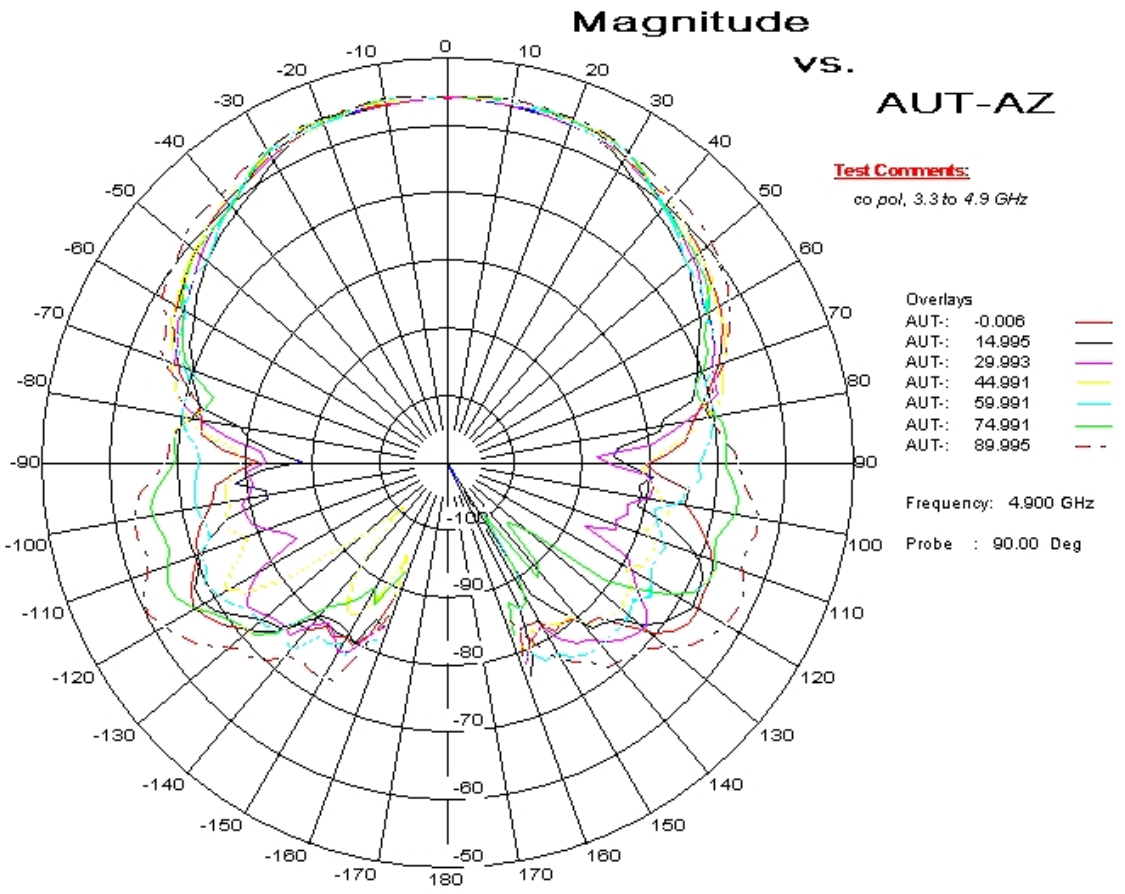

Figure 5.15: Co-pol radiated from $Petal_2$ and $Petal_3$ at 4.9 GHz as a function of θ, at ϕ = 0, 15, 30, 45, 60, 75 and 90 degrees.

as a function of $\theta < |160|$ degrees at $\phi = 0$, 15, 30, 45, 60, 75 and 90 degrees. Unfortunately, in the pattern there is substantial variation amongst the ϕ cuts and it is difficult to give a uniform 10 dB taper or the SLL value, although the average values are roughly similar to those stated for the lower frequencies. This relatively poor pattern performance could possibly be explained by increasing negative effects of any deviation from a differential signal feed or a differential geometry, which becomes more electrically significant as the physical antenna components become electrically larger as compared to the smaller wavelengths at higher frequencies. The presence of components with finite dimensions, such as the coaxial cables, are also seen to become more significant at the higher frequencies, as evidenced in the

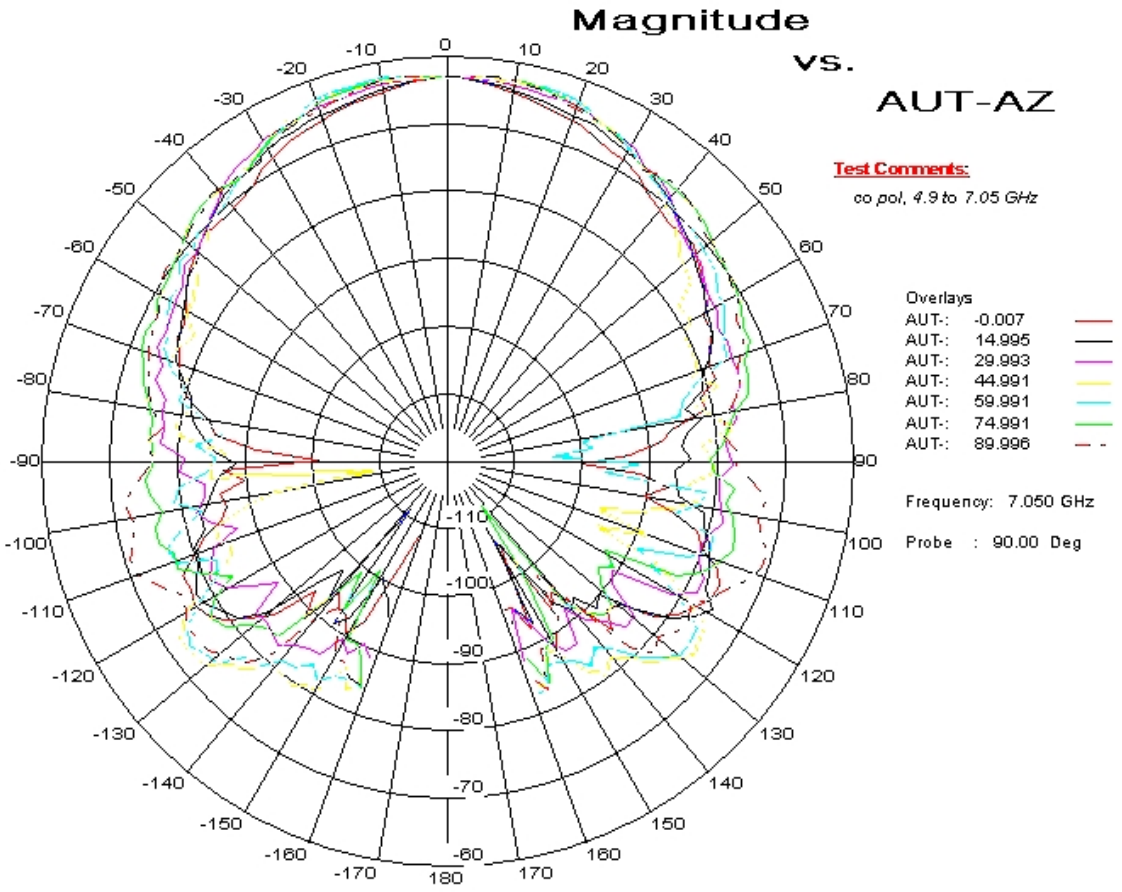

Figure 5.16: Co-pol radiated from $Petal_2$ and $Petal_3$ at 7.05 GHz as a function of θ, at ϕ = 0, 15, 30, 45, 60, 75 and 90 degrees.

loss of the smooth features in the lower frequency simulated far-field patterns of Figure 4.3 as compared with the higher frequency simulated far-field patterns of Figure 4.4. However, despite this roughness in the far-field patterns, there is still a symmetry in the simulated patterns at 8 GHz amongst the E-plane ($\phi = 0$ in Figure 4.4e) and the H-plane ($\phi = 90$ in Figure 4.4f) supports the conjecture that the asymmetry seen in physical measurements of Figure 5.17 is in fact due to the physical asymmetries of the differential signal feed and differential geometry as these physical asymmetries were not present in the simulated CAD model.

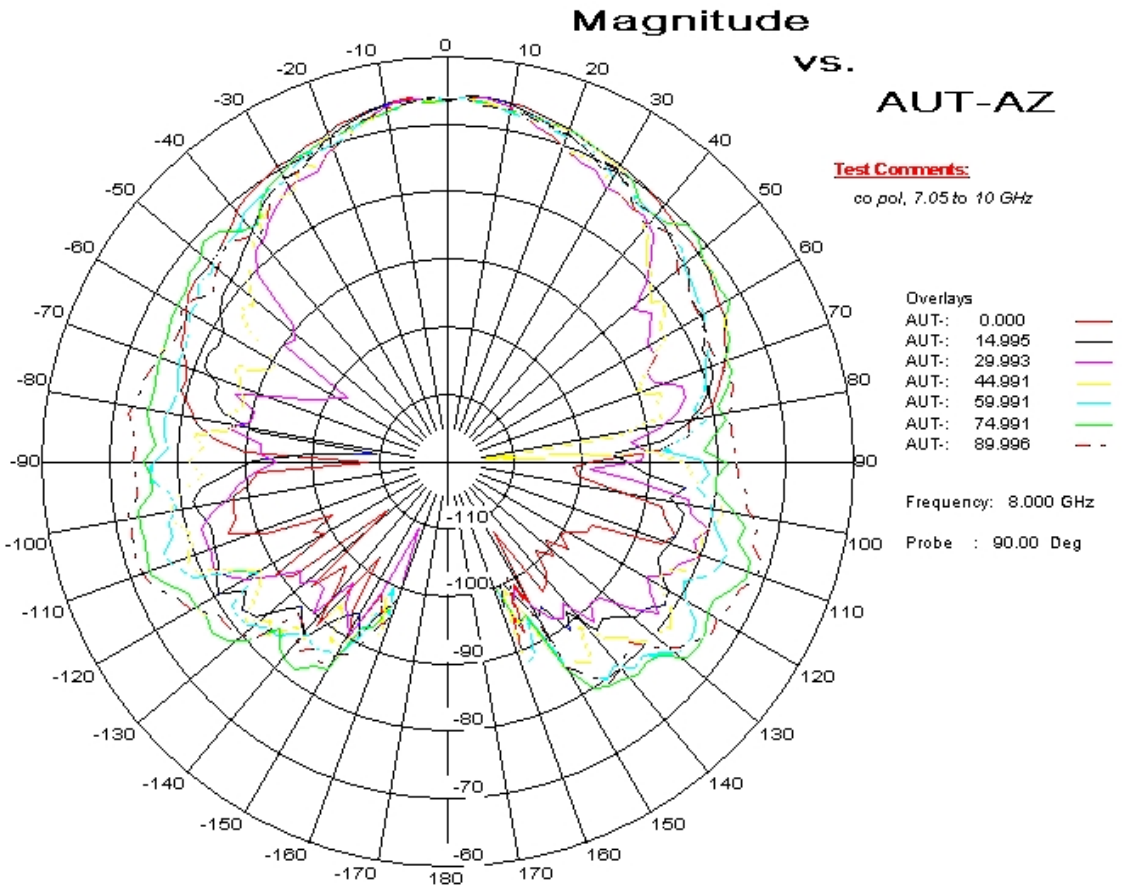

Figure 5.17: Co-pol radiated from $Petal_2$ and $Petal_3$ at 8 GHz as a function of θ, at $\phi = 0$, 15, 30, 45, 60, 75 and 90 degrees.

5.5.4 Co-pol and X-pol Patterns at $\phi = 45$ degrees

We again note that one particular 2-D plane of interest in terms of the co-pol and x-pol field is that along the $\phi = 45$ degrees plane. Due to the sensitive requirement of differentially balanced fields to reduce the x-pol, we elected to investigate the x-pol component at the specific frequencies at which 180 degree hybrids provided power evenly to the two petals of interest.

Figure 5.18a shows the co-pol (red line) and x-pol (blue-line) E-field component of the far-field pattern, radiated at $\phi = 45$ degrees from the differentially excited petals one and four. Note that the x-pol component is about 20 dB below the co-pol component at the

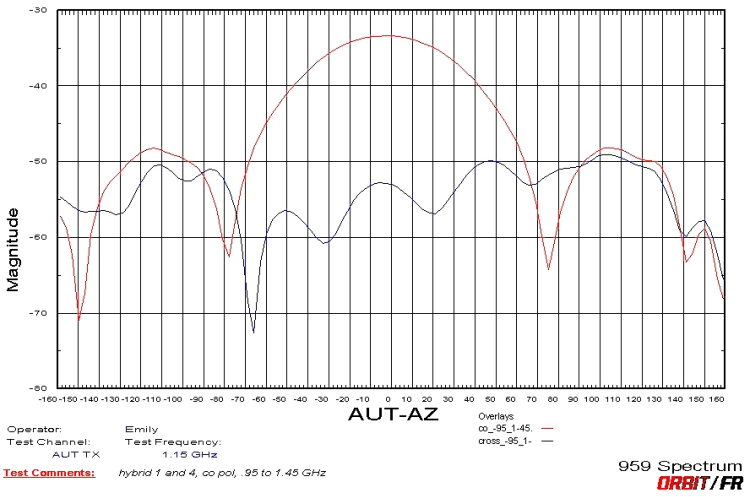

(a) 1.15 GHz

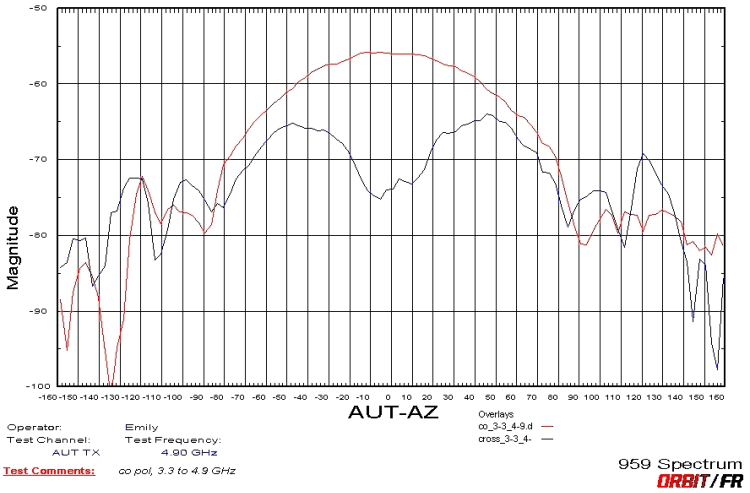

(b) 4.7 GHz

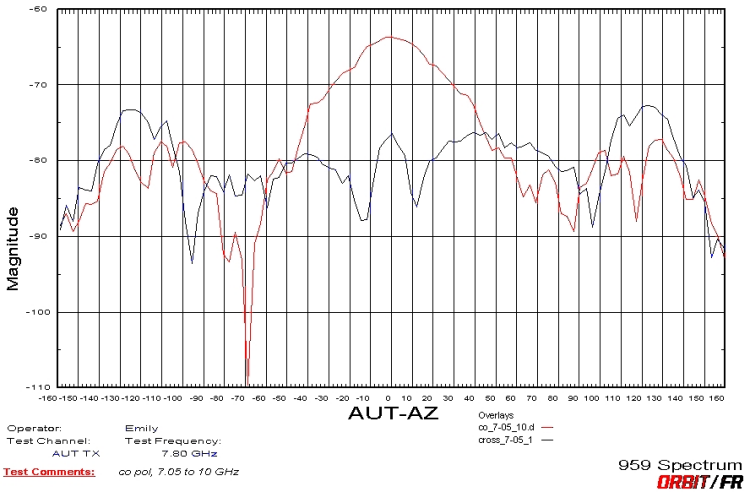

(c) 7.8 GHz

Figure 5.18: Co-pol and x-pol measured far-field 2-D slices at $\phi = 45$

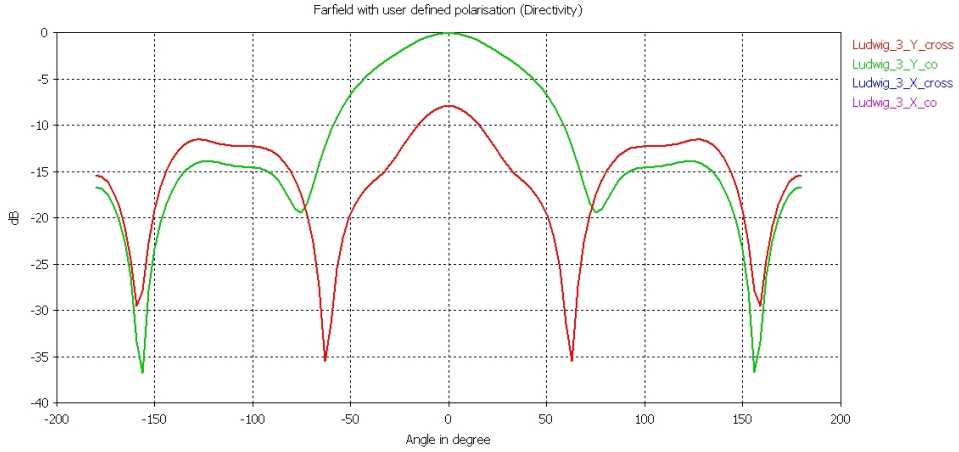

(a) 1 GHz

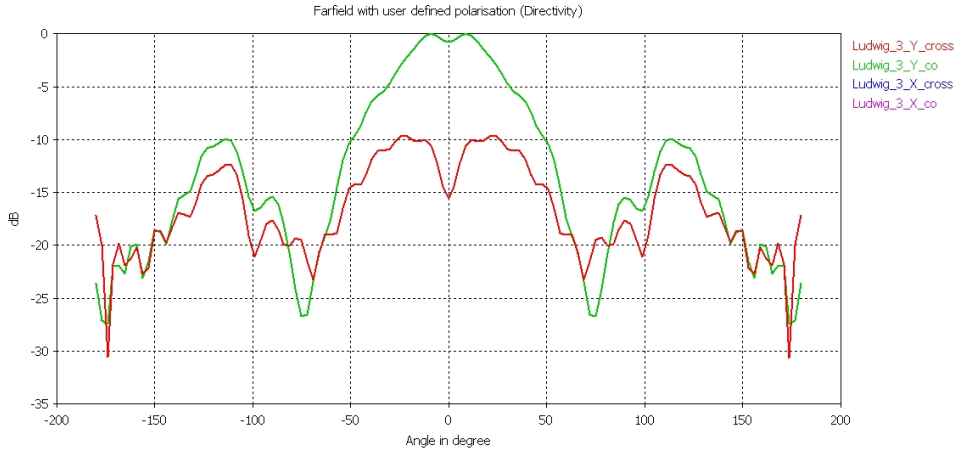

(b) 4 GHz

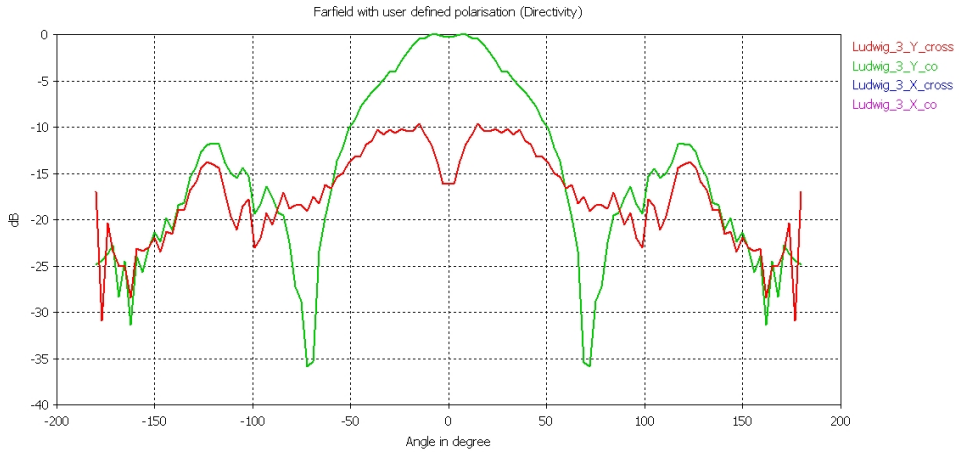

(c) 8 GHz

Figure 5.19: Simulated co-pol (green line) and x-pol (red line) 2-D patterns at $\phi = 45$ degrees.

boresight of the antenna at $\theta = 0$ degrees. As we reach $\theta = |60|$ degrees, the XPL decreases to about 5 dB.

In Figure 5.18b we see again that the XPL at 4.7 GHz is ≈ -20 dB on boresight, and decreases to about 1 dB as $\theta = |60|$ degrees along the $\phi = 45$ degree plane. Finally, Figure 5.18c show that although the XPL level is about 15 dB on boresight, it is 0 dB or higher at $\theta = |60|$ degrees on the $\phi = 45$ degree plane.

The simulated co-pol (green line) and x-pol (red line) 2-D patterns at $\phi = 45$ degrees are presented in Section 4.3.2 reproduced here are generally seen to be comparable to the measured patterns of Figure 5.18. The presence of a high x-pol field on boresight is seen in measured data of Figure 5.18c, but not in simulated data Figure 5.19c, initially appears to be an artifact of a measurement probe mis-alignment [26]. This explanation, however, is unlikely due to the absence of an x-pol null on boresight in the simulated pattern of Figure 5.19a as well, where the probe alignment is ideal. An alternative explanation for the absence of a null on boresight can be explained by the absence of a necessarily even-mode current distribution on the differentially fed, 180 degree rotationally symmetric petals.

5.5.5 Differentially Combined Patterns

As explained in Section 4.2.1 the radiation patterns from two distinct single-ended excitations of the two petals that comprise a single polarization are vectorially combined to obtain the "differential far-field" pattern in simulation. To determine the validity of this simulation step in practice, we also excited individual petals in a single-ended measurement while the three other petals were terminated in 50 ohms.

Figure 5.20 shows the co-polarization of the single-ended excitation of 5.20a petal one with petals two through four terminated, and 5.20b petal four with petals one through three terminated in 50 ohms. In these individual petal measurements, the single ended petals are excited with identical signals, thus ideally generating identical instantaneous surface currents on the petals. However, in a differential mode of operation, the surface currents of the two petals should be 180 degrees out of phase. This 180 degree phase difference can be

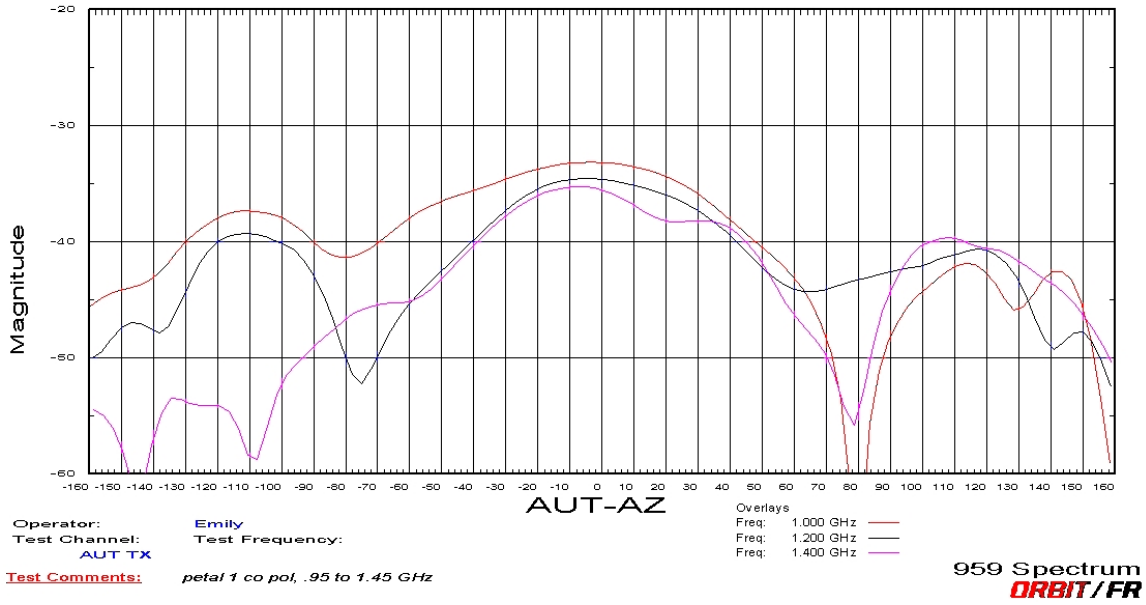

(a) Measurement of petal one with petals two through four terminated in 50 ohms

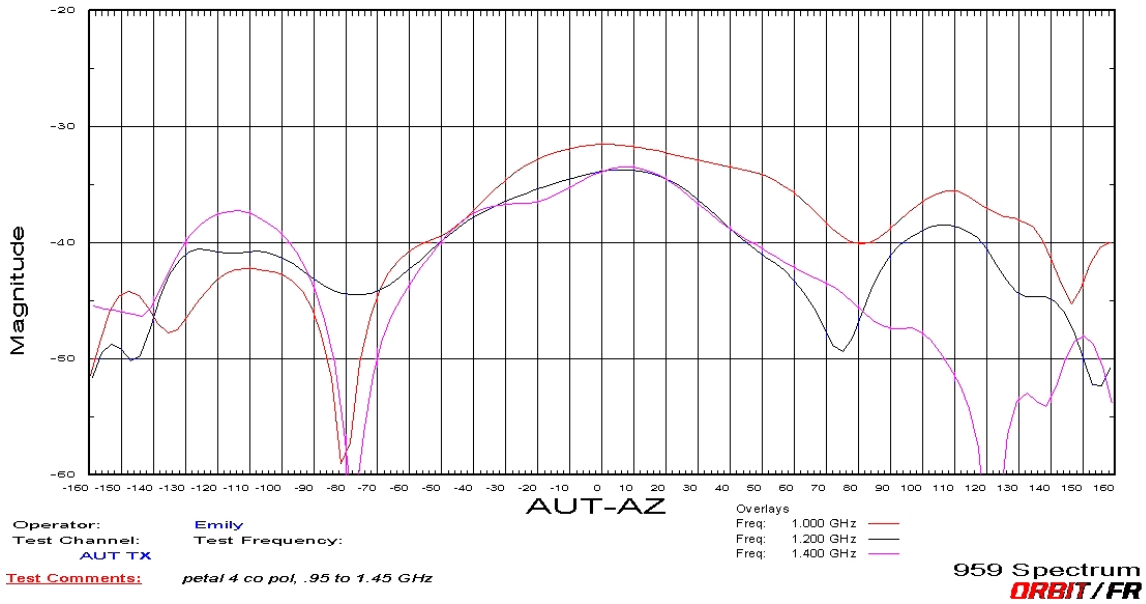

(b) Measurement of petal four with petals one through three terminated in 50 ohms

Figure 5.20: Co-polarization of single-ended excitation measurements as a function of at $\theta < |160|$ degrees at $\phi = 0$.

achieved by shifting the phase of one petal relative to the other by a relative phase change of $e^{j\theta_0+180} = -e^{j\theta_0} = -1$ if we set $\theta_0 = 0$.

Thus, the surface currents can be transformed from common mode currents to differential currents by simply subtracting the complex vector values of the surface currents on one petal from the surface currents on the other petal. We seek to achieve the same transformation in the qualities that we have measured: the electric component of the far-field. As mentioned earlier, the relationship between the surface currents on the antenna and its radiated electric field is a Fourier Transform relationship. Due to the linearity of the FT, the operation of taking the difference of the two complex electric vector fields radiated from the two petals should produce a resulting combined electric field identical to the electric field radiated from the two petals with differential surface currents.

Figure 5.21a is the result of the complex vectorial subtraction of the single petal's E-field in Figure 5.20a from that in Figure 5.20b. Alternatively, Figure 5.21b is the far-field pattern produced by the real-time differential excitation of petals one and four using the 180 degree hybrid as described in Section 5.5. The approximate 6 dB difference between 5.21a and 5.21b can be explained by the fact that the mathematically derived pattern is the combination of two measurements and thus contains twice the total power received by the probe during a single measurement. This doubling of power, or 3 dB difference in power, is equivalent to a 6 dB difference in the E-field component [39], confirming the validity of our method of vectorially subtracting two single-ended far-field patterns to find the combined differential far-field pattern.

5.6 LPLS Scattering Parameter Measurements

For S-parameter measurements, we used Agilent's N5230A PNA-L 4 port Vector Network Analyzer (VNA) [40]. Our first step was to electronically calibrate the VNA to four phase stable 50 ohm cables using Agilent's E-cal N4433A, with a precision calibration technique obtaining a level of accuracy similar to that of the "Through, Reflect, Line" calibration

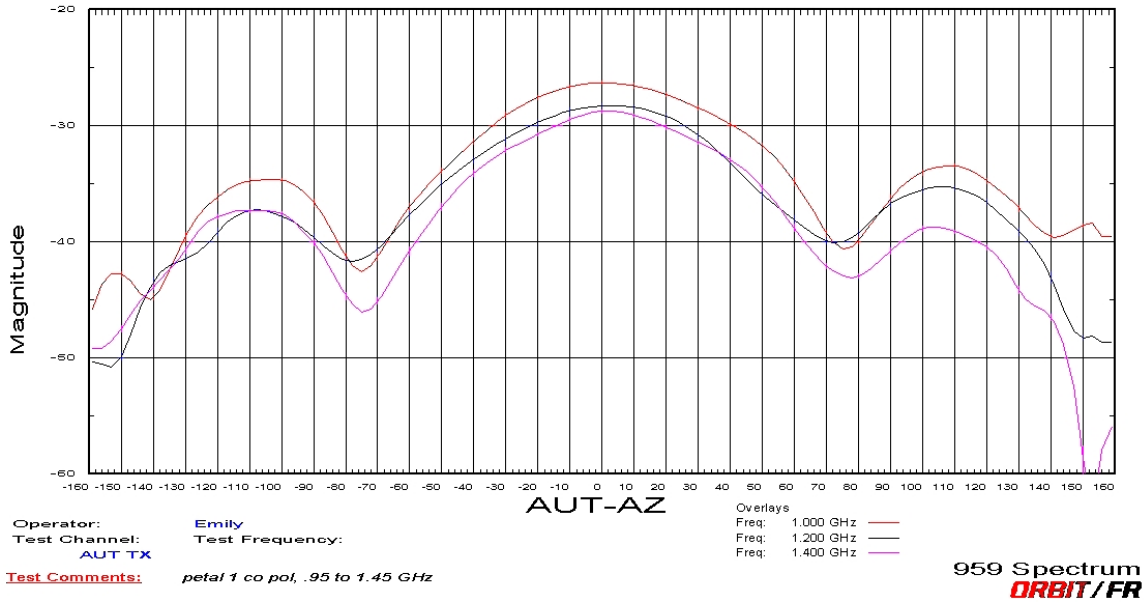

(a) Mathematically derived differential combination petals one and four

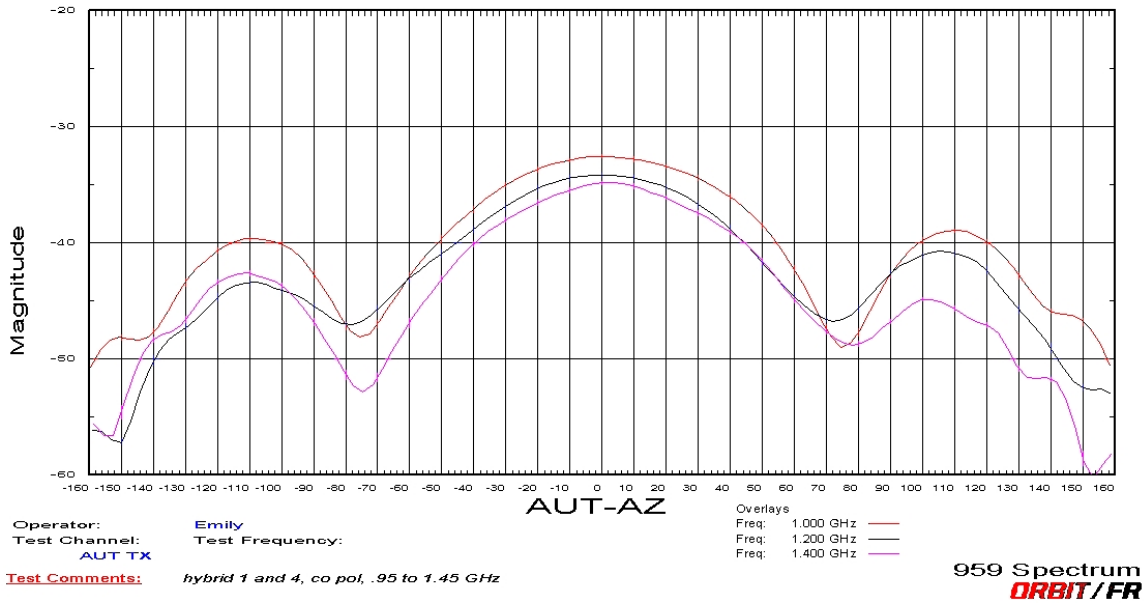

(b) Physically derived differential combination petals one and four

Figure 5.21: Co-polarization of differential pattern measurements as a function of at $\theta < |160|$ degrees at $\phi = 0$.

standard [41].

5.6.1 Measurement Procedure

As discussed in Section 5.2, the petals are directly soldered to 73 mm of 50 ohm co-axial cables that are terminated with SMA connectors. Subsequent to calibration, the SMA connectors of all four petals of the AUT are connected to the phase stable cables that were calibrated to the VNA, and the AUT is oriented such that the majority of its radiated power is directed toward RF-absorbing foam. Port 1 and port 4 are attached to $Petal_1$ and $Petal_4$, which comprise one polarization of the AUT, while $Petal_2$ and $Petal_3$ comprise the orthogonal polarization. Port 1 is excited and s_{11} , s_{21}, s_{31} and s_{41} are measured relative to the VNA's 50 ohm impedance. The measured 4-port data is then uploaded into ADS for data plotting and analysis.

5.6.2 Raw Data

The raw S_{11} (and the reciprocal S_{44}) measurements shown in Figure 5.22a are very poor. Somewhat poor results can be expected due to the impedance mismatch between the transmission line to AUT. The measured data is matched to a single-ended 50 ohm load, whereas the singled-end impedance of the petals is closer to 130 ohms. Additionally, the reference plane for these results is located 73 mm from the actual feedpoint where the 130 to 50 ohm mismatch occurs. The impedance mismatch sets up a standing wave pattern that is transformed along the length of the co-axial. This transformation can be seen in the plot of the raw data on the Smith Chart (Figure 5.22b) that appears to be smeared along constant $|\Gamma|$ circles, as discussed in Section 4.5. After the effects of the 73 mm co-ax have been extracted from the measurements, a renormalization on the Smith Chart should yield the results similar to the simulated results found in Section 4.6.

(a) Single-ended S_{11} and S_{44} measured data plotted in dB

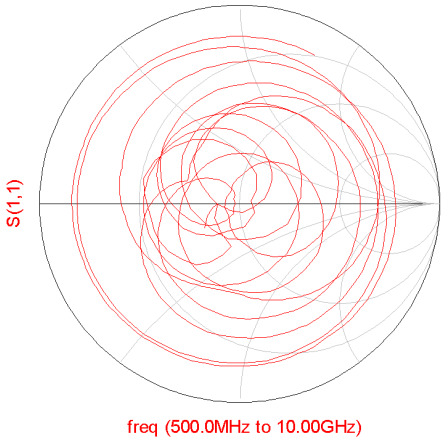

(b) Single-ended s_{11} data plotted on the Smith chart

Figure 5.22: Raw data captured from VNA and plotted using ADS.

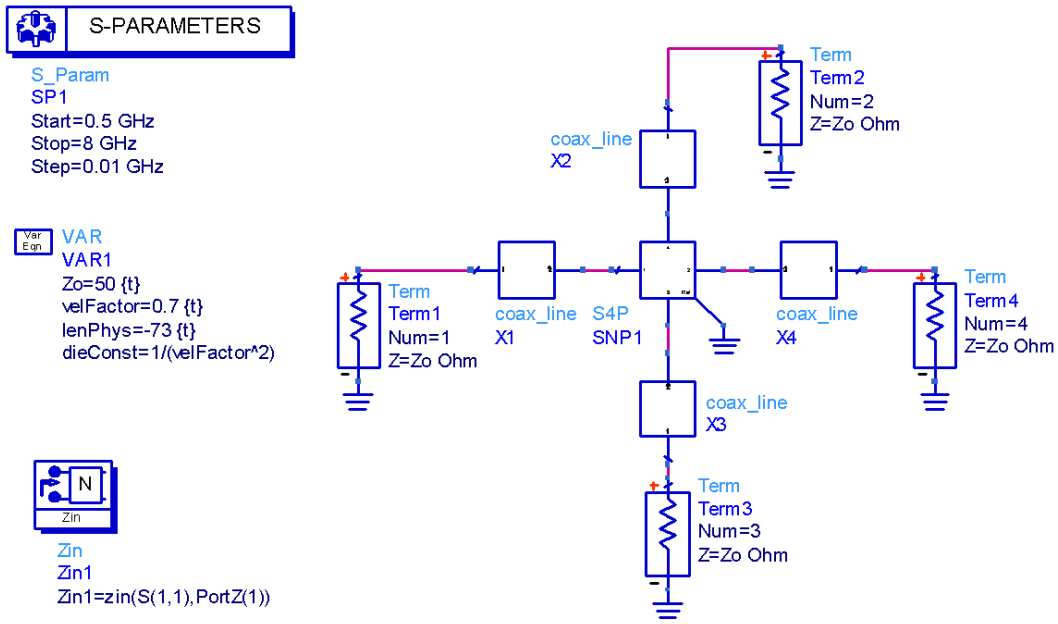

Figure 5.23: ADS model with an introduction of dummy transmission line -73 mm in length.

5.6.3 ADS De-embedding

The effects of the 73 mm of co-ax can be de-embedded from the data by introducing dummy transmission lines with identical characteristics to those of the measured co-axial cables, but with a length of negative magnitude of the actual cable's lengths as discussed. In the ADS model as shown in Figure 5.23, the complete 4-port (S4P) VNA measurements are uploaded to ADS and represented by the "SNP1" block in the schematic. The 4 ports of the VNA are represented by the 50 ohm terminations "Term1" through "Term4". Finally, the "coax_line" block elements $X1$ through $X4$ are simply distributed circuit models of dummy transmission lines with 50 ohms impedance, a $0.7c$ velocity factor, and a "length" of -73 mm. Without these "coax_line" blocks, the ADS model would present the exact data captured on the VNA. The addition of these "coax_line" blocks move the measurement reference plane 73 mm toward the AUT, to the position where the actual inner conductors of the transmission lines attach to the petals.

5.6.4 Inductive Results

Although de-embedding the 73 mm transmission line does not change the magnitude of the S-parameter measurements, we see its profound effect on the phase S-parameter measurements in the Smith chart plot (presented in Figure 5.25a). For an ideal frequency independent antenna, a renormalization of the Smith chart could center the real part of antenna's feedpoint impedance, $\Re\{Z_a\}$, to the middle of the chart. This renormalization would result in a reduction of the magnitude of the s_{11} measurements to values closer to those achieved in simulation (such as Figure 4.7b), in which the AUT is matched to transmission lines with $\Re\{Z_a\} \approx 130$ ohm impedance. However, the efficacy of this renormalization is limited to only some small portion of the bandwidth. This bandwidth limitation is because the measured data reveals a frequency dependent behavior in the reflection coefficient. Specifically, we are now able to identify an increasingly inductive component in the Smith chart plot that resembles an uncoiled slinky with the higher frequencies becoming more inductive as

the curve reaches further into the upper hemisphere of the Smith chart. This undesirable unwinding of the plotted curve was not exhibited in the simulated Smith chart results (represented in Figure 5.28b). Rather, the simulated Smith chart plots were slightly capacitive, as indicated by the presence of the plot in the lower hemisphere. The unexpected inductive component in these results prompted a re-investigation of the simulated model.

5.6.5 Capacitive Culprit

A closer investigation of the original simulation model revealed a residual appendage of excessive material left behind from an earlier CAD model, as shown in Figure 5.24a. The prototype was constructed to resemble the CAD model of Figure 5.24b, without this extra conductive material near its feedpoint. This additional 1.5 mm of coax outer conductor had not been incorporated in either theoretical modeling or physical prototyping of the AUT, however, its effects unwittingly guided our design decisions based on simulation analysis. Subsequent to this realization, a follow-up re-simulation was completed without the outer conductor shields extending beyond the cone top. The shunt capacitive effect due to the presence of the excessive shielding appendage becomes apparent when comparing the data from the models with the excess shielding to data from the models without the excess shielding, as will be done in Section 5.6.6.

We find the re-simulated data of the CAD model (Figure 5.24b) without the excessive shielding to be more comparable to the measured data of the prototype that also lacked the excessive shielding. The measured Smith Chart of Figure 5.25a can be directly compared to the re-simulated Smith Chart of Figure 5.25b, in which the plots show the similarity that one would expect between the measured data and simulated data. Additionally the re-simulated S_{11} data of Figure 5.26b is similar to the measured S_{22} data, reproduced here for ease of comparison in Figure 5.26a.

It also appears that the presence of the excessive shielding increased the real part of the feed impedance as well. The re-simulated Smith chart results are shifted from the center of the chart toward the short circuit (left) side of the Smith Chart (Figure 5.25b) suggesting

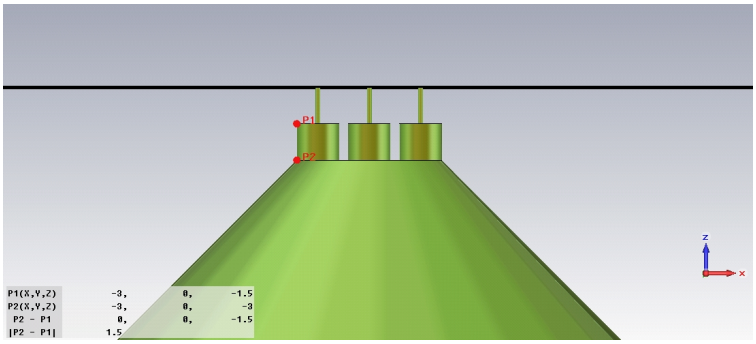

(a) Capacitive-appendage version revealing outer co-axial shields extending 1.5 mm beyond the cone top

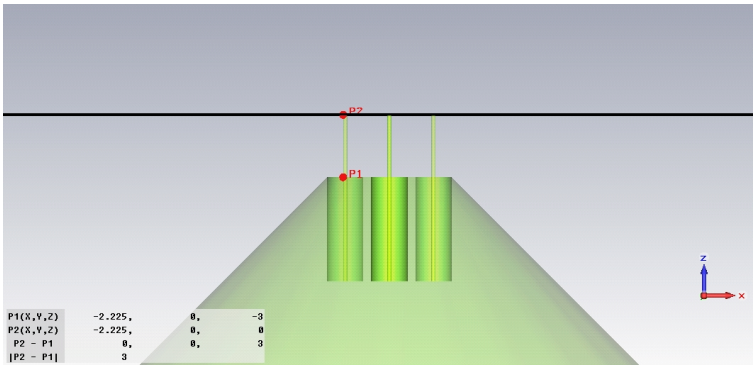

(b) Re-simulated version (shown with a partially transparent cone), which is a more accurate representation of the built prototype

Figure 5.24: Close-up of CAD models with the (a) presence and (b) absence of the excessive 1.5 mm of copper shielding.

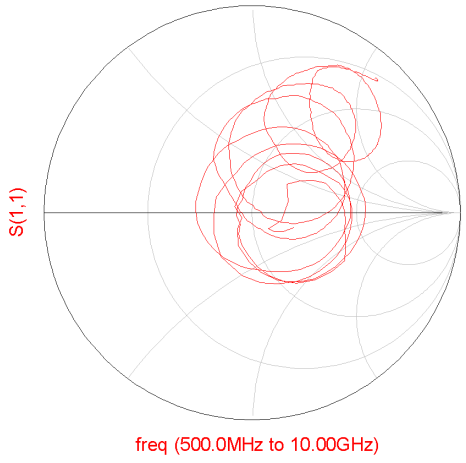

(a) Measured s_{11} results

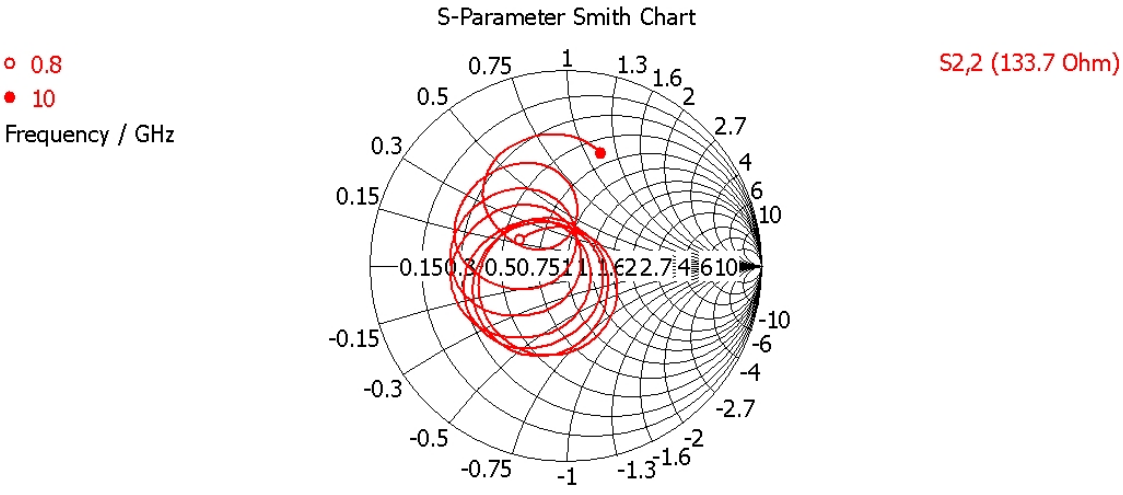

(b) Re-simulated s_{22} (equal to s_{11}) results

Figure 5.25: Smith chart plots without the capacitive component.

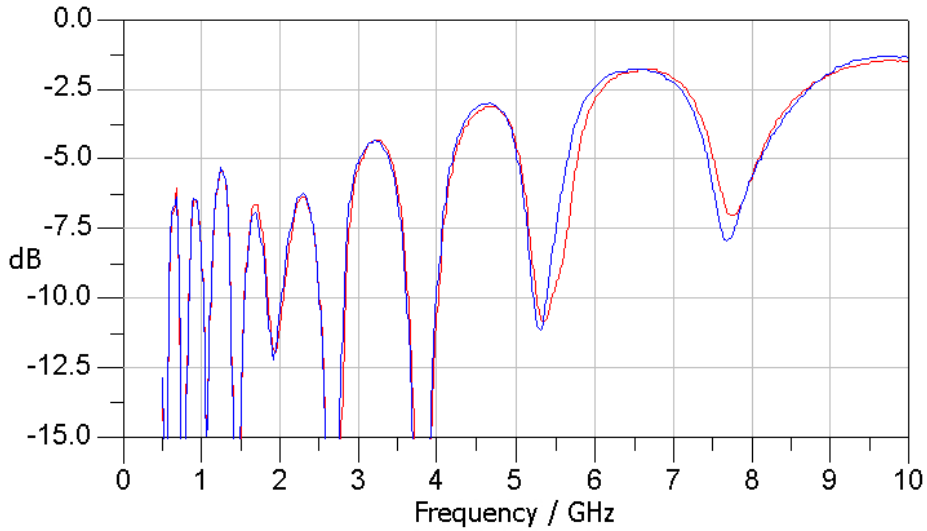

(a) Measured S_{11} and S_{44} results

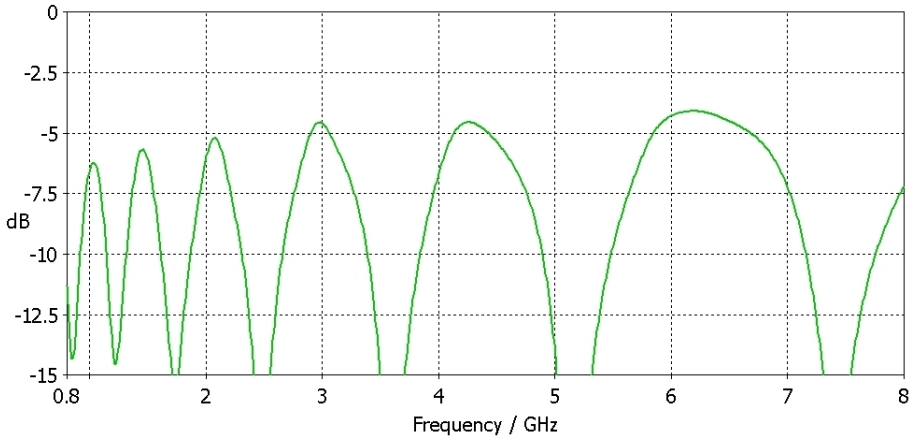

(b) Re-simulated S_{22} (equal to S_{11}) results

Figure 5.26: Single-ended reflection coefficient data without the capacitive component plotted in dB.

that the AUT presents a feedpoint impedance that is lower than that of the impedance transmission line, which at this time is designed to be about 130 ohms. We will investigate renormalizing the measured data to a lower value in the next section.

5.6.6 ADS Corrections

To achieve measured results similar to the more desirable results that we obtained from the CAD model with the excessive shielding, the prototype should incorporate a capacitive component near its feedpoint. Unfortunately, follow-up physical modification and measurements were not possible due to time constraints. However, ADS can be used to model the effect of adding a lumped capacitance to the antenna. This model can provide very accurate results because the modification is applied directly to the measured data. A lumped capacitative element is implemented in an ADS model very similar to that shown in Figure 5.23 for the 73 mm cable de-embedding. However, now the "coax_line" elements $X1$ through $X4$ include a shunt capacitor labeled "C", in addition to the -73 mm of transmission line labeled "TLNP". A schematic of one of these elements is shown in Figure 5.27. The value of "C" is set to 400 fF in the remaining results to be presented. An additional difference between this most recent ADS model and the one in Figure 5.23 is that the impedance of the terminations have been renormalized to $Z_0 = 80\,\Omega$. Figure 5.28a and Figure 5.29a shows the single-ended results of the real measured data after renormalization and the introduction of the shunt capacitor detailed in Figure 5.27

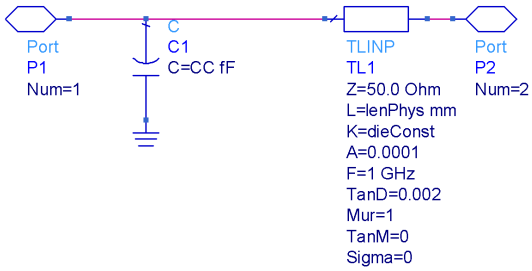

Figure 5.27: ADS model close-up.

The presence of the plotted data in the inductive portion (upper hemisphere) of the

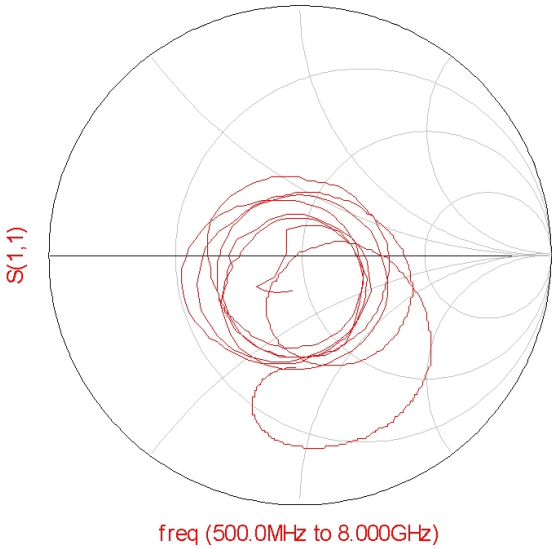

(a) Measured results modified in ADS

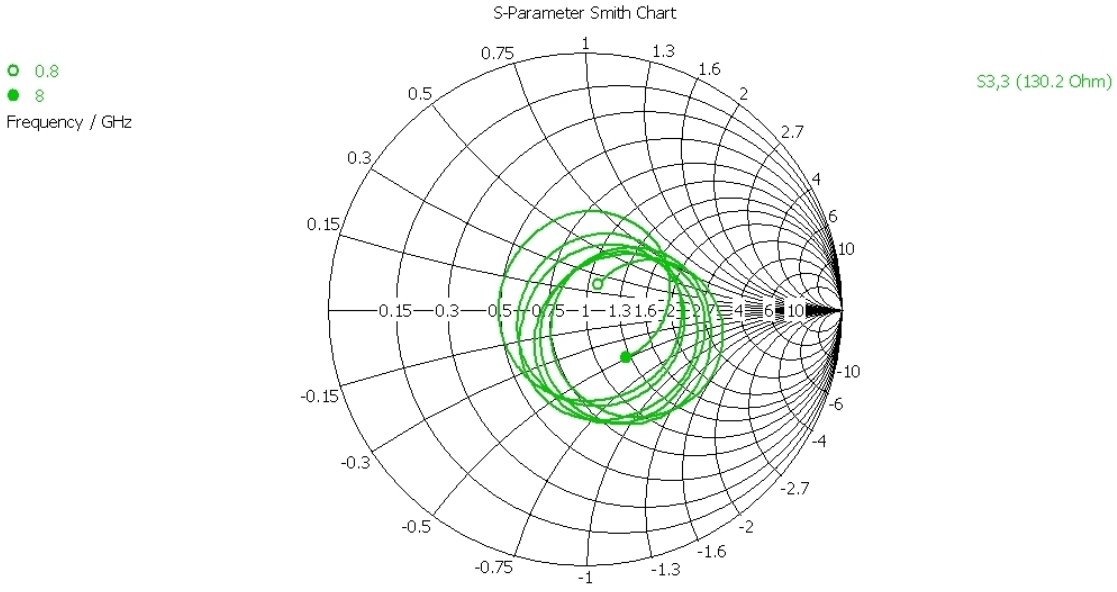

(b) Original simulation results from Section 4.6.1

Figure 5.28: Smith chart plots with the capacitive component.

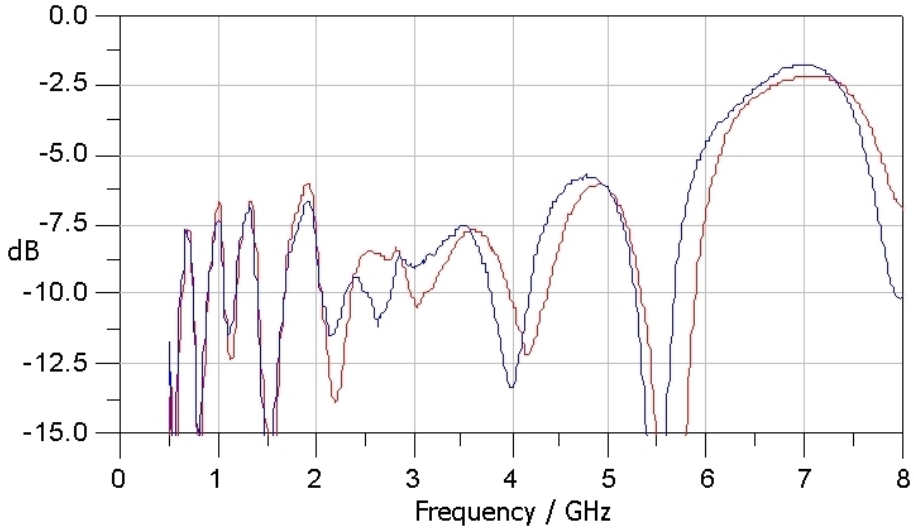

(a) Measured S_{11} and S_{44} results modified in ADS plotted in dB

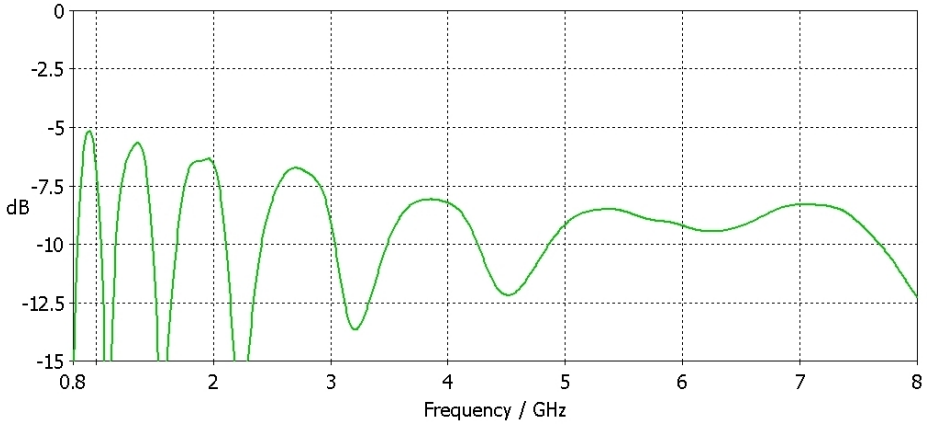

(b) Original simulation results of S_{22} (equal to S_{11}) from Section 4.6.1

Figure 5.29: Single-ended reflection coefficient data with the capacitive component plotted in dB.

Smith chart seen in the plots without the excessive shielding (Figure 5.25) as compared to the Smith chart plots with the excessive shielding (Figure 5.28), indicates the capacitive effect of that 1.5 mm excess of outer coax conductor near the feedpoint. Additionally, it is the higher portions of the frequency band that appears more inductive in the Smith chart plots of the model and prototype without the excessive shielding, whereas the lower portions of the frequency band are less effected by the presence of the excess shielding. Similarly, as frequency is reduced in a lumped element circuit model, the effect of a shunt capacitor is diminished until it has an infinitesimally small effect [39], further suggesting that the excessive shielding has the effect of a shunt capacitive element.

The modified measured results of Figure 5.28a and Figure 5.29a more closely resemble the original simulation results re-presented in Figure 5.28b and Figure5.29b, particularly in the frequency range of 0.8 GHz to 6 GHz. We propose that these modified measured results could be achieved with the introduction of the approximately 1.5 mm of additional conducting material at the feedpoint to counter the inductive reactance of the petals and to drive down the real component of the feedpoint impedance. We will propose in Chapter 6 some potential explanations of the frequency dependent behavior present in the measured results above 6 GHz, that was not encountered in simulation results above 6 GHz.

5.6.7 Differential Mode Measurement Results

Maintaining the 400 fF shunt capacitance detailed in Figure 5.27 and the 80 ohm real impedance modifications, ADS was utilized to calculate S_{dd11} employing Equation 4.8. These results in Figure 5.30a are again comparable to the original simulation results of Figure 4.8 (reproduced here in Figure 5.30b) in the frequency range of 0.8 GHz to 6 GHz.

We again note that although the magnitude of return loss is quite poor in comparison to more traditional antennas, these results are within the realm of the WB+SPF antennas currently proposed for the SKA such as the Eleven antenna [22].

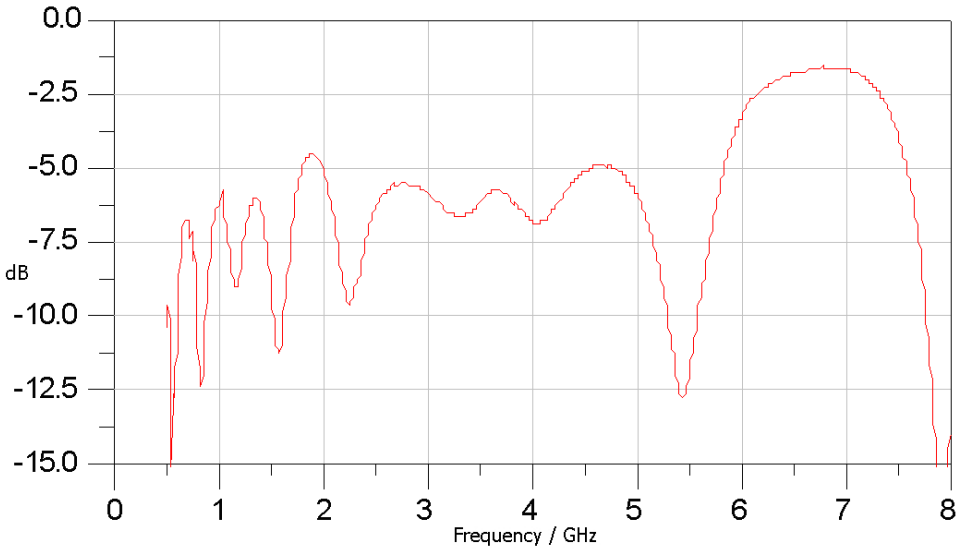

(a) Measured data of $S_{dd11} = S_{dd44}$ results with modified in ADS

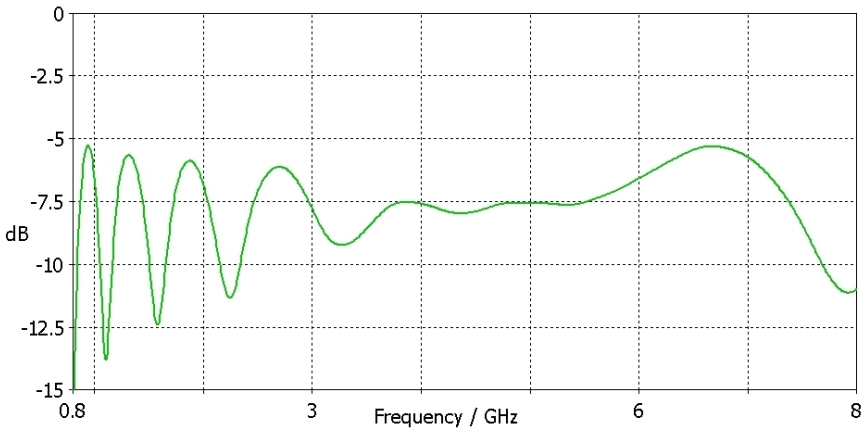

(b) Original simulation results of S_{dd22} (equal to S_{dd11}) from Section 4.6.2

Figure 5.30: Differential reflection coefficient data with the capacitive component plotted in dB.

5.6.8 Mixed Mode and Other S-parameters

We conclude this chapter with a brief examination of several S-parameter measurements that confirm assumptions made at earlier stages in this thesis.

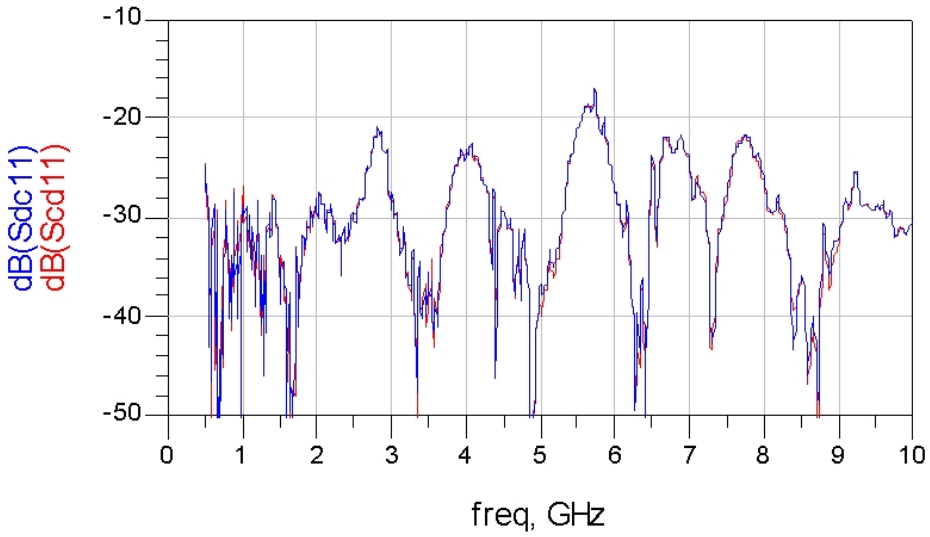

Figure 5.31: Measured transmission coefficient from common mode to differential mode: S_{dc11} and the reciprocal differential mode to common mode: S_{cd11} plotted in dB.

Figure 5.31 shows the transmission coefficient, or the mode conversion between differential and common mode currents, plotted with the theoretically reciprocal S_{dc11} and S_{cd11}. Depending upon the application, the magnitude of the transmission coefficient between two ports may be referred to as the isolation [39]. The measured isolation from the excited horizontal polarization of $Petal_1$ and $Petal_4$ to the 50 Ω terminated vertical polarization of $Petal_2$ and $Petal_3$ is generally above 20 dB. Due to the reciprocal nature of $Petal_1$ and $Petal_4$, the measured values of S_{21} and S_{31} are sufficient to indicate the isolation between the between the vertical and horizontal polarizations. This validates our use of Equation 4.8 and Equation 4.9 in the determination of the differential return loss, as these equations neglect the mode conversion components.

Additionally, differential mode to common mode current conversion would be introduced by asymmetries in the petal structure. Specifically, the 180 degree phase difference

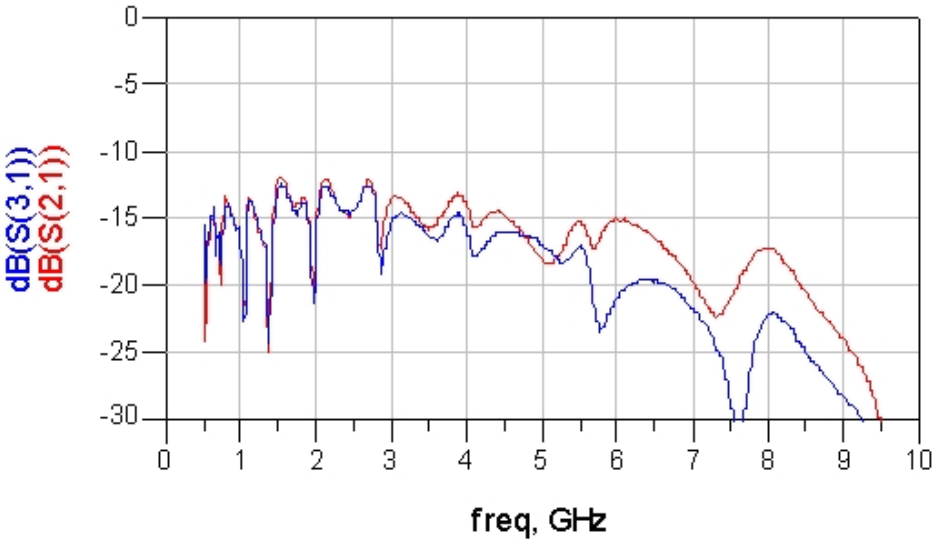

Figure 5.32: Measured transmission coefficient from the vertical polarization of $Petal_1$ to the horizontal polarization of $Petal_2$: S_{21} and $Petal_3$: S_{31} plotted in dB.

that describes differential mode currents, requires 180 degree rotational symmetry between the two petals that support the currents on a single polarization. The low level of mode conversion suggests that our construction efforts were sufficiently accurate in maintaining the ideal 180 degree rotational symmetry that was modeled in the CAD.

Finally, Figure 5.32 shows that the coupling from the horizontal polarization of $Petal_1$ and $Petal_4$ to the orthogonal polarization of $Petal_2$ and $Petal_3$ represented as S_{21} and S_{31}, is well under -10 dB across the band, indicating reasonably good isolation between the two vertically polarized and horizontally polarized petals in light of their close proximity to one another.

Chapter 6

Conclusions

The introduction of a non-planar ground surface to a previously unreported log periodic design permitted the low cost fabrication of a Wideband Single Pixel Feed, proposed for development for the Square Kilometer Array, the next generation radio astronomy telescope slated for 2020 completion date.

6.1 Comparison to Existing Technology

The initial results of the LPLS antenna over a conical ground surface compared well to the initial results of other antennas currently proposed for the SKA. A half width 10 dB taper of about 60 degrees, cross-polarization level of about 10 dB and differential return loss of 5 dB compares well the other WB+SPF antennas, as well as the LPLS simulation results. The advantage of low cost implementation of this antenna permits cost effective prototyping in efforts to improve the design, and should permit high yield implementation as would be required for the thousands of SKA dishes.

6.2 Suggested Revisions

Supporting the entire petal structure with the Teflon hardware located at the apex of the cone proved difficult and somewhat unstable. Maintaining rotational symmetry amongst the petals was crucial in the avoidance of the excitation of common-mode currents that will not contribute to the received signal. Locating features constructed on the Teflon hardware aided our successful situating of the petals in 180 degree opposition to one another, however, this was a very time consuming effort. Placement of additional supports and locating features on the outer edges of the petals may increase the efficiency of this construction process [33].

Considerable difficultly was encountered when attempting to reduce the differential return loss. It was found that increasing the distance between the petals and the ground surface could increase return loss at the cost of a degraded far-field pattern. This increase in distance can be accomplished by increasing the angle of the cone, or possibly changing the function that describes the surface of the cone from a linear function to some other curve.

6.3 Future Investigations

As suggested in the previous section, an investigation of the function from which the conical surface is extruded could provide interesting results. Shortly after the first order calculation that this function would ideally be linear with no constant offset, we fixed the angle at 45 degrees. Fixing this variable early in the process allowed time for the construction of the conical surface prototype component, which was a foreign procedure to us at the time. However, other variables continued to be varied and it is very likely that another angle would provide more optimal results. Additionally, the first order calculation for the function of the surface did not take into account coupling amongst the radiating components or fringing effects. Taking these complicating factors into account, it is likely that another function describing the surface, such as a Gaussian curve may produce better results.

The LPLS over a ground surface provided promising results with the variable values that were fixed for the prototype construction. There is great potential for improvement upon these results with the adjustment of these variable values or the introduction of another log periodic pattern atop the 3-D ground surface.

Bibliography

[1] R. T. Schilizzi, P. Alexander, J. M. Cordes, P. E. Dewdney, R. D. Ekers, A. J. Faulkner, B. M. Gaensler, P. J. Hall, J. L. Jonas, and K. I. Kellermann, "Preliminary specifications for the Square Kilometre Array," Dec. 2007. Available online at `http://www.skatelescope.org/PDF/Preliminary_SKA_Specifications.pdf`.

[2] Swinburne Astronomy Productions, "SKA Dish," 2010. Graphic provided as visual material available for journalists at `http://www.skatelescope.org/pages/journ_hrimages.htm`.

[3] Square Kilometre Array Consortium, "SKA configuration," 2010. Graphic provided as visual material available for journalists at `http://www.skatelescope.org/pages/journ_hrimages.htm`.

[4] P. Dewdney, P. Hall, R. Schilizzi, and T. Lazio, "The Square Kilometre Array," *Proceedings of the IEEE*, vol. 97, pp. 1482–1496, Aug. 2009.

[5] G. Engargiola, "Non-planar log-periodic antenna feed for integration with a cryogenic microwave amplifier," in *IEEE AP-S Int. Symp. Dig.*, vol. 4, pp. 140–143, 2002.

[6] V. H. Rumsey, *Frequency Independent Antennas*. New York: Academic Press, 1966.

[7] J. Descloitres, "Low off Iceland," Oct. 2010. From The Visible Earth, a catalog of NASA images and animations of our home planet, at `http://visibleearth.nasa.gov/view_rec.php?id=6204`.

[8] J. D. Kraus, *Antennas*. New York: McGraw-Hill, 2nd ed., 1988.

[9] J. Welch and M. Fleming, "Planned upgrade of the ATA feed," Tech. Rep. 5, US SKA Technology Development Project, Mar. 2009.

[10] G. Cortes-Medellin, "Novel non planar ultra wide band Quasi Self-Complementary antenna," in *IEEE AP-S Int. Symp. Dig.*, pp. 5733–5736, June 2007.

[11] P.-S. Kildal, R. Olsson, and J. Yang, "Development of three models of the Eleven antenna: A new decade bandwidth high performance feed for reflectors," in *Proc. European Conf. Antennas and Propagat.*, pp. 1–6, Nov. 2006.

[12] Gemini Multi-Object Spectrographs Team, "M74: The Perfect Spiral." NASA Astronomy Picture of the Day Collection, last accessed on 15, Jan., 2010 at `http://www.nasaimages.org/luna/servlet/detail/NVA2~4~4~4409~104935:M74--The-Perfect-Spiral`.

[13] J. Welch, D. Backer, L. Blitz, D.-J. Bock, G. Bower, C. Cheng, S. Croft, M. Dexter, G. Engargiola, E. Fields, J. Forster, C. Gutierrez-Kraybill, C. Heiles, T. Helfer, S. Jorgensen, G. Keating, J. Lugten, D. MacMahon, O. Milgrome, D. Thornton, L. Urry, J. van Leeuwen, D. Werthimer, P. Williams, M. Wright, J. Tarter, R. Ackermann, S. Atkinson, P. Backus, W. Barott, T. Bradford, M. Davis, D. DeBoer, J. Dreher, G. Harp, J. Jordan, T. Kilsdonk, T. Pierson, K. Randall, J. Ross, S. Shostak, M. Fleming, C. Cork, A. Vitouchkine, N. Wadefalk, and S. Weinreb, "The Allen Telescope Array: The first widefield, panchromatic, snapshot radio camera for radio astronomy and SETI," *Proceedings of the IEEE*, vol. 97, pp. 1438–1447, Aug. 2009.

[14] J. L. Volakis, ed., *Antenna Engineering Handbook*, ch. 49 Radio Telescope Antennas. New York: McGraw-Hill, 4th ed., 2007.

[15] W. Imbriale, "Design of a wideband radio telescope," in *Proc. IEEE Aerospace Conference*, pp. 1–12, Mar. 2007.

[16] Chris73, "Nautilus shell cut in half." Last accessed on 13, Mar., 2010 at `http://upload.wikimedia.org/wikipedia/commons/0/08/NautilusCutawayLogarithmicSpiral.jpg`.

[17] M. Livio, *The Golden Ratio*. New York: Broadway Books, 2003.

[18] C. A. Balanis, *Antennas Theory Analysis and Design*. New York: John Wiley and Sons, 3rd ed., 2005.

[19] P. Mayes, "Frequency-independent antennas and broad-band derivatives thereof," *Proceedings of the IEEE*, vol. 80, pp. 103–112, Jan 1992.

[20] R. DuHamel and D. Berry, "A new concept in high frequency antenna design," in *IRE International Convention Record*, vol. 7, pp. 42–50, Mar 1959.

[21] W. L. Stutzman and G. A. Thiele, *Antenna Theory and Design*. New York: John Wiley and Sons, 2nd ed., 1998.

[22] R. Olsson, P.-S. Kildal, and S. Weinreb, "The Eleven antenna: a compact low-profile decade bandwidth dual polarized feed for reflector antennas," *IEEE Trans. Antennas and Propagat.*, vol. 54, pp. 368–375, Feb. 2006.

[23] J. Dyson, "The unidirectional equiangular spiral antenna," *IRE Trans. Antennas and Propagat.*, vol. 7, pp. 329–334, Oct. 1959.

[24] T. Landecker, July 2009. Personal communication.

[25] Microwave Studio's CST, Palo Alto, *CST 2008 Help*, 2008.

[26] A. Ludwig, "The definition of cross polarization," *IEEE Trans. Antennas and Propagat.*, vol. 21, pp. 116–119, Jan 1973.

[27] S. Bhaumik, M. Panahi, and D. Kettle, "Differential lna considerations for the Square Kilometer Array," in *Proc. ANTEM/URSI 2009.*, pp. 1–4, Feb. 2009.

[28] W. Fan, A. Lu, L. Wai, and B. Lok, "Mixed-mode s-parameter characterization of differential structures," in *Proc. 5th Electronics Packaging Technology Conf.*, pp. 533–537, Dec. 2003.

[29] "Single-ended and differential s-parameters," Apr. 2008. Application Note ver. HFAN-5.1.0.

[30] G. Cortes-Medellin, "Input impedance characterization of the QSC ultra wide band feed," in *IEEE AP-S Int. Symp. Dig.*, pp. 1–4, July 2008.

[31] J. Yang, X. Chen, N. Wadefalk, and P.-S. Kildal, "Design and realization of a linearly polarized Eleven feed for 1 to 10 ghz," *IEEE Antennas Wireless Propagat. Lett.*, vol. 8, pp. 64–68, 2009.

[32] J. Yang and P.-S. Kildal, "Optimization of large log-periodic dual-dipole antenna by using genetic algorithm on embedded element in small log-periodic array," in *Proc. 3rd EuCAP 2009*, pp. 1308–1311, Mar. 2009.

[33] P. Czajko, "Cantilevered Antennae Design of a Prototype Single Pixel Feed Receiver of the Square Kilometre Array Project," tech. rep., Herzberg Institute of Astrophysics, Victoria, Canada, Jan. 2010.

[34] J. E. Hansen, ed., *Spherical Near-Field Antenna Measurements*. Exeter, England: Short Run Press Ltd.

[35] "Antenna measurement theory." Available online at `http://www.home.agilent.com/upload/cmc_upload/All/ORFR-Theory.pdf`.

[36] R. Johnson, H. Ecker, and J. Hollis, "Determination of far-field antenna patterns from near-field measurements," *Proceedings of the IEEE*, vol. 61, pp. 1668–1694, Dec. 1973.

[37] G. F. Masters and S. F. Gregson, "Coordinate system plotting for antenna measurements," 2007. Available online at `http://www.nearfield.com/amta/AMTA07-0092-GFM_SFG.pdf`.

[38] A. C. Newell, "Spherical coordinate systems for defining directions and polarization components in antenna measurements," 1998. Available online at `http://www.nearfield.com/amta/1998SPHERICALCOORDINATESYS.pdf`.

[39] D. M. Pozar, *Microwave Engineering*. New York: John Wiley and Sons, 3rd ed., 2005.

[40] Agilent Technologies, *4-Port PNA-L Microwave Network Analyzer N5230A*, 2009.

[41] Agilent Technologies, *Agilent Electronic Calibration (ECal) Modules for Vector Network Analyzers*, 2009.

Appendix

ACRONYMS

active region AR

Advanced Design System ADS

Allen Telescope Array ATA

antenna under test AUT

Aperture Arrays AAs

Computer Simulations Technology CST

computer-aided design CAD

cross polarization level XPL

curved trapezoidal tooth CTT

Dominion Radio Astrophysical Observatory DRAO

electromagnetic EM

focal length to dish diameter f/D

Fourier Transform FT

Frequency Independent FI

ground plane GP

Herzberg Institute for Astrophysics HIA

large number small diameter LNSD

log periodic dipole array LPDA

log periodic log spiral LPLS

log periodic LP

logarithmic spiral LS

low-noise amplifier LNA

National Research Council NRC

orthomode transducer OMT

perfect electric conductor PEC

Phased Array Feeds PAFs

printed circuit board PCB

Quasi-Self-Complementary QSC

Self-Complementary SC

Self-similar SS

side lobe level SLL

Single Pixel Feeds SPFs

Square Kilometer Array SKA

transmission line region TLR

ultra wideband UWB

vector network analyzer VNA

Visual Basic for Applications VBA

Wideband Single Pixel Feed WB+SPF